WETTING AND INTERFACIAL WATER ANALYSIS OF SELECTED MINERAL SURFACES AS DETERMINED BY MOLECULAR DYNAMICS SIMULATION AND SUM FREQUENCY VIBRATIONAL SPECTROSCOPY

by

Jiaqi Jin

A dissertation submitted to the faculty of
The University of Utah
in partial fulfillment of the requirements for the degree of

Doctor of Philosophy

Department of Metallurgical Engineering

The University of Utah

May 2016

The University of Utah Graduate School

STATEMENT OF DISSERTATION APPROVAL

The dissertation of **Jiaqi Jin**

has been approved by the following supervisory committee members:

Jan D. Miller	, Chair	**Dec 21, 2015** Date Approved
Xuming Wang	, Member	**Dec 21, 2015** Date Approved
Michael L. Free	, Member	**Dec 21, 2015** Date Approved
Vladimir Hlady	, Member	**Dec 21, 2015** Date Approved
Liem X. Dang	, Member	**Dec 21, 2015** Date Approved

and by **Manoranjan Misra** , Chair/Dean of

the Department/College/School of **Metallurgical Engineering**

and by David B. Kieda, Dean of The Graduate School.

ABSTRACT

In this dissertation research, Molecular Dynamics Simulation (MDS), Sum Frequency Vibrational Spectroscopy (SFVS), and contact angle measurement have been used to investigate the wettability and interfacial water structure at selected mineral surfaces. The primary objective is to provide fundamental understanding of the hydrophobic surface state, a state of special interest in particle separations by froth flotation.

First, MDS interfacial water features, including water number density profile, water residence time, water dipole orientation, and hydrogen bonding analysis, at selected hydrophobic mineral surfaces (graphite (001) surface and octadecyltrichlorosilane (OTS) monolayer on quartz) and at selected hydrophilic mineral surfaces (quartz (001), sapphire (001), and gibssite (001) surfaces) have been evaluated and compared to the corresponding SFVS experimental results. A "water exclusion zone" of 3 Å accounts for the "free OH" vibration (from both MDS water dipole orientation analysis and SFVS spectrum) at hydrophobic surfaces. In addition, a water residence time of less than 10 ps and about 2 hydrogen bonds have been found for surface water molecules at the selected hydrophobic mineral surfaces.

Sessile drop wetting characteristics of the hydrophobic molybdenite (001) surface and the hydrophilic quartz (001) surface have been examined by MDS and by contact angle experiments to determine the effect of drop size, advancing/receding contact angles, and spreading time on wettability. In addition, film stability and bubble attachment at the

hydrophobic molybdenite (001) surface and the hydrophilic quartz (001) surface have been studied by MDS for the first time and the results compared with corresponding experimental captive bubble contact angles. At the hydrophobic molybdenite (001) surface, the water film is unstable and ruptures, while the water film at the hydrophilic quartz (001) surface does not.

Finally, the wettability and interfacial water features of sulfide/telluride mineral surfaces have been described with MDS for the first time. The interfacial water features of selected sulfide/telluride mineral surfaces under anaerobic conditions have been examined, as well as Cu^{2+} activated sphalerite (110) and oxidized pyrite (100) surfaces, to determine which interfacial water features best identify the wetting characteristics of the selected mineral surfaces.

In summary, it has been found that "water exclusion zone" and "free OH" vibration present for hydrophobic mineral surfaces, whereas, for hydrophilic mineral surfaces, the interfacial water is characterized by hydrogen bonding with the surface and relatively long water residence time. The interfacial water analysis of the selected mineral surfaces increases our fundamental understanding of the flotation chemistry associated with the mineral systems and is expected to provide a foundation for improved flotation technology in the future.

TABLE OF CONTENTS

LIST OF TABLES

LIST OF FIGURES

ACKNOWLEDGEMENTS

Part of the financial support for this thesis research was provided by the U.S. Department of Energy (DOE) under Basic Science Grant No. DE-FG-03-93ER14315. The support and resources from the Center for High Performance Computing at the University of Utah are gratefully acknowledged. Part of the calculations was carried out using computer resources provided by the Division of Chemical Sciences, Geosciences, and Biosciences, Office of Basic Energy Sciences (BES), of the DOE at the Pacific Northwest National Laboratory.

The author is grateful to Dr. Hao Du, Prof. Tsun-Mei Chang, Prof. Collin D. Wick, and Prof. Erich Peterson for valuable discussions. Thanks are extended to Ms. Dorrie Spurlock for her proofreading of the manuscript.

CHAPTER 1

INTRODUCTION

1.1 Froth Flotation of Sulfide/Telluride Minerals

In the early twentieth century, froth flotation was developed at the Broken Hill mine, Australia to float sphalerite, a zinc sulfide mineral. Due to the development of froth flotation technology for the modern mining industry, low-grade and complex ore bodies could be mined economically. Sulfide minerals are the largest group of minerals floated. Currently, billions of tons of sulfide ores are concentrated annually all over the world with froth flotation.

Sulfide mineral flotation is an important industrial technology, and its associated surface chemistry has been studied extensively. It is well known that sulfide mineral surfaces are thermodynamically unstable and undergo oxidation and hydrolysis reactions when exposed to air and water (Chander, 1991). As a result, surfaces of sulfide minerals become hydrophilic and typically wetted by water. However, unlike most nonsulfide minerals, under anaerobic conditions in which no oxidation occurs, sulfide mineral surfaces have a natural hydrophobic character, and this intrinsic hydrophobicity accounts for the fact that sulfide flotation can generally be accomplished with short-chain sulfhydryl collectors at low levels of dosage. This natural surface chemistry of sulfide minerals is important because it provides a fundamental foundation for understanding

sulfhydryl collector adsorption and a basis for the design of selective flotation separation processes.

Several investigations have demonstrated that many sulfide minerals exhibit native floatability and can be floated without a collector. Flotation of various sulfides in the virtual absence of oxygen (i.e., in water containing less than 5 ppb oxygen) has shown the natural floatability of these minerals under such conditions (Fuerstenau and Sabacky, 1981). Essentially, complete flotation of galena, chalcopyrite, and pyrite occurs under anaerobic conditions. Fresh sphalerite exhibits only modest floatability under anaerobic conditions. However, after activation with Cu^{2+} cation, complete flotation of sphalerite is achieved under the same flotation conditions in the absence of collector. Similar observations have been made by other researchers (Finkelstein et al., 1975; Fornasiero and Ralston, 2006; Lepetic, 1974; Ravitz, 1940).

For sulfide mineral oxidation under different conditions, the reaction products have been studied by X-ray Photoelectron Spectroscopy (XPS) (Buckley and Woods, 1987; Buckley et al., 1989; Buckley and Woods, 1984a, b). It is now well established that sulfide mineral oxidation follows a reaction mechanism in which metal oxide or hydroxide products and an underlying metal-deficient or sulfur-rich surface are formed. A number of previous researchers have shown that these oxidation products, particularly metal oxides and hydroxides, interfere with the recovery and selectivity of sulfide minerals during froth flotation (Clarke et al., 1995; Grano et al., 1990; Guy and Trahar, 1985; Kristall et al., 1994; Zachwieja et al., 1989). The surface chemistry of oxidized sulfide mineral surfaces is significantly important for understanding the depression of sulfide minerals after oxidation (Fuerstenau et al., 1968; Fuerstenau et al., 1985).

Telluride minerals are similar to sulfides and are grouped with them in both the Dana and Strunz mineral classification systems (Dana, 1869; Strunz and Nickel, 2001). Tellurides are the only gold minerals other than native gold and electrum that are of economic significance. Gold tellurides are also as naturally floatable as are most sulfide minerals under anaerobic conditions (Marsden and House, 2006). At the Emperor mine in Fiji, gold tellurides have been floated without a collector. Commonly, the same type of short chained thiol collectors used for sulfide flotation are used to float gold tellurides together with free gold and gold-bearing sulfides for subsequent cyanidation, such as at the Kalgoorile operations in western Australia and the Cripple Creek operations in Colorado. It is interesting to compare the natural floatability of gold telluride minerals and sulfide minerals from the surface chemistry perspective.

1.2 Froth Flotation of Oxide Minerals

Although initially, froth flotation has been developed to treat the metal sulfides, the technology of froth flotation was eventually expanded to nonsulfide minerals. The froth flotation technology has been used to treat a diversity of nonsulfide mineral classes, including soluble salts (potash and borax), semisoluble salts (phosphates, fluorite, and calcite), and oxide minerals (metal oxides, mica, quartz, and feldspar). Among the non-sulfide mineral classes, metal oxide minerals are a major resource for important metals, such as aluminum, iron, manganese, titanium, and tin. In order to recover these metals, direct or reverse flotation technologies of oxide minerals have been developed (Fuerstenau and Raghavan, 1978; Weston, 1978).

The flotation chemistry of oxide minerals is distinctly different from the flotation

chemistry of sulfide/telluride minerals. In general, oxide minerals have an intrinsic hydrophilic surface property. Unlike sulfide/telluride minerals, oxide minerals require high levels of collector addition on the order of 1 lb per ton to establish a hydrophobic surface state. Also, the collectors used in froth flotation of oxide minerals are anionic or cationic surfactants containing hydrocarbon chains of more than 10 carbon atoms, which is longer than the hydrocarbon chain of the common collectors used for sulfide flotation (normally 5 carbon atoms or less). The surface chemistry of oxide minerals is significantly important for explaining the distinctly different flotation chemistry of oxide minerals when compared to sulfide/telluride minerals.

1.3 Hydrophobicity of Mineral Surfaces

In chemistry, hydrophobicity is the physical property of a molecule that is water repellent, which means there are repulsive interactions between such a molecule and water molecules. On the other hand, if a molecule is hydrophilic, water molecules are attracted to this molecule. For mineral surfaces, hydrophobic mineral surfaces are water repellent so they cannot be fully wetted by water, while the hydrophilic mineral surfaces are hydrated and have strong water wettability, water adheres to these hydrophilic surfaces.

In the process of froth flotation, hydrophobic mineral particles are separated from hydrophilic mineral particles in an aerated aqueous suspension. Attachment of hydrophobic mineral particles to air bubbles carries the hydrophobic mineral particles to the froth phase formed on top of the cell. In contrast, the hydrophilic mineral particles cannot attach to air bubbles and remain suspended in the slurry.

The attachment of hydrophobic mineral particles to air bubbles is the most important step in the froth flotation process. During froth flotation, mineral particles and air bubbles collide in the aerated aqueous suspension. During collision, the water film between the air bubble and the hydrophobic mineral particle ruptures, because of the repulsion force between the hydrophobic mineral surface and water molecules. Thus, the hydrophobic mineral particles attach to air bubbles and are recovered due to buoyant forces. However, for the hydrophilic mineral particles, which are water adherent, the water film does not rupture, so there is no attachment between the hydrophilic mineral particles and air bubbles. The hydrophobicity of mineral surfaces is of significant importance for the effective attachment between mineral particles and air bubbles.

Commonly, the hydrophobicity of a mineral surface can be quantified by contact angle measurements. When measuring the sessile drop contact angle of a mineral surface, a water drop is placed on the mineral surface. If the water spreads over the mineral surface, the contact angle is low and the mineral surface is hydrophilic. In contrast, if the water forms a stable drop instead, the contact angle is high and the mineral surface is hydrophobic. The hydrophobicity or wettability of mineral surfaces can also be described by the captive bubble contact angle measurements, which are measured when an air bubble is placed below and in contact with the mineral surface in an aqueous phase. In the captive bubble contact angle measurements, the water film at a very hydrophilic mineral surface does not rupture so no bubble attachment occurs, while, in the case of a hydrophobic surface, the film ruptures, attachment occurs, and a contact angle is established.

1.4 Interfacial Water

Improved understanding of hydrophobicity at a molecular level is of significant importance in the development of froth flotation technology. The hydrophobic surface state is established by the repulsion and adhesion forces between water molecules and the mineral surface. The nature of these forces has been discussed from a thermodynamic perspective (Eriksson and Yoon, 2007). In addition, the interactions between air bubbles and mineral particles have been measured using techniques like Atomic Force Microscopy (AFM) (Nguyen et al., 2003). Macroscopic results are related to microscopic behavior. In order to explain the hydrophobicity of mineral surfaces, knowledge of the behavior of interfacial water molecules at the mineral surfaces is of fundamental importance.

Due to the different nature of hydrophobic and hydrophilic mineral surfaces, the behaviors of interfacial water molecules at the hydrophobic and hydrophilic mineral surfaces are expected to be distinctly different. By exploring the different interfacial water characteristics at hydrophobic and hydrophilic mineral surfaces, an improved understanding can be achieved at the atomic scale. In the past decades, a number of experimental and computer simulation techniques have been used to study the interfacial water at mineral surfaces.

1.4.1 Sum Frequency Vibrational Spectroscopy

Different spectroscopic methods have been applied to study the interfacial water structure at mineral surfaces. For example, the interfacial water structure at soluble salt surfaces has been studied with Fourier Transform Infrared Spectroscopy (FTIR) (Cao et

al., 2011; Cheng et al., 2013; Yalamanchili et al., 1991). However, because FTIR is relatively less sensitive to the interfacial water molecules, it is difficult to explore the interfacial water structures using FTIR. A molecular monolayer-sensitive technique, Sum Frequency Vibrational Spectroscopy (SFVS), has been used to study the structure of water molecules at oxide mineral surfaces (Ostroverkhov et al., 2005; Shen, 1994; Shen and Ostroverkhov, 2006; Yeganeh et al., 1999) and fluorite surfaces (Eftekhari-Bafrooei and Borguet, 2009; Zhang et al., 2013). Although the spectroscopic signal has been difficult to analyze and the experimental results require further analysis at the molecular level, the SFVS results provide some experimental evidences of the interfacial water structure at mineral surfaces.

SFVS is a second-order nonlinear optical technique which can be used to detect structural information of molecules at the surfaces and interfaces, including gas-solid, gas-liquid, and liquid-solid interfaces. Two input incident laser beams, including a tunable Infrared (IR) beam and a visible beam, are focused at the same point on the surface. Then an output beam is generated with a frequency equal to the sum of the frequencies of the two input beams, as shown in equation (1.1).

$$\omega_{IR} + \omega_{vis} = \omega_{SFG} \tag{1.1}$$

The terms ω_{IR}, ω_{vis}, and ω_{SFG} are the frequencies for IR, visible, and SFG beams. Sum Frequency Generation (SFG) is a general form for the phenomena. This SFG process is shown in Figure 1.1.

When the IR beam is tuned through the spectral region of interest and the photon energy coincides with the energy of the molecular vibrational mode, the SFG response is enhanced resonantly.

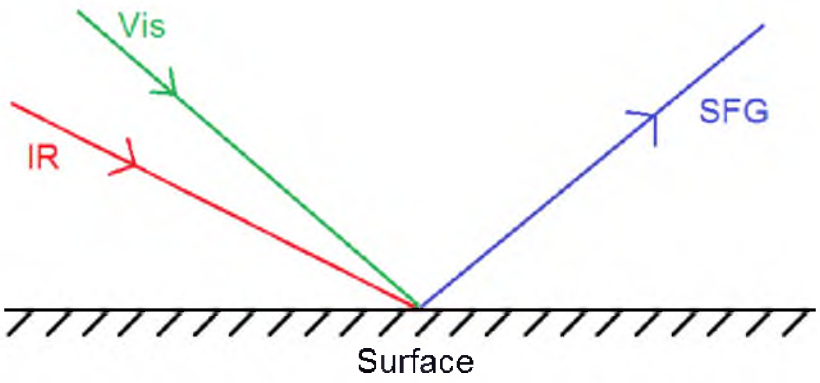

Figure 1.1 Schematic view of Sum Frequency Generation.

The SFG intensity is proportional to the two incident laser beams (IR and visible) and the square of the effective SFG susceptibility, which contains the measurable information about the response of the molecular system to the incident optical fields at the sum frequency (Wang et al., 2005; Zhuang et al., 1999).

The most important advantage of SFVS is its high sensitivity with good spatial and spectral resolution (Zhuang et al., 1999). The SFG response is a second-order response, so there is no SFG response in centrosymmetric systems. However, at the surfaces or interfaces where the inversion symmetry is broken, the SFG processes are allowed. This second-order nature of the SFG response contributes to the surface and interface sensitivity of SFVS (Richmond, 2002; Van Loon and Allen, 2004).

By assigning the surface as the xy plane and the surface normal as the z axis, s is defined as the polarization perpendicular to the xy plane, and p is defined as the polarization in the xz plane. The s polarized light only has one component in y direction, while the p polarized light can have x and z two components. As a result, particular susceptibilities with specific incident polarization combinations can be probed (Lambert et al., 2005). The most common polarization combination used is ssp, designating

polarization of beam in the following order s-polarized SFG, s-polarized visible, and p-polarized IR.

The SFG intensity is proportional to number density of the molecules detected at the interface. The higher SFG intensity represents more molecules detected. In addition, the SFG intensity is related to the orientation of molecules, i.e., the more ordered molecules give higher SFG intensity. According to the positions and relative intensities of the vibrational peaks in the SFVS spectra, quantitative and orientation information of interfacial molecules can be obtained. The characteristic frequencies and shape of the vibrational modes of molecular structures, such as CH, OH, and CO bonding, have been studied with SFVS (Schrödle and Richmond, 2008).

Thus, SFVS has the ability to be molecular monolayer sensitive and characterize different OH stretching vibrations at the mineral/water interface. SFVS is the preferred spectroscopic technique for exploring the different interfacial water structures at hydrophobic and hydrophilic mineral surfaces. In addition, SFVS is nondestructive to most crystal specimens and can be performed in situ.

1.4.2 Molecular Dynamics Simulation

Computational chemistry utilizes the methods of theoretical chemistry, incorporated into efficient computer programs, to calculate the structures and properties of molecules and solids. Different ways to determine the total energy in predicting molecular structures include Ab initio methods, Density Functional Theory (DFT), and Molecular Dynamics Simulations (MDS).

Because of the remarkable increase in computational capabilities in recent years, DFT

quantum chemical calculation methods, which can provide electron-level information about interactions between atoms, have been used in the study of minerals, such as molybdenite and quartz (Goumans et al., 2007; Todorova et al., 2004). In addition, DFT study of the interaction between a mineral surface and a single water molecule has been reported (De Leeuw et al., 2000). However, due to the limitation imposed by the magnitude of the DFT calculation, it would be difficult to explore the interfacial water structure using the DFT methods. When calculating a simulation system containing a mineral/water interface using the DFT methods, the energy minimum is difficult to be obtained. On the other hand, with the simplified pair potential models, MDS is capable to simulate a system containing a much larger number of atoms and can provide important molecular-level information about the structures and properties of interfacial water molecules at mineral surfaces.

The interactions considered in MDS to determine the total potential energy is shown in equation (1.2), where the total energy E_{total} is the sum of energies involved by bond stretching between two atoms E_{bonds}, angle between two bonds E_{angles}, dihedral of three bonds $E_{dihedrals}$, and nonbond interactions between two atoms $E_{nonbond}$.

$$E_{total} = E_{bonds} + E_{angles} + E_{dihedrals} + E_{nonbond} \quad (1.2)$$

In MDS, coordinates for each atom are used to represent its position in the space of the simulation system, i.e., the coordinates file, and a set of parameters is built to describe the interactions between each pair of atoms, i.e., the topology file. The initial coordinates and the interactions parameters are prepared before the simulation starts. Then, the simulation includes different stages, including energy minimization, equilibration dynamics, and production dynamics. The simulation results of the production dynamics

are commonly used for specific analysis, such as the structures and properties of molecules.

Because of the remarkable ability to simulate large systems, the contact angles of nanoscale water drops at mineral surfaces, such as graphite (001) surface, can even be measured by MDS (Werder et al., 2003). Much research based on MDS has been reported on interfacial water structures and properties at mineral surfaces, such as alkaline chloride, brucite, magnetite, and talc (Du and Miller, 2007a; Du and Miller, 2007b; Rustad et al., 2003; Wang et al., 2004a). With the capabilities to measure the wettability of mineral surfaces and to explore the interfacial water structures and properties at the mineral surfaces, MDS can provide information of the interfacial water molecules at a mineral surface with an MDS determined hydrophobicity. Thus, an atomic scale explanation about the origin of hydrophobicity of mineral surfaces can be obtained by the MDS study of interfacial water molecules at hydrophobic and hydrophilic mineral surfaces.

It is apparent that the reliability of MDS depends critically on the accuracy and efficiency of the interatomic potential models (i.e., force fields). In recent decades, much effort has been made to establish force fields for selected minerals, and many useful force fields have been developed, such as CLAYFF (Cygan et al., 2004), General Amber Force Field (GAFF) (Wang et al., 2004b), and the soluble salts force fields (Dang and Smith, 1995; Smith and Dang, 1994). GAFF includes force field models of most organic molecules. The CLAYFF force fields can be applied to several oxide/silicate minerals, such as gibbsite, quartz, and sapphire. For sulfide/telluride minerals, a few specific force fields have been made for pyrite (Sithole et al., 2003) and sphalerite (Wright and Gale,

2004) using the functional forms of the Buckingham potential (Buckingham, 1938). However, there is not a set of force fields such as CLAYFF for oxide/silicate minerals that is applicable for different mineral categories. Nevertheless, all the elements in sulfide/telluride minerals are involved in the Universal Force Field (UFF) developed by A. K. Rappé in 1992 (Rappé et al., 1992). In the UFF, parameters are estimated using general rules based on the element, its hybridization, and its connectivity.

1.5 Research Objectives

Previous researchers have studied the hydrophobicity of mineral surfaces by traditional methods and discussed the dispersion forces and polar forces between the interfacial water molecules and mineral surfaces (Drzymala, 1994; Gaudin et al., 1957). In contrast, this thesis utilizes a new method, MDS, to explore the hydrophobicity and interfacial water structures at mineral surfaces, in which the dispersion forces and polar forces are combined into the Lennard-Jones potentials and electrostatic interactions (Jones, 1924). It is intended that the results will contribute to a better understanding of the hydrophobic state of mineral surfaces. In addition, results from MDS interfacial water analysis are confirmed by SFVS. The following five research objectives have been established for this dissertation research.

First, MDS interfacial water features which best describe the wetting characteristics of hydrophobic/hydrophilic surface state of selected minerals are examined in Chapter 4. The graphite (001) surface and octadecyltrichlorosilane (OTS) monolayer were selected as examples of natural and collector-modified hydrophobic mineral surfaces. On the other hand, oxide mineral surfaces, such as the quartz (001), sapphire (001), and gibssite (001)

surfaces, were selected as examples of hydrophilic mineral surfaces. The MD simulations of oxide mineral surfaces have been reported but not been systematically considered for the interfacial water features (Argyris et al., 2008; McCarthy et al., 1996; Wang et al., 2006). Interfacial water structures at all these selected hydrophobic/hydrophilic mineral surfaces for MDS study in Chapter 4 can be studied by SFVS.

Second, interfacial water structures at the selected hydrophobic/hydrophilic mineral surfaces determined by SFVS are reported in Chapter 5 and compared with the corresponding MDS results from Chapter 4. The SFVS has been used to study interfacial water at collector-modified hydrophobic and natural hydrophilic surfaces by previous researchers (Shen et al., 2001). However, this dissertation research explores the interfacial water features at natural and collector-modified hydrophobic surfaces and at natural hydrophilic surfaces using both MDS and SFVS. SFVS spectra of the quartz/water interface were directly measured. However, a graphite multilayer on a quartz substrate was used for the SFVS measurements of interfacial water at the graphite (001) surface, and an OTS monolayer on a quartz substrate was used for the SFVS measurements of interfacial water at the OTS monolayer. Additionally, in order to clarify the free OH stretching observed on the SFVS spectra of the water/sapphire interface, SFVS study of the water/sapphire interface is repeated and compared to the MDS results of the water/sapphire and water/gibbsite interfaces.

Third, the effect of drop size on water sessile drop wettability for the molybdenite (001) and quartz (001) surfaces is examined using both MDS and experimental measurements. The wettability is described and analyzed in terms of advancing/receding contact angles and spreading time. The molybdenite (001) surface was selected as an

example of a hydrophobic mineral surface, while the quartz (001) surface was selected as an example of a hydrophilic mineral surface. In the past decades, the effect of drop size, advancing/receding contact angles, and spreading time on water sessile drop wettability of mineral surfaces has been reported (Drelich and Miller, 1994; Drelich et al., 1996; Dussan, 1979). However, not much MDS analysis has been done yet. This dissertation research examines water wettability at selected mineral surfaces using MDS and compares the MDS results with experimental results as reported in Chapter 6. In addition, the MDS advancing and receding contact angles at selected mineral surfaces, which have never been reported, are studied.

Fourth, MDS bubble attachment contact angles for the molybdenite (001) and quartz (001) surfaces are measured and compared to experimental results. It is the first time for measuring the MDS contact angles for selected mineral surfaces by the bubble attachment method. In the MD simulations of bubble attachment at the selected mineral surfaces, there is no gravity and buoyant force compared to experimental captive bubble contact angle measurements. MDS intermolecular interactions are represented by Lennard-Jones potentials and electrostatic interactions (Jones, 1924). The MDS bubble attachment results are compared to corresponding experimental captive bubble contact angles in Chapter 7. Of course, the stability of the water film is considered. At the selected hydrophobic mineral surface, the film is unstable and ruptures, while the water film at the selected hydrophilic surface does not.

Fifth, wettability and interfacial water features of sulfide/telluride mineral surfaces, which have never been studied with MDS, are reported in Chapter 8. The interfacial water features of selected sulfide/telluride mineral surfaces under anaerobic conditions

are examined, as well as Cu^{2+} activated sphalerite (110) and oxidized pyrite (100) surfaces, to determine which interfacial water features best identify the hydrophobic/hydrophilic surface state for selected mineral surfaces.

It is expected that the findings from this dissertation will increase our fundamental understanding of the flotation chemistry for these systems and provide a foundation for improved flotation technology in the future.

CHAPTER 2

EXPERIMENTAL CONTACT ANGLE PROCEDURES

Mineral surfaces selected for experimental contact angle measurements include: oxide mineral surfaces, hydrophobic quartz surface (coated with graphite multilayer or OTS monolayer), sulfide/telluride mineral surfaces under anaerobic conditions, oxidized pyrite (100) surface, and Cu^{2+} activated sphalerite (110) surface. Details of preparation and experimental contact angle measurements for the selected mineral surfaces are provided in the following sections.

2.1 General Procedures

General procedures for the experimental contact angle measurements using sessile drop and captive bubble techniques are provided in the following two sections.

2.1.1 Sessile Drop Measurement

For the experimental contact angle measurements using the sessile drop method, water drops with specific volumes/drop sizes were generated by a syringe using the 18MΩ·cm deionized water. Sessile drop contact angles were measured with a Rame-Hart goniometer. In order to avoid the influence of water evaporation, all contact angles were measured within 20 seconds after the water drop was put on the surface. At least ten

water drops were generated and measured. The average of these measurements is reported as the sessile drop contact angle value. The maximum experimental variation in sessile drop contact angle values was found to be ±3°, according to the error analysis.

2.1.2 Captive Bubble Measurement

A Rame-Hart goniometer was used to measure the captive bubble contact angles for selected mineral surfaces. The glass cell used for captive bubble contact angle measurements was cleaned with acetone and methanol then rinsed with 18MΩ·cm deionized water for at least three times. The mineral crystal sample was held by two glass cylinders and merged in the glass cell filled with 18MΩ·cm deionized water. Then an air bubble was released from the needle tip after formation with a syringe. The bubble was captured and attached at the selected mineral surface. Since the contact angle was measured for cases when attachment occurred, contact angles reported in this study are intermediate contact angles, which are between advancing and receding contact angles. At least ten air bubbles were generated and measured for each selected mineral surface. The reported captive bubble contact angle values are the average of these measurements. The maximum experimental variation in captive bubble contact angle values was found to be ±1°.

2.2 Preparation of Selected Mineral Surfaces

The following sections provide detailed information about preparation of the oxide mineral surfaces, hydrophobic quartz surface (coated with graphite multilayer or OTS monolayer), sulfide/telluride mineral surfaces under anaerobic conditions, oxidized pyrite

(100) surface, and Cu^{2+} activated sphalerite (110) surface for experimental contact angle measurements. The same procedures are used to prepare the selected mineral surfaces for SFVS measurements.

2.2.1 Oxide Surfaces

The oxide mineral surfaces selected for experimental contact angle measurements were quartz, sapphire, and gibbsite (001) surfaces. Pure quartz and sapphire single crystal specimens were cut into hemi-cylinder shape with both the diameter and height of 25 mm and purchased from Almaz Optics, Inc. The hemi-cylindrical shape was selected, because these quartz and sapphire specimens were also prepared for the SFVS internal reflection experiments. The crystallographic plane for the quartz and sapphire crystal surfaces is unknown. The quartz and sapphire surfaces were polished to the standard surface quality based on U.S. Standard MIL-PRF-13830B by Almaz Optics, Inc. The quartz and sapphire specimens were cleaned by rising with acetone, methanol, and 18MΩ·cm deionized water obtained from a Milli-Q system. Then, the quartz and sapphire crystals were blown dry with high-purity nitrogen gas. In order to remove possible organic contamination on the quartz and sapphire surfaces, the crystals were treated with argon plasma for 15 minutes. The gibbsite sample is from the rock and mineral collections of the College of Mines and Earth Sciences at the University of Utah. The fresh gibbsite (001) surface was cut from a gibbsite specimen then polished. Polishing procedures for the gibbsite (001) surface is the same with the sulfide mineral surfaces which will be provided in section 2.2.3. In addition, the gibbsite (001) surface was cleaned with the same cleaning procedures as used for quartz and sapphire. The contact angles of the selected oxide mineral surfaces

were measured using both sessile drop and captive bubble approaches.

2.2.2 Hydrophobic Quartz Surface

The graphite multilayer and OTS monolayer coated on a quartz substrate were prepared for experimental contact angle and SFVS measurements. Procedures for preparing the quartz substrates are provided in section 2.2.1.

The graphite multilayer was coated on the quartz substrate at the First Nano division of CVD Equipment Corporation using Chemical Vapor Deposition (CVD) method (Obraztsov et al., 2007). Experimental contact angle of the graphite multilayer coated on the quartz substrate was measured by captive bubble approach.

OTS reagents were purchased from Sigma-Aldrich, Inc. Its purity is higher than 90%. Since OTS would have violent reaction with water, during the self-assemble process, water is absolutely forbidden. The quartz substrate was cleaned with the same procedures as described in section 2.2.1 for cleaning the quartz surface. 0.1 g of OTS was diluted into 10 mL of benzene solvent. After the solution mixed well, the quartz substrate was soaked in the OTS benzene solution for 15 hours, in order to have OTS form a monolayer at the quartz surface. Then, the substrate was rinsed by chloroform for at least three times. The substrate was dried in an oven for 4 hours at 100 ℃. After the quartz substrate cool down to room temperature, it was used for captive bubble contact angle and SFVS measurements. The monolayer structure of the OTS molecules adsorbed on the quartz substrate was verified by the SFVS spectrum.

2.2.3 Sulfide/Telluride Minerals under Anaerobic Conditions

The sulfide/telluride mineral surfaces selected for experimental contact angle measurements under anaerobic conditions include the calaverite (001), covellite (001), galena (100), molybdenite (001), pyrite (100), and sphalerite (110) surfaces. Crystals of the selected sulfide/telluride minerals were obtained from the rock and mineral collections of the College of Mines and Earth Sciences at the University of Utah. According to different size and shape of mineral crystals, the selected mineral surfaces were prepared with different procedures, in order to proceed with the experimental contact angle measurements.

Sulfide mineral crystals were polished parallel to the preferred cleavage surface to create selected sulfide mineral surfaces. Roughness on the natural flat surfaces was eliminated by grinding with an 8-inch Aluminum diamond lap using 150 grit diamond for 2 minutes and fine grinding with 600 grit metal bonded diamond lap for another 2 minutes. Polishing procedures involved coarse polishing with 6 micron diamond dripped onto the polishing cloth and fine polishing with 1 micron diamond dripped onto a "Boehler Trident" polishing cloth. After a quick wash with water and drying with kimwipes, the sulfide mineral crystal sample was put into a Nitrogen ziplock plastic bag, in order to minimize surface oxidation.

The fresh pyrite (100) surface was cut from a cubic piece of a natural pyrite crystal (about 38mm × 36mm × 35mm) from Canonea, Mexico, then this surface was ground and polished. Due to the lack of large pieces of natural covellite, galena, and sphalerite crystals, these three samples were only polished parallel to the preferred cleavage surface to create the covellite (001), galena (100), and sphalerite (110) surfaces. Because of the

unique layered structure of molybdenite, in which the MoS_2 layers are held by VdW forces, the fresh molybdenite (001) surfaces were prepared by removing the top MoS_2 layer with adhesive tape.

The experimental contact angles of selected sulfide mineral surfaces were measured using the captive bubble technique. In order to reduce the amount of oxygen in water and produce an anaerobic condition, nitrogen gas was purged into the deionized water for 5 minutes before the crystal specimens were put in the deionized water environment.

A calaverite crystal (3mm × 2mm) from Cripple Creek, CO was used for experimental contact angle measurements at the calaverite (001) surface. From Energy-Dispersive X-ray Spectroscopy (EDXS) analysis, less than 10% of copper impurity was found in this calaverite crystal, a common impurity of calaverite (Afifi et al., 1988). In order to reduce damage to the caleverite crystal, the specimen was only fine polished using 1 micron diamond suspension on a "Boehler Trident" polishing cloth for the cleaved (001) surface. After quick washing with 18MΩ·cm deionized water and drying with Kimwipes, the specimen was put into a nitrogen-filled ziplock plastic bag to minimize surface oxidation. Due to the limited size of the calaverite specimen, it was difficult to measure the contact angle with the captive bubble technique. The experimental contact angle of the calaverite (001) surface was measured using the sessile drop method.

2.2.4 Oxidized Pyrite (100) Surface

The fresh pyrite (100) surface was prepared with the same procedures mentioned in section 2.2.3. A 30% hydrogen peroxide solution (pH = 4.0) was used to oxidize the pyrite crystal sample. After being soaked in a 30% hydrogen peroxide solution for 90

seconds, the pyrite crystal sample was quickly washed with deionized water and dried in a vacuum chamber. Then, the oxidized pyrite crystal sample was used for captive bubble contact angle measurements, taking SEM images, and EDXS analysis of the oxidized pyrite (100) surface. Another conditioning time for 180 seconds was applied on the fresh pyrite (100) surface to prepare the oxidized pyrite (100) surface with a different extent of oxidation for captive bubble contact angle measurements.

EDTA is able to "sequester" metal ions such as Ca^{2+} and Fe^{3+} because of its role as a hexadentate ("six-toothed") ligand and chelating agent. Saturated EDTA solution was used to wash the oxidized pyrite crystal sample, in order to remove the iron oxide/hydroxide at the oxidized pyrite (100) surface (Wiberg, 2001). After quickly being washed with water and dried in a vacuum chamber, the restored pyrite crystal sample was used for captive bubble contact angle measurements, taking SEM images, and EDXS analysis for the oxidized pyrite (100) surface without iron oxide/hydroxide.

2.2.5 Cu^{2+} Activated Sphalerite (110) Surface

Yellow transparent sphalerite crystals from Chirera, Mexico, with a purity of 99% by weight and, examined by EDXS analysis, were used to prepare samples for the experimental contact angle measurements for the Cu^{2+} activated sphalerite (110) surface. No iron or copper was found in these specimens. Each of the sphalerite crystals had a flat surface with a surface area of about 20mm × 20mm. The fresh sphalerite surfaces were prepared following the same procedures described in section 2.2.3.

The sphalerite crystal was soaked in the cell containing 1.0×10^{-5} mol/L $CuSO_4$ solution at pH = 5.3. After 5 minutes, at least five bubbles were generated and captive

bubble contact angles were measured. The captive bubble method was used to measure the contact angle of Cu^{2+} activated sphalerite (110) surface. Three sphalerite crystal samples were used to reproduce the results of contact angle measurement for the Cu^{2+} activated sphalerite crystal surfaces.

CHAPTER 3

MOLECULAR DYNAMIC SIMULATION PROCEDURES

3.1 Potential Energy Function

Amber, an MDS program package, was used for the simulation and analysis of interfacial water at selected mineral surfaces in this dissertation research (Pearlman et al., 1995). As mentioned in section 1.4.2, a potential energy function models the basic interactions between atoms in the MDS system. The total energy function in MDS was determined by evaluating the appropriate energy terms for all atom-atom interactions. In the Amber program, this total energy is expected to include the Coulombic/electrostatic, van der Waals, and bonded interactions, as is shown in Equation (3.1).

$$E_{Total} = E_{bonded} + E_{Coulombic} + E_{vdW} \quad (3.1)$$

The bonded term includes the bond stretch and angle bend energy terms. For example, the bond length and angle for the water models are represented as harmonic terms.

The Coulombic/electrostatic energy is represented by Equation (3.2) in which the energy of the interaction is inversely proportional to the distance of separation r_{ij}. The terms q_i and q_j are atomic partial charges for atoms i and j. The term e is the charge of an electron, and ϵ_0 is the dielectric permittivity of vacuum (8.85419×10^{-12} F/m).

$$E_{Coulombic} = \frac{e^2}{4\pi\epsilon_0}\sum_{i\neq j}\frac{q_i q_j}{r_{ij}} \quad (3.2)$$

The van der Waals energy term, represented by the conventional Lennard-Jones (12-6) function (Jones, 1924), includes the short-range repulsion associated with the increase in energy as two atoms approach each other and the attractive dispersion energy, as is shown in Equation (3.2). The term ε_{ij} is the depth of the potential well, and $r_{m,ij}$ is the distance at which the potential reaches its minimum.

$$E_{vdW} = \sum_{i\neq j}\varepsilon_{ij}\left[\left(\frac{r_{m,ij}}{r_{ij}}\right)^{12} - 2\left(\frac{r_{m,ij}}{r_{ij}}\right)^{6}\right] \quad (3.3)$$

The interaction parameters between unlike atoms are calculated according to the arithmetic mean rule for the distance parameter, r_m, and the geometric mean rule for the energy parameter, ε:

$$r_{m,ij} = \frac{1}{2(r_{m,i}+r_{m,j})} \quad (3.4)$$

$$\varepsilon_{ij} = \sqrt{\varepsilon_i \varepsilon_j} \quad (3.5)$$

3.2 Force Fields

As mentioned in section 1.4.2, force fields refer to the set of parameters for use in MDS. In recent decades, various kinds of molecular water models have been developed. The rigid SPC/E water model has the closest average configurational energy to the experimental value (-41.5 kJ mol^{-1}) (Kusalik and Svishchev, 1994; Mahoney and Jorgensen, 2000). Also, other calculated physical properties of the SPC/E water model are comparably good, such as self-diffusion, dielectric constant, and water dipole moment. Thus, the SPC/E water model was selected for exploring the interfacial water at selected mineral surfaces in this dissertation research.

Force field models for the selected oxide minerals, such as gibbsite-$Al(OH)_3$, quartz-SiO_2, and sapphire-Al_2O_3, are from CLAYFF. The CLAYFF is an ionic model, in which all atoms are treated as ions except OH groups. The interactions between atoms include the VdW and electrostatic interactions, which are described by Lennard-Jones parameters and atomic partial charges of each atom. The force field parameters for gibbsite-$Al(OH)_3$, quartz-SiO_2, and sapphire-Al_2O_3 are listed in Table 3.1.

The selected sulfide/telluride minerals for MDS study include calaverite-$AuTe_2$, chalcopyrite-$CuFeS_2$, copper-zinc sulfide-$CuZnS_2$, covellite-CuS, elemental sulfur-S, iron polysulfide-FeS_4, galena-PbS, molybdenite-MoS_2, pyrite-FeS_2, sphalerite-ZnS, and villamaninite-CuS_2.

A similar ionic force field model was used for the atoms in the selected sulfide/telluride minerals, which includes the Lennard-Jones parameters and atomic partial charges. The Lennard-Jones parameters of selected sulfide/telluride minerals are from Universal Force Field (UFF) (Rappé et al., 1992).

Table 3.1 Force field parameters for selected oxide minerals.

Mineral	Atom	r_m (Å)	ε (kcal/mol)	Q
Gibbsite-$Al(OH)_3$	Al	4.7943	0.0000013	1.575
	O	3.5532	0.1554	-0.950
	H	0.0	0.0	0.425
Quartz-SiO_2	Si	3.7064	0.0000018	2.1
	O	3.5532	0.1554	-1.05
Sapphire-Al_2O_3	Al	4.7943	0.0000013	1.575
	O	3.5532	0.1554	-1.05

Atomic partial charges for the Au, Cu, Fe, Mo, Pb, S, Te, and Zn atoms in the selected sulfide/telluride mineral crystals are Mulliken charges determined from the periodic DFT quantum chemical calculations of well-defined calaverite-$AuTe_2$, chalcopyrite-$CuFeS_2$, copper-zinc sulfide-$CuZnS_2$, covellite-CuS, galena-PbS, molybdenite-MoS_2, pyrite-FeS_2, sphalerite-ZnS, and villamaninite-CuS_2 unit cells using the Perdew-Wang 1991 (PW91) functional theory and the generalized gradient approximation (Perdew et al., 1996; Perdew et al., 1991), which is the same approach CLAYFF applied to assign atomic partial charges. The quantum program DMol3 was used to assign the Mulliken charges (Delley, 2000). For the iron polysulfide-FeS_4, parameters for the Fe and S atoms are the same as for the pyrite atoms, except the atomic partial charge for the S atoms in the iron polysulfide is set as half of the value for S atoms in pyrite, in order to make the polysulfide top layer electrically neutral. Similarly, for elemental sulfur-S, atomic partial charge for the S atoms is set as 0. The force field parameters for selected sulfide/telluride minerals are listed in Table 3.2.

In addition, the MDS study of the oxidized pyrite (100) surface involves the inclusion of ferric hydroxide. For the ferric cations (Fe^{3+}), the Lennard-Jones parameters are also from UFF, and the atomic partial charge is set as +3. The force field parameters for hydroxide anions are from a previous MDS study on chemical reactions of hydroxide groups (Peng and Merz Jr, 1992). Force fields for graphite used in this MDS are the same models in Werder's MDS study about water/graphite interactions (Werder et al., 2003). General Amber Force Field (GAFF) was used to simulate the OTS molecules in this dissertation research (Wang et al., 2004b). The initial structure of OTS molecule was generated by the Gaussian 09 software using the 6-31G basis set (Frisch et al., 2009).

Table 3.2 Force field parameters for selected sulfide/telluride minerals.

Sulfide/Telluride Mineral	Atom	r_m (Å)	ε (kcal/mol)	q
Calaverite $AuTe_2$	Au	3.293	0.039	0.1064
	S	4.035	0.274	-0.0532
Chalcopyrite $CuFeS_2$	Cu	3.495	0.005	0.27500
	Fe	2.912	0.013	0.49800
	S	4.035	0.274	-0.38650
Covellite CuS	Cu	3.495	0.005	0.110
	S	4.035	0.274	-0.110
$CuZnS_2$	Cu	3.495	0.005	0.230
	Zn	2.763	0.124	0.390
	S	4.035	0.274	-0.310
Elemental Sulfur S	S	4.035	0.274	0
Iron Polysulfide FeS_4	Fe	2.912	0.013	0.14750
	S	4.035	0.274	-0.036875
Pyrite FeS_2	Fe	2.912	0.013	0.14750
	S	4.035	0.274	-0.07375
Molybdenite MoS_2	Mo	3.052	0.056	0.45800
	S	4.035	0.274	-0.22900
Galena PbS	Pb	4.297	0.663	0.24670
	S	4.035	0.274	-0.24670
Sphalerite ZnS	Zn	2.763	0.124	0.45900
	S	4.035	0.274	-0.45900
Villamaninite CuS_2	Cu	3.495	0.005	0.172
	S	4.035	0.274	-0.086

3.3 Crystal Structures

Most of the crystal structures for selected minerals in this dissertation research are from the American Mineralogist Crystal Structure Database (Downs and Hall-Wallace, 2003), including calaverite-$AuTe_2$, chalcopyrite-$CuFeS_2$, covellite-CuS, galena-PbS, gibbsite-$Al(OH)_3$, graphite-C, molybdenite-MoS_2, pyrite-FeS_2, quartz-SiO_2, sapphire-Al_2O_3, sphalerite-ZnS, and villamaninite-CuS_2. Lattice parameters of the selected minerals are all from X-ray Diffraction (XRD) measurements of natural crystals.

Crystal structures of the copper-zinc sulfide-$CuZnS_2$, iron polysulfide-FeS_4, and elemental sulfur-S at the oxidized pyrite (001) surface are not available because of the difficulties in experimental measurements as well as a lack of specimens. However, these selected crystal structures were obtained by geometric optimization of known and relevant crystal structures using quantum chemical DFT methods. Quickstep package of the CP2K program can perform accurate and efficient DFT calculations on large, complex systems including, e.g., liquids, crystals, proteins, and interfaces (Mundy et al., 2000; VandeVondele et al., 2005). Quickstep is based on the Gaussian and Plane Waves method (GPW) and its augmented extension (GAPW). In this dissertation research, Quickstep was used to simulate the crystal structure of the iron polysulfide-FeS_4 and elemental sulfur-S at the (100) surface as well as the copper-zinc sulfide-$CuZnS_2$.

A simulation periodic box with a pyrite crystal in the bottom was created with the pyrite unit cell from American Mineralogist Crystal Structure Database. The surface was the pyrite (100) surface. The size of the simulation periodic box was 10.832Å × 10.832Å × 20.000Å, and the size of the cubic pyrite crystal was 10.832Å × 10.832Å × 10.832Å. There are 32 Fe atoms and 64 S atoms in the pyrite crystal. The DZVP-MOLOPT-SR-

GTH shorter range basis set (VandeVondele and Hutter, 2007) and Perdew-Burke-Ernzerhof (PBE) correlation functional (Perdew et al., 1996) were used in the DFT quantum chemical calculations in this dissertation research. To simulate the metal deficient layer produced during pyrite oxidation, i.e., iron polysulfide-FeS_4 and elemental sulfur-S at the (100) surface, different numbers of Fe atoms in the top atomic layer of a fresh unoxidized pyrite (100) surface (10.832Å × 10.832Å × 10.832Å) were removed. In the top atomic layer, there are a total of eight Fe atoms and 16 S atoms. In order to simulate the iron polysulfide-FeS_4 at the pyrite (100) surface, four Fe atoms were removed (50%), so the chemical formula for the polysulfide at the pyrite (100) surface is FeS_4. To simulate the elemental sulfur-S at the (100) surface, all eight Fe atoms were removed (100%), so the top layer is only composed of elemental sulfur dimers. These manipulated iron polysulfide-FeS_4 and elemental sulfur dimers-S_2 at the (100) surface were then calculated for DFT geometry optimization using the same basis set and functional described in the last paragraph. The two bottom layers of the pyrite crystals were also fixed in DFT calculations. It is well known that the atomic structure for one of the most common elemental sulfur allotropes is the 8-member ring structure (Steudel and Eckert, 2003). In order to simulate the elemental sulfur 8-member rings at the (100) surface, some of the sulfur dimers in the top layer were twisted by 30° to 90° without moving their centers before the DFT calculations. The same DFT calculations were used for the geometry optimization of this elemental sulfur-S at the (100) surface with twisted sulfur dimers.

To make the initial crystal structure for copper-zinc sulfide-$CuZnS_2$, a chalcopyrite crystal structure with the Fe atoms substituted by Zn was used as the initial crystal

structure of copper-zinc sulfide-$CuZnS_2$, because sphalerite and chalcopyrite have the same crystal structure. The chalcopyrite crystal lattice parameters are from the American Mineralogist Crystal Structure Database. This initial copper-zinc sulfide-CuZnS2 crystal structure is set as the input for the DFT quantum chemical calculation to obtain crystal geometry optimized by energy minimization. Similarly, the DZVP-MOLOPT-SR-GTH shorter range basis set and PBE correlation functional were used in this DFT quantum chemical calculation (Perdew et al., 1996; VandeVondele and Hutter, 2007).

3.4 Interfacial Water Analysis

The interfacial water features determined for MDS include water number density profile, water dipole orientation, water residence time, and hydrogen bonding analysis. To study the structure and properties of water molecules at selected mineral surfaces, a simulation periodic box containing a vacuum space at the top, a water phase in the middle, and a mineral crystal surface at the bottom for each selected mineral was made. The water box was generated by the Xleap module of the Amber software packages (Pearlman et al., 1995). The mineral crystal was expanded and cut using the CrystalMaker software packages (Palmer, 2009). The dimension of this periodic simulation system was set as about 40Å × 40Å × 100Å. The purpose for having a vacuum space was to make sure the water phase experienced the same pressure for all simulations. A snapshot of a simulation periodic system to study interfacial water at the molybdenite (001) surface is shown as an example in Figure 3.1. After a simulation time of 2 ns for equilibration of the system, a final simulation for another 2 ns was performed to produce results for analysis.

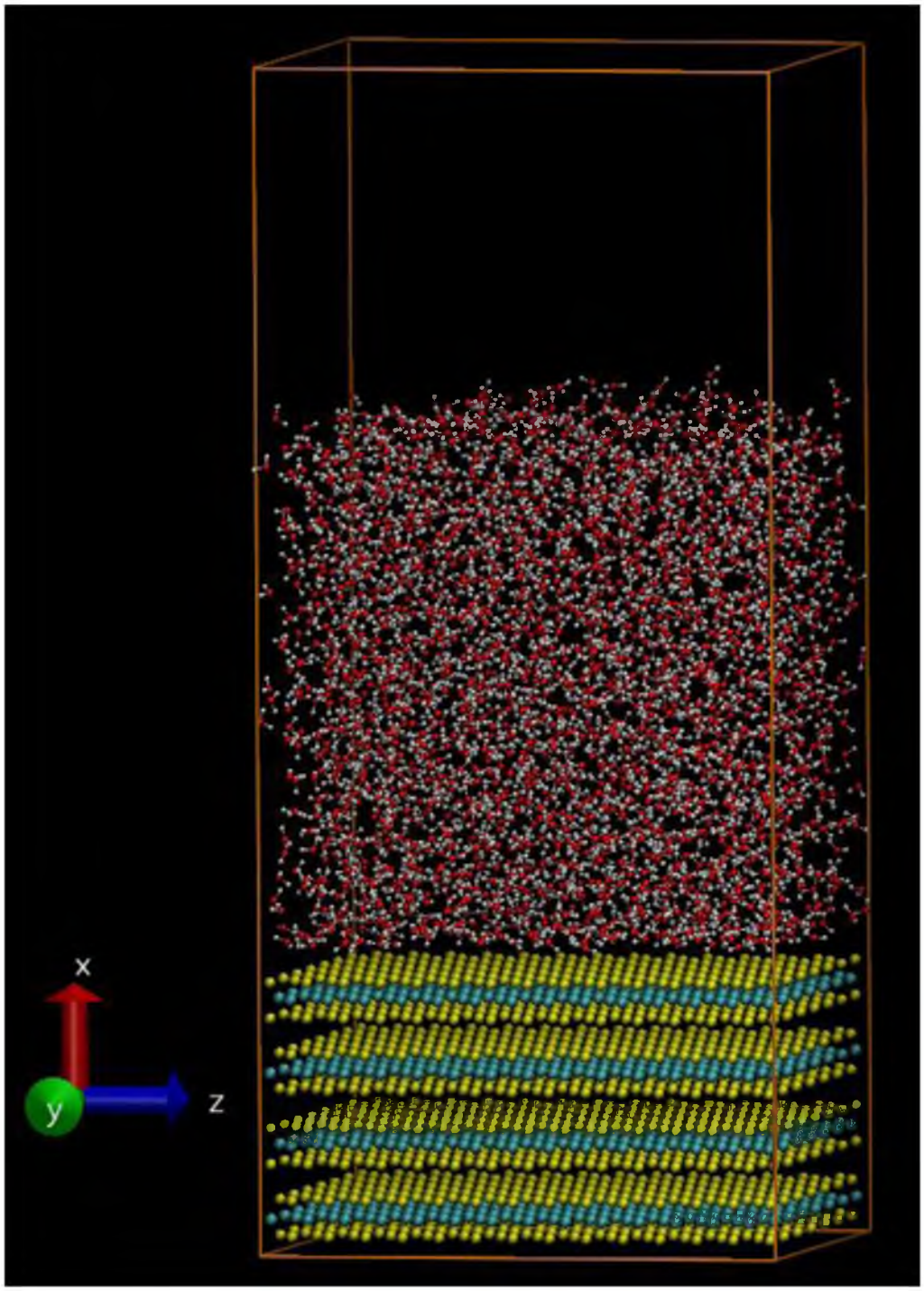

Figure 3.1. Snapshot of periodic system to study interfacial water at the molybdenite (001) surface. The simulation time is at 2 ns. The atoms' color code is as follow: cyan, Mo; yellow, S; red, O; white, H.

The canonical ensemble (NVT) was used for the MD simulations of interfacial water molecules at the selected mineral surfaces, in which case the amount (N), volume (V), and temperature (T) are conserved. The simulation temperature was set as 298 K.

In the MD simulations of interfacial water at the oxidized pyrite (100) surface, ferric cations and hydroxide anions were added in the water phase to simulate the accommodation of ferric hydroxide on the fresh and oxidized pyrite (100) surfaces. The number of hydroxide anions is three times the number of ferric cations to keep the system electrically neutral. For the fresh unoxidized pyrite (100) surface, the number of ferric cations is half of the number of Fe atoms at the surface. For the polysulfide and elemental sulfur at the (100) surface, the number of ferric cations equals the number of Fe atoms lost from the surface (metal deficient layer).

In this dissertation research, four computer programs were coded for the MDS interfacial water analysis of the selected mineral surfaces, including number density profiles, water dipole orientation, water residence time, and hydrogen bonding analysis. All these programs for interfacial water analysis were coded in Fortran 90 (Ellis et al., 1994). The analysis programs extract information of interfacial water structure and properties from the trajectory files of the MD simulations. The analysis procedures for interfacial water structure are provided in the following sections.

3.4.1 Number Density Profile

The number density profile of interfacial water molecules or ions in the aqueous phase provides a quantitative analysis of their distribution at the mineral/water interface. In the analysis of the number density distribution of interfacial water molecules or ions in

the aqueous phase, the simulation periodic box was divided into 0.5Å bins parallel to the selected surface. The number of molecules or ions in each bin was counted. In this study, the position of a water molecule is defined as the position of the center of mass for the water molecule. The number of molecules or ions in each bin was plotted versus the bin's distance from the surface, making the number density profile. In this dissertation research, the position of the selected mineral surface is defined as the position of the top layer atoms.

3.4.2 Water Dipole Orientation

A schematic illustration describing the orientation of a water dipole moment and the hydrogen position relative to the surface normal is shown in Figure 3.2. The angle α is the angle between the water dipole moment (oriented from negative to positive) and the surface normal. The angle β is the acute angle between the surface normal and a line connecting the two hydrogen atoms.

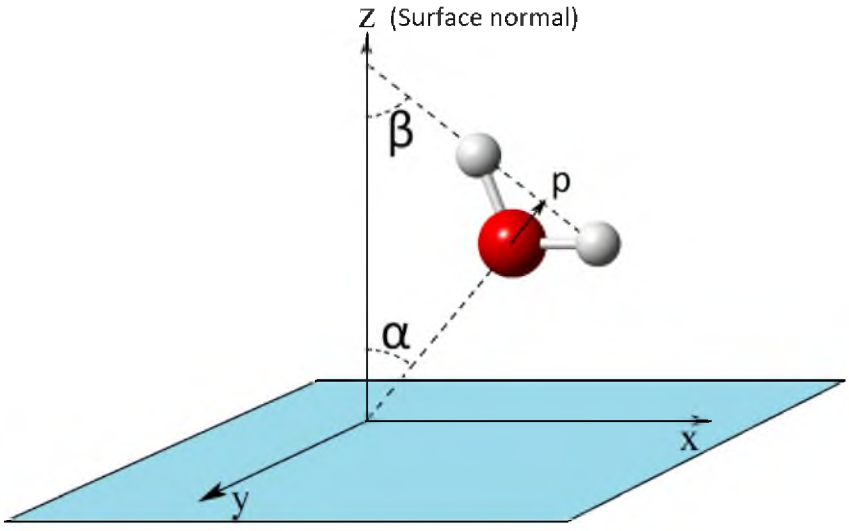

Figure 3.2. Schematic illustration describing the orientation of a water dipole moment by the angle (α) and hydrogen position relative to the surface normal by the angle (β).

To calculate the relative density distribution for water dipoles and hydrogen positions, the simulation periodic box was divided into 0.5Å bins parallel to the selected surface. In each bin, the angle α and angle β of the water molecules was measured, and their number density distribution for different degrees calculated. The range of angle α is from 0° to 180°, and angle β is from 0° to 90°. Then, the relative density distribution of water dipoles and hydrogen positions are plotted as a 3-dimensional surface with x axis as degree of angle α or β, y axis as distance from selected mineral surface, and z axis as the relative number density.

3.4.3 Water Residence Time

Besides the structural analysis of interfacial water, the dynamic properties of interfacial water molecules, such as water residence time, can also be studied using MDS. The water residence time, τ, is described as the time a water molecule spends in each water layer along the surface. It has been calculated using the residence-time correlation function defined by Equation (3.6). The term {R(t)} is derived from time correlation functions (Berendsen et al., 1987; Chowdhuri and Chandra, 2001; Koneshan et al., 1998) and is defined by Equation (3.7).

$$\tau = \int_0^\infty \{R(t)\}dt \tag{3.6}$$

$$R(t) = \frac{1}{N_h}\sum_{i=1}^{N_h}[\theta_i(0)\theta_i(t)] \tag{3.7}$$

Note that the term $\theta_i(t)$ is the Heaviside unit step function, which has the value 1 if a water molecule, i, is in the hydration shell of the reference water molecule at time t, and is zero otherwise. Water molecules in the hydration shell for more than 2 ps are considered to constitute the hydration shell. The term N_h is the apparent dynamic

hydration number. Here, this type of numbering system has also been used for tables and figures. The average residence time of water molecules in each layer of the water phase is plotted versus its distance from selected mineral surface. Then, the first peak of water residence time adjacent to the selected mineral surface is reported as the water residence time measured for the selected mineral surface.

3.4.4 Hydrogen Bonding Analysis

MDS results also provide information about the hydrogen bonding, including the hydrogen bonding between two water molecules, the hydrogen bonding between hydroxide group and water molecule, as well as the hydrogen bonding between surface oxygen and water molecule. For the SPC/E water model, two water molecules are defined as hydrogen bonded if the distance between the two oxygen atoms is less than 3.5 Å and the O…O-H angle is simultaneously less than 30° (Luzar and Chandler, 1996). The hydrogen bonding between a hydroxide group and a water molecule as well as between a surface oxide and a water molecule are defined in the same way as the hydrogen bonding between two water molecules.

Then, the hydrogen bond number per water molecule is calculated by divide the hydrogen bond number in each water layer by its corresponding water number. The hydrogen bond number per water molecule in each water layer is plotted versus the distance from selected mineral surface. The total number of hydrogen bonds per water is the sum of the number of hydrogen bonds formed with this water molecule from other water molecules, hydroxide groups, and surface oxygen atoms.

3.5 MDS Contact Angle

Procedures of the MDS sessile drop and bubble attachment contact angle measurements of selected mineral surfaces are provided in the following two sections.

3.5.1 Sessile Drop

To measure the simulated contact angle of water drops at selected mineral surfaces by MDS, a water drop containing certain number of water molecules was put on a selected mineral surface at the bottom of a simulation periodic box. A crystal of the selected mineral with specific mineral surface exposed was prepared with Crystal Maker software packages (Palmer, 2009). The initial coordinates of a water drop are from a water box with a specific size and number of water molecules generated by the Xleap module of the Amber software packages (Pearlman et al., 1995). Three different drop sizes studied in this dissertation research include 3, 4, and 5nm, which correspond to 800, 1300, and 1700 water molecules in the water drop.

Since periodic conditions are applied in the contact angle simulation, periodic images of the drops were avoided by using mineral surfaces with sufficient surface area. In this dissertation research, the horizontal extent of the surfaces was about 150Å × 150Å. A snapshot of a periodic simulation system to measure sessile drop contact angle of molybdenite (001) surface is shown as an example in Figure 3.3. Depending on the specific mineral being studied, the horizontal extent varies, because of the unique size of the crystal unit cell for each mineral being considered. Also, the vertical extent of the periodic simulation boxes was set at 150Å to avoid the influence of the periodic conditions on water drops.

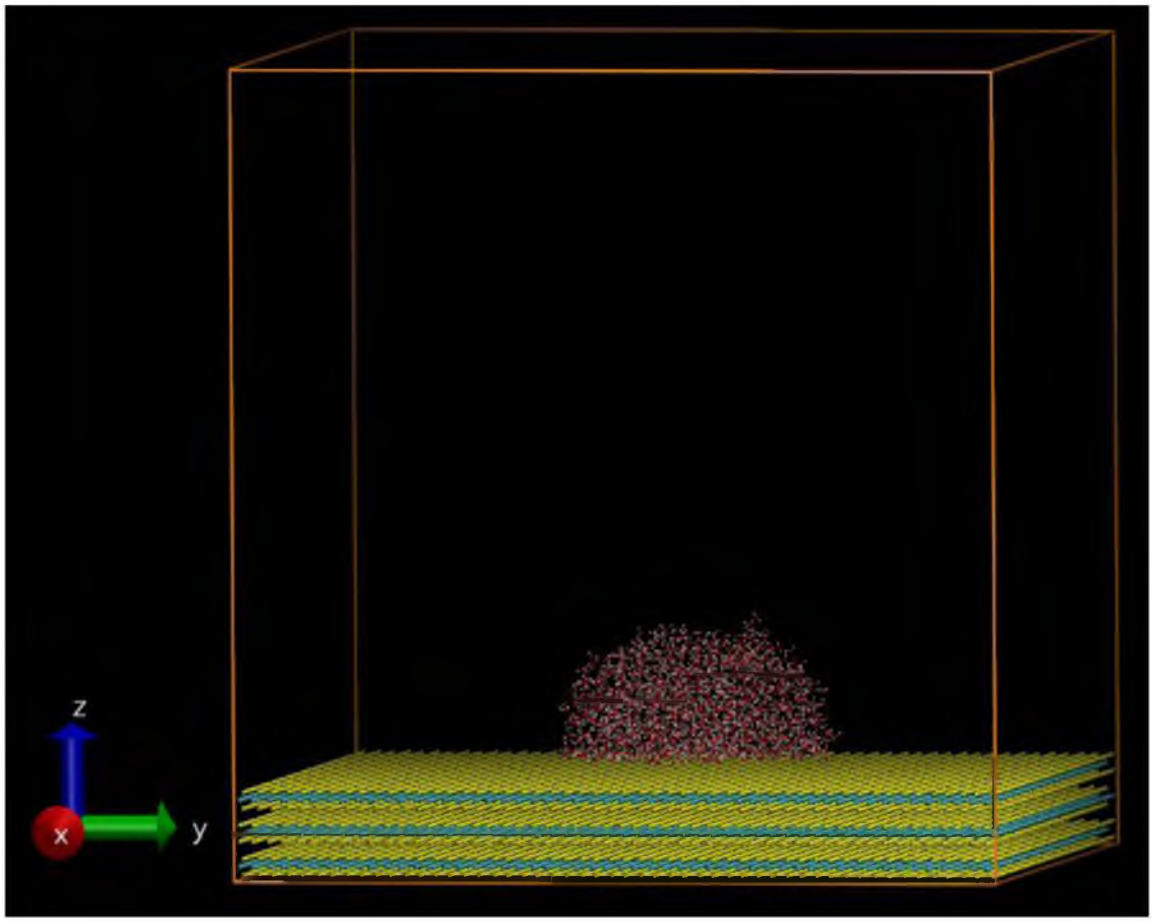

Figure 3.3. Snapshot of periodic simulation system to measure the sessile drop contact angle at the molybdenite (001) surface. The simulation time is at 1 ns. The atoms' color code is as follow: cyan, Mo; yellow, S; red, O; white, H.

As a result, the volume of simulation periodic boxes was about 3.375 $\times 10^6$ Å^3. Only one water molecule in this small volume will provide a saturated atmosphere, so the water drop in the simulation box would be stable under these conditions. The canonical ensemble (NVT) was used for the simulation of MDS sessile drop contact angle measurements. The simulation temperature was set as 298 K.

A total simulation time of 1 ns (1×10^6 steps each of 1 fs) is applied for MDS of the water drop for selected sulfide/telluride mineral surfaces, the graphite (001) surface, and the OTS monolayer, including a 500 ps equilibration period and another 500 ps analysis

period. For the selected sulfide/telluride mineral surfaces, graphite (001) surface, and the OTS monolayer, the water drop became stable after 500 ps of equilibration. Effect of spreading time on the MDS sessile drop wettability is discussed in section 6.1. The MDS sessile drop contact angles for the selected sulfide/telluride mineral surfaces, graphite (001) surface, and the OTS monolayer were measured based on an average for the following 500 ps. It is well known that the solubility of sulfide/telluride minerals and graphite in water is very low. In order to improve the calculation efficiency during simulation, the atoms for the sulfide/telluride minerals and for graphite were fixed as their respective initial positions (i.e., positions observed by XRD).

For the selected oxide mineral surfaces, such as the gibbsite (001), quartz (001), and sapphire (001) surfaces, the equilibration period in the MDS was extended to 1 ns, in order to assure equilibration of the water drop. Then, a subsequent 500 ps simulation was used for analysis to measure the MDS sessile drop contact angle. To test the effect of spreading time on the MDS water sessile drop wettability of selected mineral surfaces, the maximum simulation time was set as 5 ns.

To determine the MDS sessile drop contact angle, postprocessed densities of water molecules were plotted in two center planes: x-z plane and y-z plane. In this dissertation research, an analysis program was coded with Fortran 90 to explore the 2-dimensional number density distribution of water molecules of the water drop in the projection plane. The water number density at each pixel of the projection plane was calculated by this analysis program. The pixel size of this 2-dimensional water number density calculation is 1Å × 1Å. A 2-dimensional droplet with a contour line corresponding to the average of the liquid and vapor densities defines the boundary of the water drop, and the results are

expressed as a best fit contour line. The contact angle was measured by drawing a tangent line from the point at the foot of the contour line at a height of 8 Å from selected sulfide mineral surfaces to avoid the influence from density fluctuations at the water-mineral surface (Werder et al., 2003). For each contact angle measurement, the contact angles were measured in the x-z and y-z planes and then averaged (Shi and Dhir, 2009).

3.5.2 Bubble Attachment

To measure the bubble attachment contact angle of selected mineral surfaces, three steps are required, including creating the selected mineral crystal, simulating a gas bubble in an aqueous phase, and assembling them together in one simulation system.

The molybdenite (001) and quartz (001) surfaces were selected as examples of hydrophobic and hydrophilic mineral surfaces, respectively. The selected mineral crystals were prepared with the same methods mentioned in the section 3.4.2 for MDS sessile drop contact angle measurements.

Nitrogen gas was chosen for this simulation. A two point model for nitrogen molecules was used in this simulation (Rowlinson and Swinton, 2013). The initial coordinates of a nitrogen bubble containing 900 nitrogen molecules in an aqueous phase containing over 100,000 water molecules was generated by the Xleap module of the Amber software packages (Pearlman et al., 1995). Then, the isothermal-isobaric (NPT) ensemble was used to run the simulation for equilibration of the water and the nitrogen bubble with a simulation period of 500 ps. The amount (N), pressure (P), and temperature (T) were conserved.

After the water box containing the nitrogen bubble reached equilibrium, a part of

water molecules and the nitrogen bubble were separated from the initial water box and put adjacent to the selected mineral crystal surface. The initial distance between the nitrogen bubble and the selected mineral surface was set at 10 Å, i.e., the initial water film thickness at the selected mineral surface is about 10 Å. A snapshot of a periodic simulation system to measure the bubble attachment contact angle at a molybdenite (001) surface is shown as an example in Figure 3.4. A simulation period of 1 ns with NVT conditions was used to equilibrate the simulation system, then a subsequent 200 ps simulation was analyzed for measuring the simulated contact angles.

To determine the MDS bubble attachment contact angle, postprocessed densities of nitrogen molecules were plotted in two center planes: x-z plane and y-z plane. The analysis program mentioned in section 3.5.1 was applied to calculate the 2-dimensional number densities of nitrogen molecules in the nitrogen gas bubble. The pixel size of this 2-dimensional nitrogen molecule number density calculation is also 1Å × 1Å. A 2-dimensional air bubble with a contour line corresponding to the lowest nitrogen density defines the boundary of the nitrogen gas bubble, and the results are expressed as a best fit contour line. For each bubble attachment contact angle measurement, the contact angles were measured in the x-z and y-z planes and then averaged.

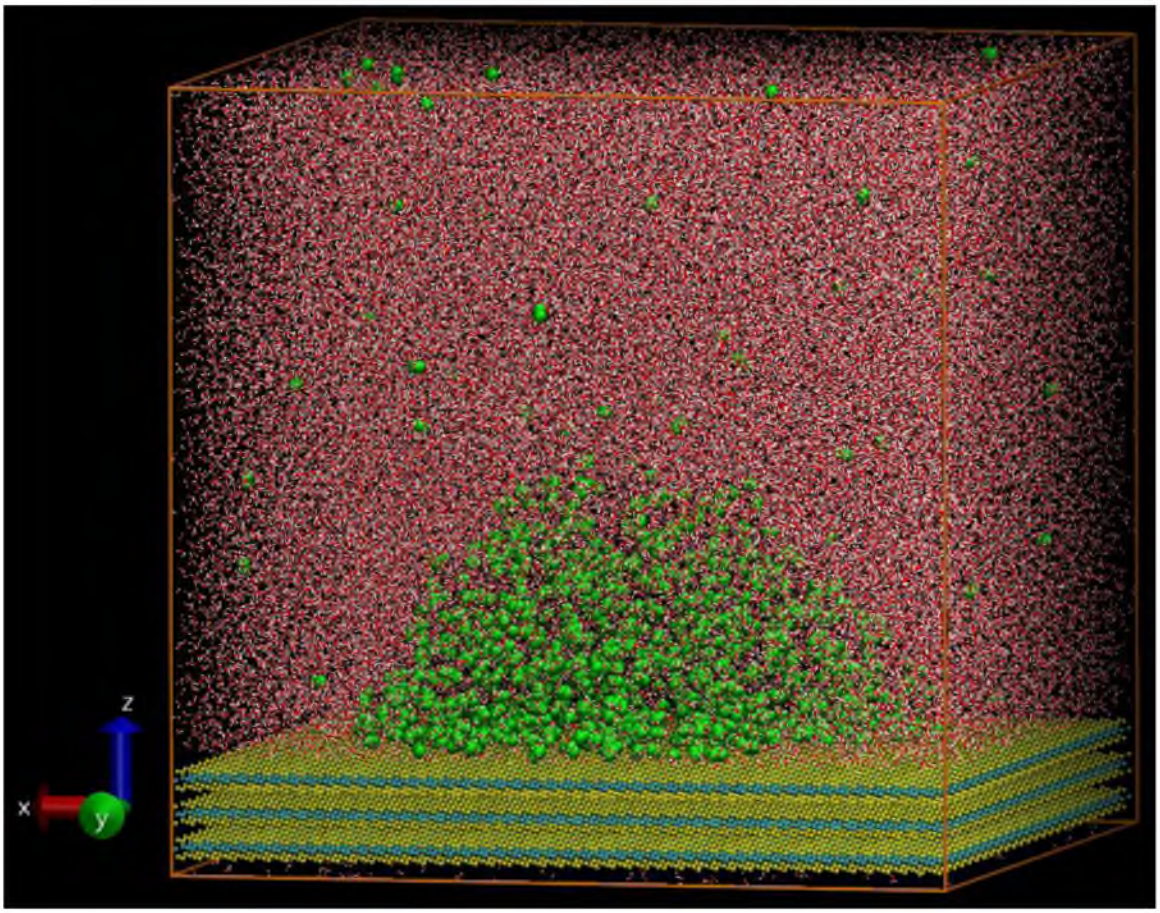

Figure 3.4. Snapshot of periodic bubble attachment simulation system to measure the water contact angle at a molybdenite (001) surface. The simulation time is at 1 ns. The atoms' color code is as follow: green, N; cyan, Mo; yellow, S; red, O; white, H.

CHAPTER 4

MDS INTERFACIAL WATER FEATURES

4.1 Selected Hydrophobic Surfaces

According to MDS and experimental sessile drop contact angles for the graphite (001) surface and OTS monolayer listed in Table 4.1, it is evident that the MDS results successfully predict the experimental values. Differences between the simulation and experimental contact angle values for the graphite (001) surface and OTS monolayer are 6.9% and 2.9%, respectively.

In addition, the MDS contact angle for the graphite (001) surface is consistent with a previous MDS study about water wettability of graphite (Werder et al., 2003). Both simulated and experimental contact angles reveal the hydrophobic surface state of the graphite (001) surface and OTS monolayer.

Table 4.1 MDS and Experimental Sessile Drop Contact Angles for the Graphite (001) Surface and OTS Monolayer.

Mineral Surface	Simulated Contact Angles, degree	Experimental Contact Angles, degree
Graphite (001) Surface	86	92
OTS Monolayer	108	105

As the examples selected for a natural hydrophobic surface and a collector-modified hydrophobic surface, MDS interfacial water features at the graphite (001) surface and OTS monolayer, including relative water number density profiles, water dipole orientation, water residence time, and hydrogen bonding analysis, are reported in this section to determine which best describes the interfacial water characteristics of a hydrophobic surface.

4.1.1 Water Exclusion Zone

MDS snapshots of interfacial water molecules at the graphite (001) surface and OTS monolayer are presented in Figure 4.1. Interfacial water molecules at the graphite (001) surface and OTS monolayer look similar from both directions.

At the solid/water interface for the graphite (001) surface and OTS monolayer, a gap between the water molecules and solid surface is found. This gap, reflecting the "water-excluded volume" or "water-exclusion zone", indicates relatively weak interaction between water molecules and the solid surface (Abraham, 1978; Yu et al., 1999). The presence of the "water exclusion zone" at the graphite (001) surface and OTS monolayer indicates that the selected hydrophobic surfaces have relatively weak interactions with water molecules, which is expected to be the origin of their macroscopic hydrophobic character. This "water exclusion zone" is filled with possible electron orbitals from water and from the crystal surface. From the snapshots in Figure 4.1, the "water exclusion zone" at the graphite (001) surface appears to be larger than the OTS monolayer. The graphite crystal structure is composed of flat Carbon monolayers held by VdW forces, so the graphite (001) surface is a flat and smooth surface.

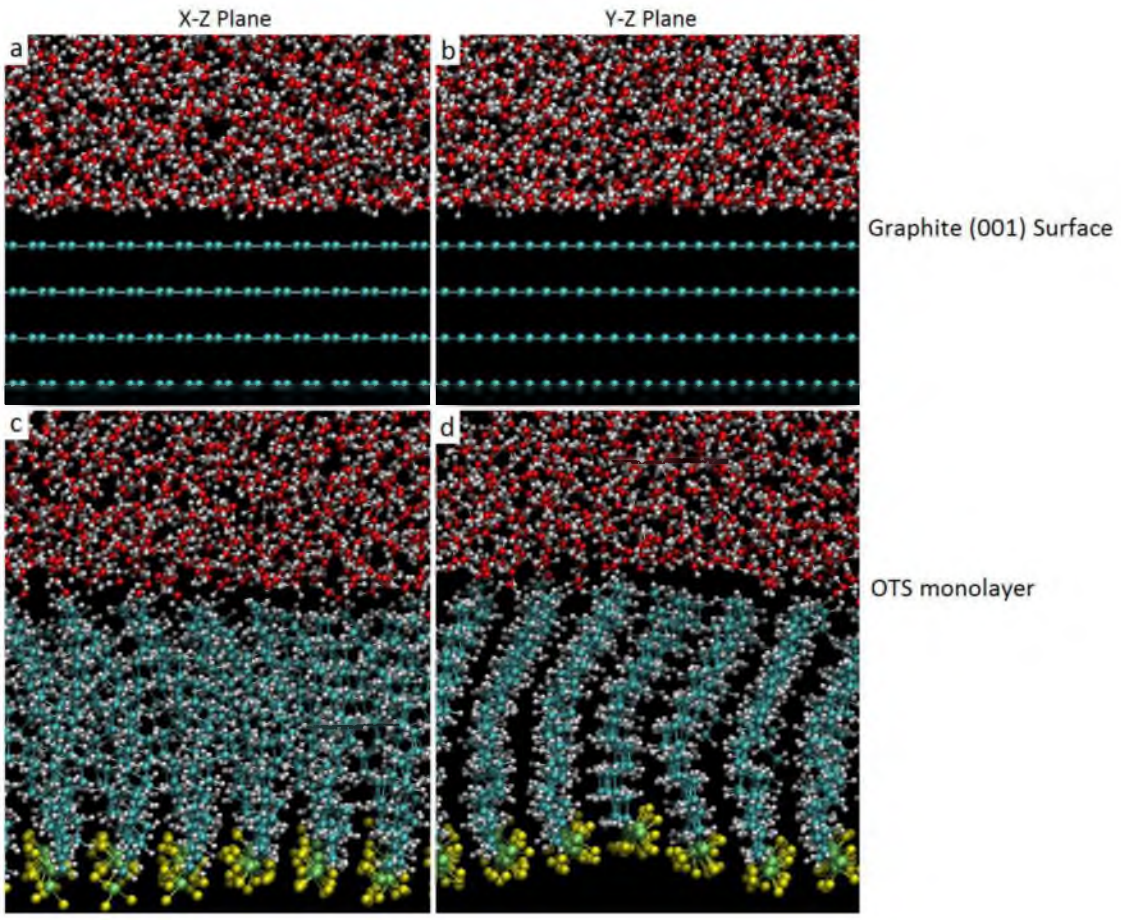

Figure 4.1. MDS snapshots of solid/water interfaces: (a), (b), graphite (001) surface; (c), (d), OTS monolayer. The simulation time is at 2 ns. The atoms' color code is as follows: cyan, C; lime, Si; white, H; yellow, Cl.

On the other hand, due to the bending, stretching and vibration of OTS molecules in the monolayer, the solid surface of OTS monolayer has a relatively large surface roughness. As a result, "water exclusion zone" at the OTS monolayer looks smaller than at the graphite (001) surface from the snapshots.

As a result of the "water exclusion zone", some interfacial water molecules do not have complete hydrogen bonding and can be observed as a free dangling OH bond at the solid/water interface, as can be observed from both the snapshots of the graphite (001) surface and OTS monolayer. Due to the lack of hydrogen bond donners at the graphite

(001) surface and OTS monolayer surface, there is no hydrogen bonding between the solid surface and interfacial water molecules.

The graphite (001) surface and OTS monolayer only have relatively weak interaction with interfacial water molecules, resulting in the "free OH" stretching of interfacial water molecules at these selected hydrophobic surfaces. The snapshots only show positions of molecules at a specific moment during the MD simulation. However, quantitative analysis of the trajectory of molecules in a 2 ns MD simulation period can provide more accurate information about interfacial water features at the selected hydrophobic surfaces.

4.1.2 Number Density Profile

The number density profiles of water molecules for the graphite (001) surface and OTS monolayer are shown in Figure 4.2. Position of the graphite (001) surface is defined as the first atomic layer, and position of the solid surface of OTS monolayer is set as an average of the top atom of each OTS molecule. Thickness of the "water exclusion zone" is determined by the distance between the center of the surface atoms and the center of mass for interfacial water molecules. For the graphite (001) surface, the first water density peak is about 3.2Å away from the surface , and this distance is greater than the distance between hydrogen-bonded water/water molecules, which is approximately 2.8 Å (Abraham, 1978; Dang and Pettitt, 1990; Lynden-Bell and Rasaiah, 1997; Rasaiah and Zhu, 1990; Smith and Dang, 1994). This result is consistent with the "water exclusion zone" presented in the snapshot in Figure 4.1 and demonstrates the relatively weak interaction between the interfacial water molecules and graphite (100) surface.

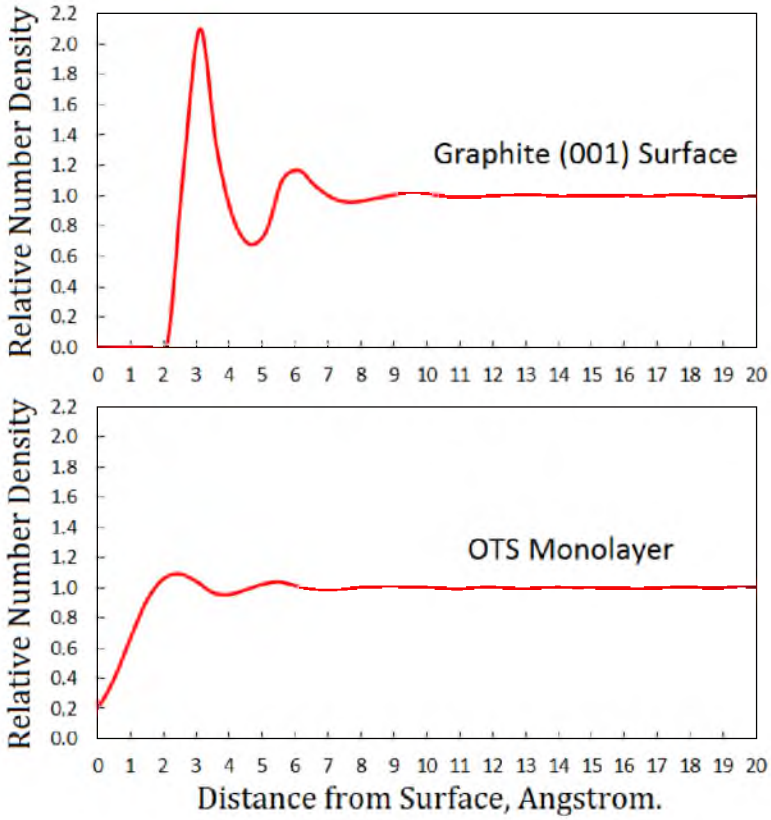

Figure 4.2. Relative water number density profiles at selected mineral surfaces: (a) graphite (001) surface; (b) OTS monolayer.

According to the MDS and experimental contact angles of the graphite (001) surface and OTS monolayer listed in Table 4.1, the OTS monolayer is more hydrophobic than the graphite (001) surface. It is expected that the distance between the first water density peak and the solid surface of OTS monolayer should be larger than the graphite (001) surface. However, for the OTS monolayer, the distance between the first water density peak and solid surface is about 2.5Å, as shown in Figure 4.2. This relatively smaller distance found at the OTS monolayer could be the result of surface roughness on the solid surface, due to the bending and stretching of OTS molecules. Thus, surface roughness has a great influence on the water number density profile at a mineral/water interface.

4.1.3 Water Dipole Orientation

The water dipole moment and hydrogen position relative density distributions for the graphite (001) surface and OTS monolayer are shown in Figure 4.3. Results for the graphite (001) surface show that the first water density layer is about 3 Å from the surface, which is consistent the number density profile. According to the large peak at 90° for the α angle, the dipole moment of most interfacial water molecules in the first water density layer is perpendicular to the surface normal which corresponds to preponderance of water molecules parallel to the surface. The peak of the β angle at 90° and shoulder of β angle from 70° to 0° indicate that interfacial water molecules are rotating or vibrating along the dipole moment with the initial and final states parallel to the surface.

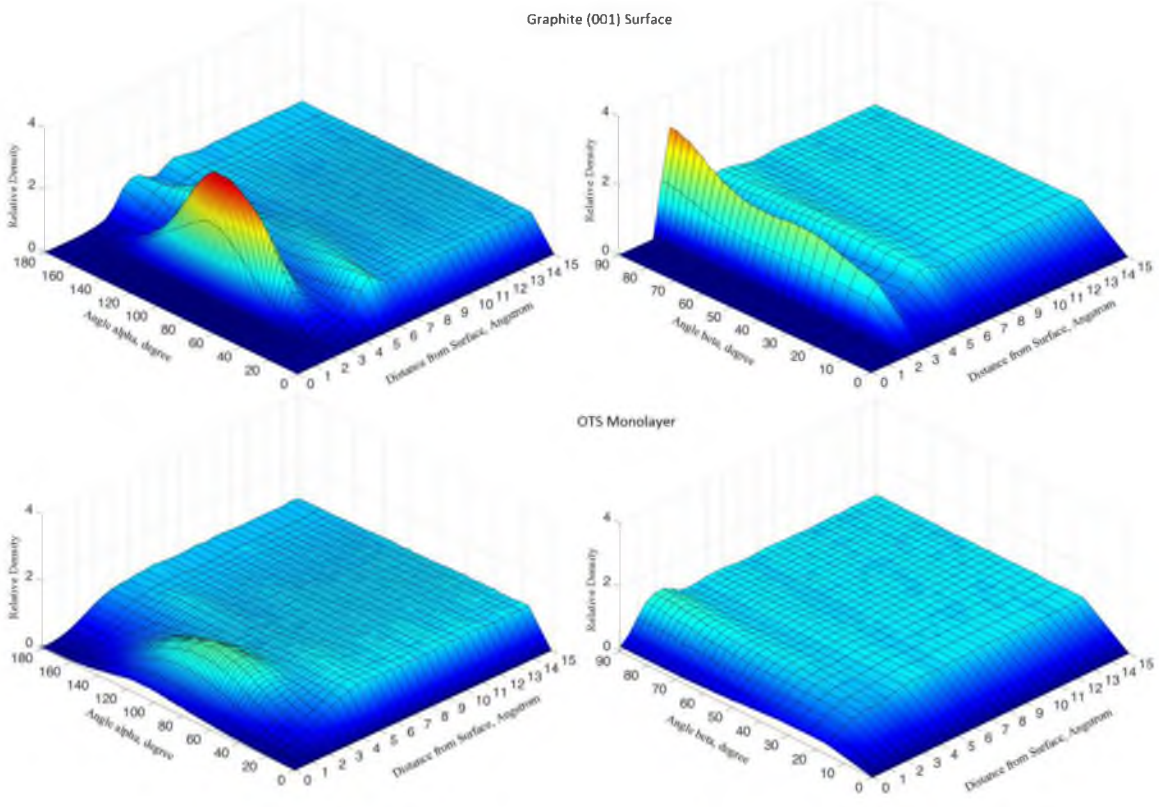

Figure 4.3. Water dipole moment (angle α) and hydrogen position (angle β) relative density distribution along the surface normal at selected mineral surfaces: (a) graphite (001) surface; (b) OTS monolayer.

The water dipole orientation and hydrogen position of interfacial water molecules at the graphite (001) surface support the "free OH" vibration analysis of interfacial water molecules presented in the snapshots in Figure 4.1, which is the result of relatively weak interaction between the interfacial water molecules and graphite (001) surface.

Results of the water dipole orientation analysis of interfacial water molecules at the OTS monolayer are similar to the graphite (001) surface, so water molecules of the first water density layer have similar water dipole orientation and hydrogen position, which suggests the "free OH" vibration of interfacial water molecules. However, the peaks of α and β angle at the OTS monolayer are relatively shorter than at the graphite (001) surface. Due to the surface roughness at the solid surface of OTS monolayer, water molecules in the first water density layer at the OTS monolayer surface are less ordered than at the graphite (001) surface. Thus, the surface roughness also has an influence on interfacial water dipole orientation analysis.

4.1.4 Water Residence Time

As listed in Table 4.2, positions of the first peak of water residence time at the graphite (001) surface and OTS monolayer are consistent with the first water density peaks from the water number density profiles. Compared to the water residence time at some hydrophilic mineral surfaces, such as the kaolinite alumina face surface, kaolinite silica face surface, and muscovite surface (Yin, 2012), magnitude of the residence time for the graphite (001) surface and OTS monolayer are relatively small. This indicates that the interfacial water molecules at the graphite (001) surface and OTS monolayer do not have strong interaction, such as hydrogen bonding, with the surface.

Table 4.2 Interfacial Water Residence Times of Graphite (001) Surface and OTS Monolayer

Mineral Surface	First Peak for Water Residence Time	
	Distance from Surface (Å)	Magnitude (ps)
Graphite (001) Surface	3.6	7.2
OTS Monolayer	2.5	4.7

In addition, the magnitude of interfacial water residence time at the OTS monolayer is smaller than at the graphite (001) surface, which reveals that interfacial water molecules at the OTS monolayer have comparably more relaxation. It is well-known that hydrocarbon chains of surfactant molecules are water repellant. The hydrocarbon chains of OTS molecules in the monolayer have relatively weaker interaction with the interfacial water molecules than the carbon atoms of the graphite (001) surface. This is consistent with the more hydrophobic surface state of OTS monolayer than the graphite (001) surface, as revealed by contact angle measurements.

4.1.5 Hydrogen Bonding Analysis

Distribution of the average number of hydrogen bonds per water molecule along the surface normal for the graphite (001) surface and OTS monolayer are shown in Figure 4.4. For the graphite (001) surface and OTS monolayer, from the interface to bulk water, the number of hydrogen bonds per water molecule increases until it reaches a plateau value around 3.35 about 4 Å from the surface, which is very close to the value of 3.5 reported in the literature (Nieto-Draghi et al., 2003).

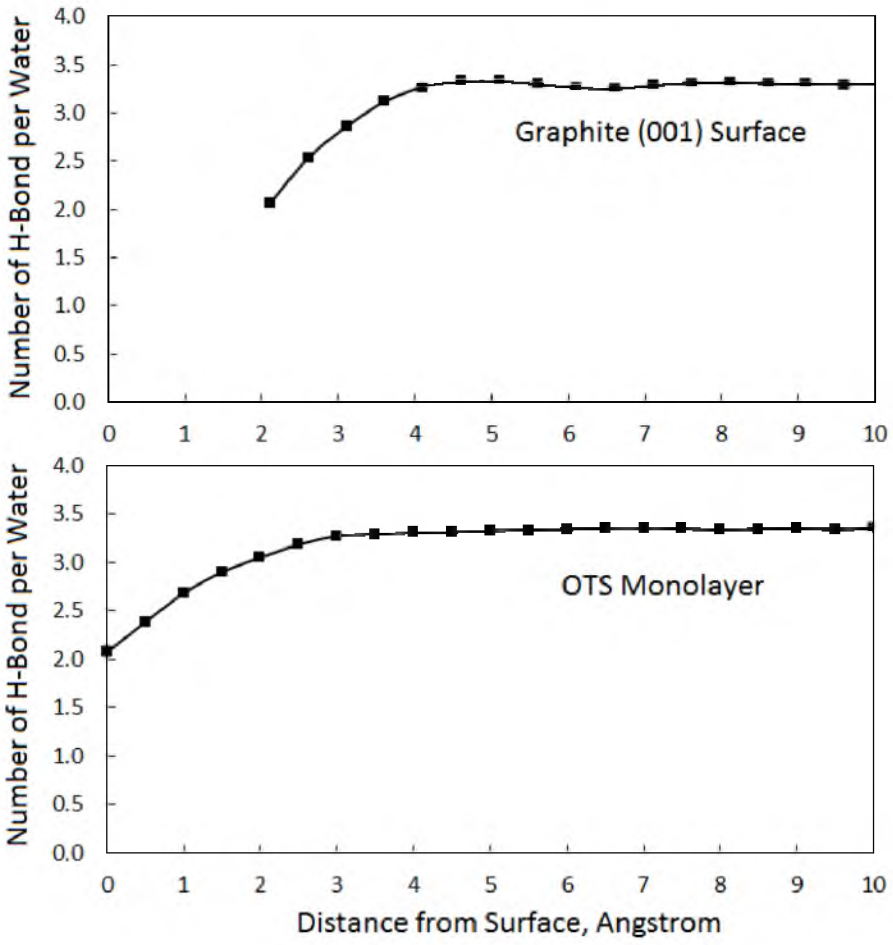

Figure 4.4. Distribution of hydrogen-bonding number per water molecule along the surface normal for selected mineral surfaces: (a) graphite (001) surface; (b) OTS monolayer.

When approaching the graphite (001) surface and OTS monolayer, number of hydrogen bonds per water molecule decreases from 3.35 to 2. As reported, because of the lack of hydrogen bond doners and accepters at the graphite (001) surface and OTS monolayer, the interfacial water molecules at the graphite (001) surface and OTS monolayer are "excluded" from the surface. Each interfacial water molecule at the solid/water interface only has the maximum of two water molecules coordinating around it, which is about half of the water coordination number in bulk water. Thus, the number of hydrogen bonds of the interfacial water molecules at the graphite (001) surface and

OTS monolayer is only around 2. The hydrogen bonding analysis of interfacial water at the graphite (001) surface and OTS monolayer confirm the relatively weak interaction between the interfacial water molecules and the selected hydrophobic surfaces.

4.2 Selected Hydrophilic Surfaces

MDS and experimental contact angles for the quartz (001), sapphire (001), and gibbsite (001) surfaces are listed in Table 4.3. Note that both the MDS and experimental contact angles of the selected oxide surfaces are sessile drop contact angles. MDS contact angles of the selected oxide mineral surfaces are mostly consistent with the experimental values. Results of the MDS and experimental contact angle measurements indicate a hydrophilic surface state of the quartz (001), sapphire (001), and gibbsite (001) surfaces, which confirms the fact that flotation of these oxide minerals require collectors with relatively long carbon chains (Pugh et al., 1996). Compared to the selected hydrophobic surfaces, the selected oxide mineral surfaces have a significantly better water wettability. This is the result of relatively stronger interaction between the selected oxide mineral surfaces and interfacial water molecules.

Table 4.3 MDS and Experimental Contact Angles for Quartz (001), Sapphire (001), and Gibbsite (001) Surfaces

Mineral Surface	Simulated Contact Angles, degree	Experimental Contact Angles, degree
Quartz (001) Surface	9	5 (random surface)
Sapphire (001) Surface	11	14 (random surface)
Gibbsite (001) Surface	0	2

In addition, during the 1 ns MD simulation for contact angle measurements, water was found to spread completely on the gibbsite (001) surface, whereas spreading was incomplete at the quartz (001) and sapphire (001) surfaces with water contact angles around 10°. This indicates that the gibbsite (001) surface is more hydrophilic than the quartz (001) and sapphire (001) surfaces. Due to possible hydrolysis reactions or crystal defects on the quartz surface, its experimental contact angle is 4° lower than MDS value. However, the experimental contact angles of the gibbsite and sapphire confirm the MDS results that the aluminum hydroxide (gibbsite) has a better water wettability than the aluminum oxide (sapphire). The comparably stronger interaction between interfacial water and the gibbsite (001) surface than the quartz (001) and sapphire (001) surfaces will be discussed regarding interfacial water features, including water number density, water dipole orientation, water residence time, and hydrogen bonding analysis.

4.2.1 Water Exclusion Zone

MDS snapshots in the x-z plane (left column) and in the y-z plane (right column) for the quartz (001), sapphire (001), and gibbsite (001)-water interfaces are presented in Figure 4.5. "water exclusion zone" is not present at the quartz (001), sapphire (001), and gibbsite (001) surfaces, which confirms a previous MDS study (Wang et al., 2006). Compared to the hydrophobic surfaces, interfacial water molecules at the quartz (001), sapphire (001), and gibbsite (001) surfaces have much stronger interactions with the surface. For the quartz (001) surface, water molecules in the first water layer are highly ordered and form hydrogen bonds with oxygen atoms at the quartz (001) surface, and the water molecules in the second water layer form hydrogen bonds with the first water layer.

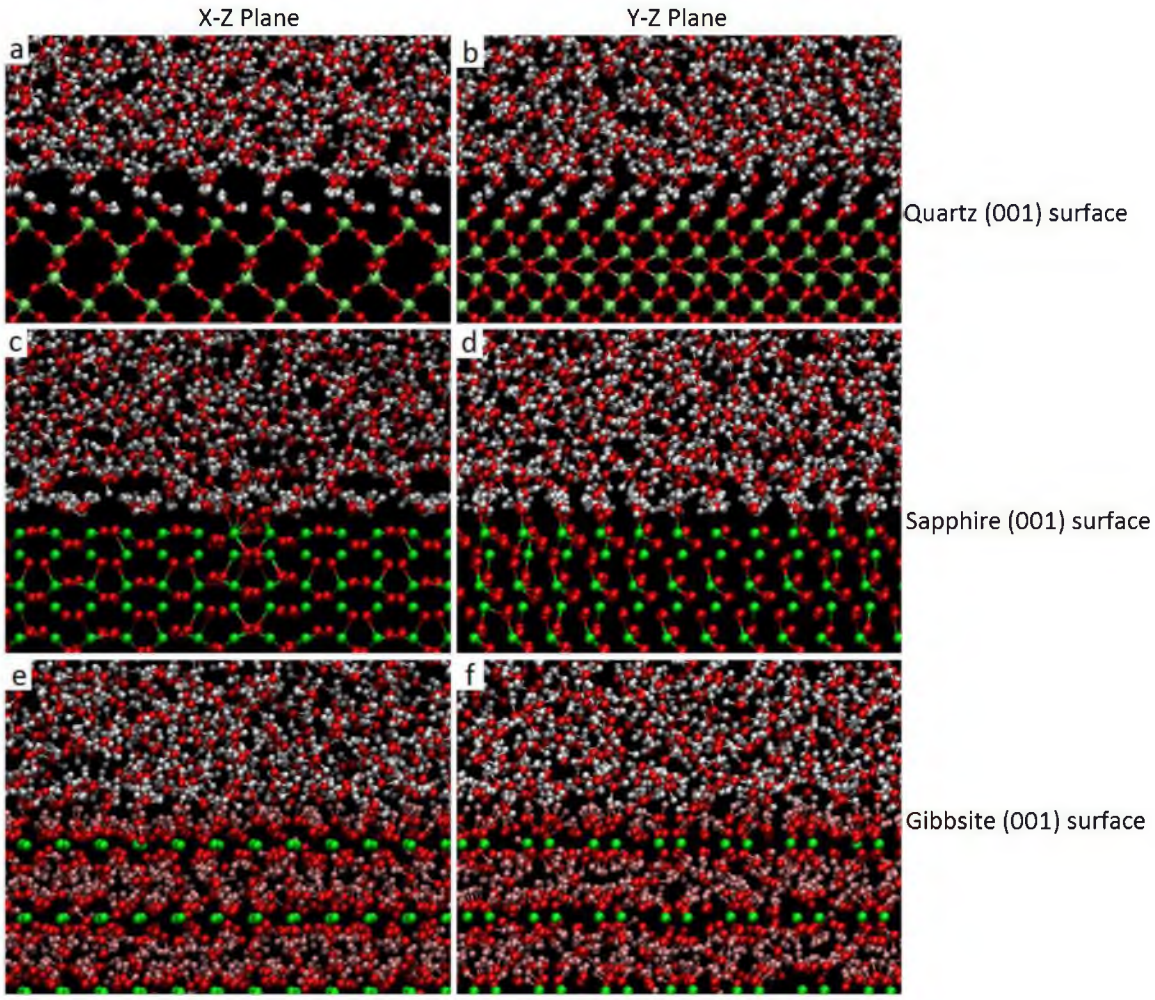

Figure 4.5. MDS snapshots of mineral/water interfaces: (a) quartz (001) surface; (b) sapphire (001) surface; (c) gibbsite (001) surface. The simulation time is at 2 ns. The atoms' color code is as follow: lime, Si; green, Al; red, O; white, H in water; pink, H in OH group.

The interfacial water molecules at the sapphire (001) surface also form hydrogen bonds with the surface oxygen atoms. Some oxygen atoms at the sapphire (001) surface are even attracted out of the sapphire crystal, because of the strong hydrogen bonding interaction from the interfacial water molecules. For the gibbsite (001) surface, interfacial water molecules have strong interactions with OH groups at the surface, instead of surface oxygen. Because of the vibration of OH groups at the gibbsite (001) surface, the

interfacial water molecules at gibbsite (001) surface appear to be less ordered than at the quartz (001) and sapphire (001) surfaces as revealed from the MDS snapshot. Quantitative analysis, such as water dipole orientation and residence time, will provide further information about of interfacial water molecules.

4.2.2 Number Density Profile

The number density profiles for water molecules at the quartz (001), sapphire (001), and gibbsite (001) surfaces are shown in in Figure 4.6. Positions of the quartz (001), sapphire (001), and gibbsite (001) surfaces are defined as the average position of the surface oxygen atoms or OH groups. Position of the oxygen atom in the OH group is used to represent the position of the OH group, due to the much larger atomic mass of oxygen compared to hydrogen.

For the quartz (001) surface, two sharp peaks of water number density which are 0.5 Å and 1.5 Å away from the surface represent the first and second water density layer of the graphite/water interface, respectively.

The distance between the first water density layer and solid surface for the quartz (001) surface is much smaller than the hydrophobic graphite (001) surface, which is 3.2 Å as revealed in Figure 4.2.

These results indicate that the interfacial water molecules have much stronger interaction, such as hydrogen bonding, with the quartz (001) surface than with the graphite (001) surface, which is consistent with the snapshots in Figure 4.5. In addition, according to the number density distribution of surface oxygen, the surface oxygen atoms keep vibrating at the quartz (001) surface.

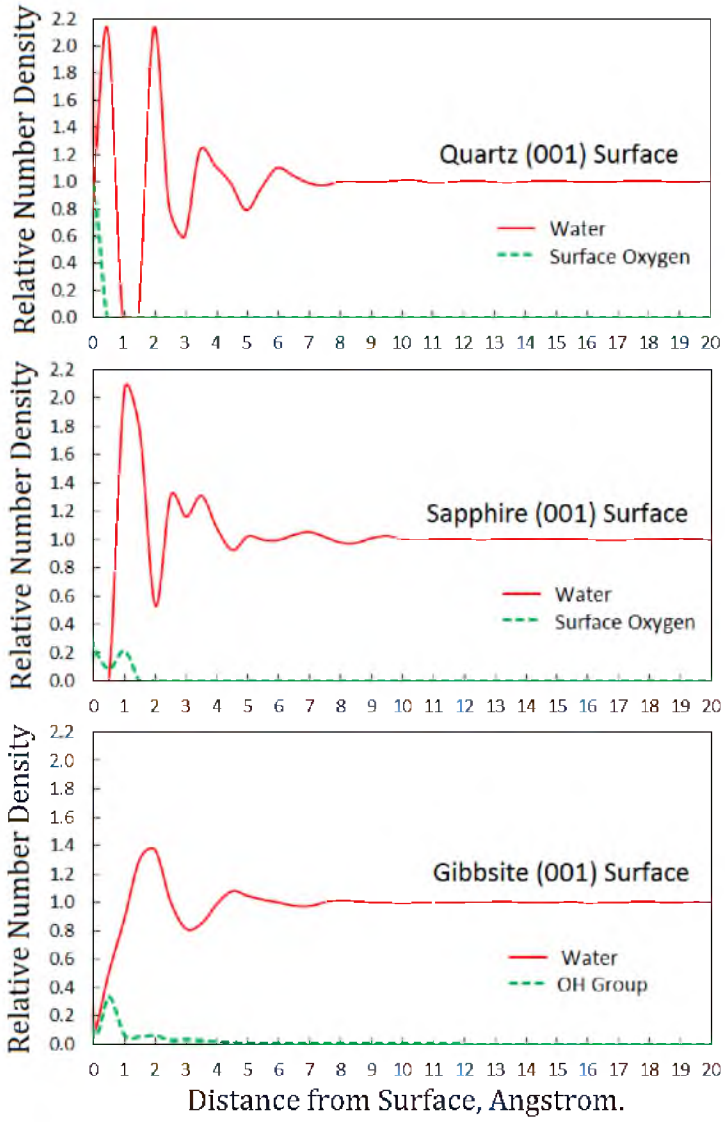

Figure 4.6. Relative water number density profiles at selected mineral surfaces: (a) quartz (001) surface; (b) sapphire (001) surface; (c) gibbsite (001) surface.

The distance between the first water density peak and sapphire (001) surface is about 1 Å, which is also much smaller than the hydrophobic graphite (001) surface and indicates the strong interaction, such as hydrogen bonding, between the interfacial water molecules and sapphire (001) surface. The number density distribution of surface oxygen show the vibration of the surface oxygen and some surface oxygen atoms are attracted toward the water phase for about 1 Å. This confirms the snapshots in Figure 4.5.

Compared to the quartz (001) and sapphire (001) surface, the first water density peak at the gibbsite (001) surface is relatively short and wide. The distance between the first water density peak and gibbsite (001) surface, the average position of surface OH groups, is about 2 Å, which is consistent with the previous MDS study (Wang et al., 2006). However, due to vibration and diffusion of OH groups at the gibbsite (001) surface, there is an OH group peak of 0.5 Å away from the gibbsite (001) surface, which is less 1.5 Å away from the first water density peak. This indicates that the interfacial water molecules form hydrogen bonds with the OH groups at the gibbsite (001) surface, which confirms the snapshots in Figure 4.5. In addition, according to the number density distribution of OH groups, the surface OH groups at the gibbsite (001) surface diffuse away from the surface for about 5 Å or further.

4.2.3 Water Dipole Orientation

The water dipole moment and hydrogen position relative density distributions for the quartz (001), sapphire (001), and gibbsite (001) surfaces are shown in Figure 4.7. The positions of the first and second water density layers for the quartz (001), sapphire (001), and gibbsite (001) surfaces are consistent with the water number density analysis.

For the first water layer at the quartz (001) surface, according to the large peak at 40° for the α angle and the large peak at 50° for the β angle, both the dipole moment and one hydrogen atom of the water molecules are oriented around 45° to the surface normal, which is exactly the orientation of first layer water molecules shown by snapshot (a) in Figure 4.5. This indicates that the water molecules of the first water layer form highly ordered hydrogen bonds with the oxygen atoms at the quartz (001) surface.

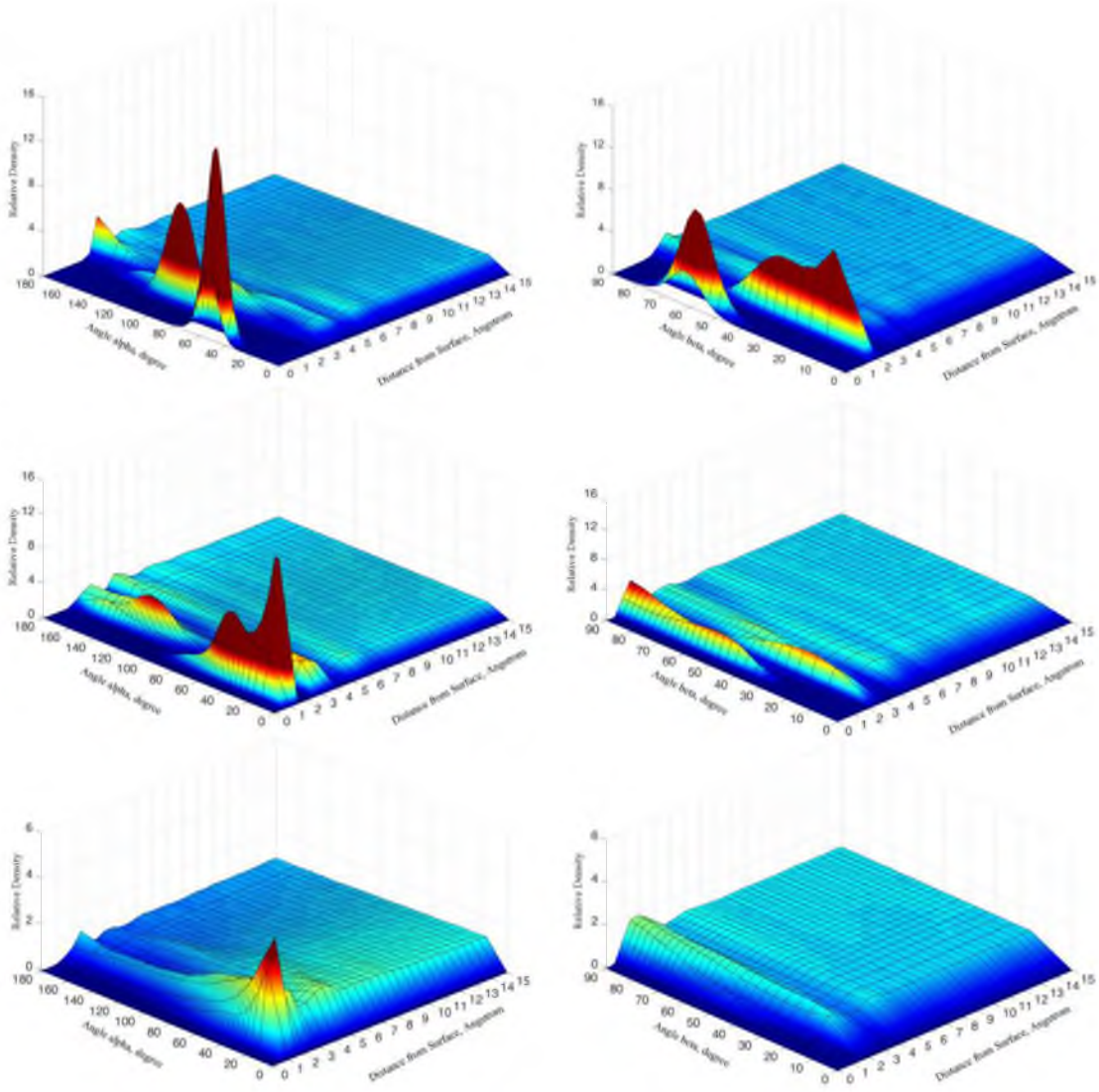

Figure 4.7. Water dipole moment (angle α) and hydrogen position (angle β) relative density distribution along the surface normal at selected mineral surfaces: (a) quartz (001) surface; (b) sapphire (001) surface; (c) gibbsite (001) surface.

In addition, for the second water layer at the quartz (001) surface, the large peak at 90° for the α angle and the large peak at 10 to 30° for the β angle indicate that the second layer water molecules have their dipole moment parallel to the surface and one hydrogen atom oriented toward the first water layer. Thus, the second layer water molecules form ordered hydrogen bonds with the first water layer, which is also consistent with the snapshots and water number density analysis.

According to the large peak at 10° to 40° for the α angle and the large peak at 50° to 90° for the β angle, the first layer of water molecules at the sapphire (001) surface have their dipole moment with one hydrogen atom tilted to the surface. This indicates that the first layer of water molecules have hydrogen bonding interaction with the oxygen atoms at the sapphire (001) surface. The dipole orientation and hydrogen positions of the water molecules in the subsequent layers at the sapphire (001) surface are relatively complex, but the results reveal that the water molecules adjacent to the first water layer have strong interaction with the first water layer.

For the first layer water molecules at the gibbsite (001) surface, the angle β is a uniform distribution from 0° to 90°, but the angle α has a large peak at 10°. Thus, the water dipole moment for the first layer of water molecules is almost parallel to the surface normal, so the oxygen atom of the water molecules are toward the gibbsite (001) surface, forming hydrogen bonds with the OH groups at the gibbsite (001) surface. The hydrogen bonding analysis of interfacial water at the gibbsite (001) surface should have similar results.

4.2.4 Water Residence Time

Water residence time for the quartz (001), sapphire (001), and gibbsite (001) surfaces are listed in Table 4.4. Positions of the first peak of water residence time at the quartz (001), sapphire (001), and gibbsite (001) surfaces confirm the water number density analysis. The magnitude of the residence time for the selected oxide surfaces is much larger than for the hydrophobic graphite (001) surface and OTS monolayer (less than 10 ps), as reported in Table 4.2.

Table 4.4 Interfacial Water Residence Times for Quartz (001), Sapphire (001), and Gibbsite (001) Surfaces

Mineral Surface	First Peak for Water Residence Time	
	Distance from Surface (Å)	Magnitude (ps)
Quartz (001) Surface	1.0	44.6
Sapphire (001) Surface	2.0	41.8
Gibbsite (001) Surface	1.5	15.0

This is consistent with the relatively stronger interactions, such as hydrogen bonding, between the interfacial water molecules and the quartz (001), sapphire (001), and gibbsite (001) surfaces, as revealed by the water number density and dipole orientation analysis. Due to the hydrogen bonding interaction between the interfacial water molecules and oxygen atoms/OH groups at the selected oxide mineral surfaces, water molecules are attracted to stay for a relatively longer time period at the interface. According to previous MDS studies, the water residence time at other hydrophilic mineral surfaces, such as the muscovite (001) and sylvite (100) surfaces, are around 20 ps (Wang et al., 2013; Yin, 2012). Thus, based on the MDS results, the magnitude of the water residence time at a hydrophilic mineral surface is expected to be greater than 10 ps.

The water residence time for the gibbsite (001) surface is larger than 10 ps but smaller than for the quartz (001) and sapphire (001) surfaces. According to the snapshots in Figure 4.5 and number density profiles in Figure 4.6, the OH groups at the gibbsite (001) surface have relatively more active vibration and diffusion than the oxygen atoms at the quartz (001) and sapphire (001) surfaces, which may cause the interfacial water molecules to be more mobile and to have a smaller residence time.

4.2.5 Hydrogen Bonding Analysis

Distribution of the average number of hydrogen bonds per water molecule along the surface normal for the quartz (001), sapphire (001), and gibbsite (001) surfaces is shown in Figure 4.8. For the quartz (001), sapphire (001), and gibbsite (001) surfaces, total number of hydrogen bonds per water of the bulk water molecules about 1 nm from the surface is around 3.35, which confirms the value of 3.5 from the previous MDS study (Nieto-Draghi et al., 2003).

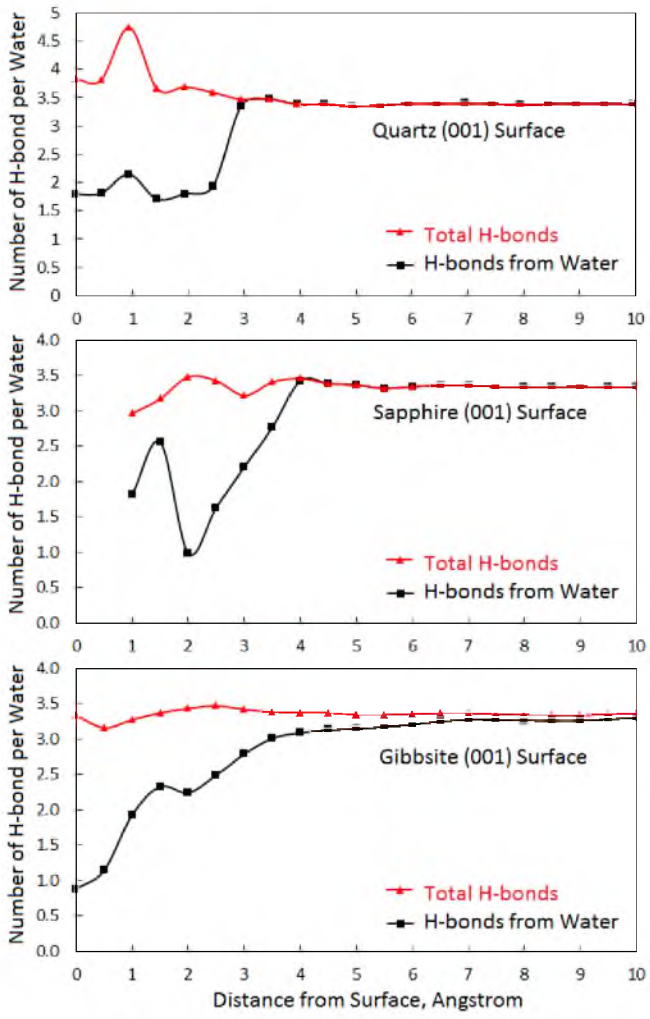

Figure 4.8. Distribution of hydrogen-bonding number per water molecule along the surface normal for selected mineral surfaces: (a) quartz (001) surface; (b) sapphire (001) surface; (c) gibbsite (001) surface.

When approaching the quartz (001) and sapphire (001) surfaces, the number of hydrogen bonds per water molecule from neighboring water molecules decreases from 3.35 to around 2, due to the decrease of water coordination number at the solid/water interface. However, the oxygen atoms at the quartz (001) and sapphire (001) surfaces are perfect hydrogen bond doners and accepters, so oxygen atoms at the quartz (001) and sapphire (001) surfaces form hydrogen bonds with the interfacial water molecules. The total number of hydrogen bonds for a water molecule includes the number of hydrogen bonds formed with the neighboring water molecules and the number of hydrogen bonds formed with surface oxygen atoms or OH groups. As a result, the first layer water molecules 1 Å away from the sapphire (001) surface have similar total hydrogen bonds per water with the bulk water molecules, and the first layer water molecules at the quartz (001) surface have a total of 4.7 hydrogen bonds per water, which is consistent with the previous study (Wang et al., 2012).

For the gibbsite (001) surface, the hydrogen bonds per water from other water molecules drop to 2 at 1 Å from the surface and less than 1 at the position of the surface. The OH groups at the gibbsite (001) surface are very good doners and acceptors of hydrogen bonds, which can bind the first water molecule to form H_3O_2- bihydroxide anions (Abu-Dari et al., 1979). Thus, for the gibbsite (001) surface, the total number of hydrogen bonds per water remains around 3.35, the bulk value, even when reaching the gibbsite (001) surface. Further, according to the number density analysis, because of the active vibration of the OH groups at the gibbsite (001) surface, some OH groups diffuse toward the water phase. The diffused OH groups form hydrogen bonds with water molecules, and make contributions to the total number of hydrogen bonds per water

further away from the gibbsite (001) surface, as revealed by the difference between the total number of hydrogen bonds and hydrogen bonds from other water from 4 Å to 10 Å away from the surface.

4.3 Summary

Compared to the experimental contact angle results, MD simulations of a water drop spreading on the selected hydrophobic or hydrophilic mineral surfaces provide relatively accurate predictions of the contact angle, indicating the reliability of the MDS force field parameters for the selected hydrophobic and hydrophilic surfaces.

From the MDS snapshots of the interfacial water at selected hydrophobic or hydrophilic mineral surfaces, a "water exclusion zone" is found between the interfacial water and selected hydrophobic mineral surfaces, while such a zone does not exist at the selected hydrophilic mineral surfaces. This is confirmed by the water number density analysis of the selected hydrophobic and hydrophilic mineral surfaces. The distance between the first water density peak and the selected hydrophobic mineral surfaces (about 3 Å) is comparably larger than the selected hydrophilic mineral surfaces (about 1 Å). Surface roughness has a great influence on the water number density analysis of interfacial water molecules.

According to the water dipole orientation analysis, the interfacial water molecules at the selected hydrophilic mineral surfaces form hydrogen bonds with the surface oxygen atoms or OH groups, while the interfacial water molecules at the selected hydrophobic mineral surfaces have a greater degree of freedom with some OH bonds vibrating freely.

Position of the first peak of water residence time is closer to the selected hydrophilic

mineral surfaces than the selected hydrophobic mineral surfaces. Further, the magnitude of interfacial water residence time at the selected hydrophilic mineral surfaces (over 10 ps) is comparably larger than at the selected hydrophobic mineral surfaces (less than 10 ps).

Based on the results of hydrogen bonding analysis, the oxygen atoms or OH groups at the selected hydrophilic mineral surfaces form hydrogen bonds with the interfacial water molecules, so the total number of hydrogen bonds per water for the interfacial water molecules at the selected hydrophilic mineral surfaces is similar to the bulk water (3.35 hydrogen bonds per water). However, at the selected hydrophobic mineral surfaces, due to the lack of hydrogen bond accepters and the decrease of water coordination number, the first layer of water molecule only have about half the number of hydrogen bonds compared to bulk water.

MDS interfacial water features, including water number density analysis, water dipole orientation, water residence time, and hydrogen bonding analysis, provide molecularly detailed information of interfacial water molecules at the selected hydrophobic and hydrophilic mineral surfaces, which can describe and explain the hydrophobic or hydrophilic surface state of these mineral surfaces.

CHAPTER 5

SUM FREQUENCY VIBRATIONAL SPECTROCOPY

5.1 Internal Reflection

In this SFVS study, wavelengths of the IR, visible, and SFG signal are 2300nm, 532nm, and 432 nm, respectively. An internal reflection system was set up for the SFVS study of interfacial water at selected mineral/water interfaces (Irvine and Pollack, 1968). As is shown in Figure 5.1, a hemi-cylinder of the selected mineral crystal with the diameter of 25mm is held at the water surface on a Teflon cell to create the selected mineral/water interface. An EKSPLA, Ltd, sum-frequency generation spectrometer was used in this dissertation research. A previous study has described the laser system (Nickolov et al., 2004).

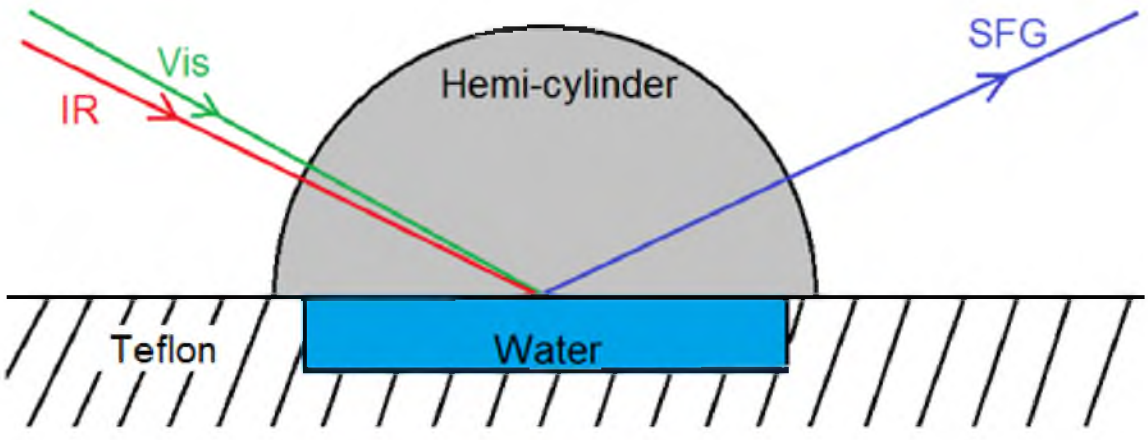

Figure 5.1. Schematic view of internal reflection system for SFVS.

The incident angles at the selected mineral/water interface for the IR and visible beam radiations are 66° and 60°, respectively. Energy of the IR and visible beams are 500 μJ andn160 μJ, respectively. As is shown in Figure 5.1, the pulsed IR and visible beams are overlapped spatially at the selected mineral/water interface. The reflected SFG signal is collected at 65°. The spectra were taken in SSP polarization (IR, visible, sum-frequency) then normalized to the IR and visible energies. Each data point is an average of 40 laser shots, and the data are collected at a 5 cm^{-1} increment. The SFVS spectra were processed with the Win-IR software package from Bio-Rad Lab., Inc. for baseline correction and fitting with Gaussian curves.

5.2 Selected Hydrophobic Surfaces

The OH stretching bands of interfacial water molecules at selected mineral surfaces are examined with the internal reflection system. Three characteristic peaks for the OH vibration, including 3200 cm^{-1}, 3450 cm^{-1}, and 3700 cm^{-1}, have been reported in previous SFVS studies of solid/water interfaces to describe the interfacial water structures (Freysz et al., 1994; Kim et al., 2001; Ostroverkhov et al., 2004; Shen et al., 2001). Different extents of intermolecular hydrogen bonding have been assigned to the peaks. The 3200 cm^{-1} peak represents the OH stretching from the strong hydrogen bonded water molecules, which is also known as "ice-like" water (Richmond, 2002). The 3450 cm^{-1} peak indicates the asymmetrically bonded water molecules with either asymmetric or bifurcated hydrogen bonds, i.e., the "liquid-like" water. The relatively sharp 3700 cm^{-1} peak is from vibrations of the free or nonhydrogen bonded OH groups, which is the weakly coupled or uncoupled OH stretching mode of straddling interfacial water.

The SFVS spectrum of the interfacial water molecules at an OTS monolayer coated on a quartz substrate is shown in Figure 5.2. Two sharp peaks of relatively high intensity at 2875 cm^{-1} and 2935 cm^{-1} represent the CH_3 symmetric stretching and CH_3 fermi resonance, respectively, which confirms the monolayer structure of OTS molecules adsorbed at the quartz surface.

A sharp peak at 3700 cm^{-1}, which is characteristic for the free or nonhydrogen bonded OH groups, is found in the SFVS spectrum of interfacial water molecules at the OTS monolayer. This is consistent with a previous SFVS study of the OTS-water interface, in which it has been concluded that the 3700 cm^{-1} "free OH" peak is related to the hydrophobic surface state of the OTS monolayer (Shen et al., 2001). Contact angle for the OTS monolayer is 105° by the captive bubble method, indicating a hydrophobic surface state of the OTS monolayer.

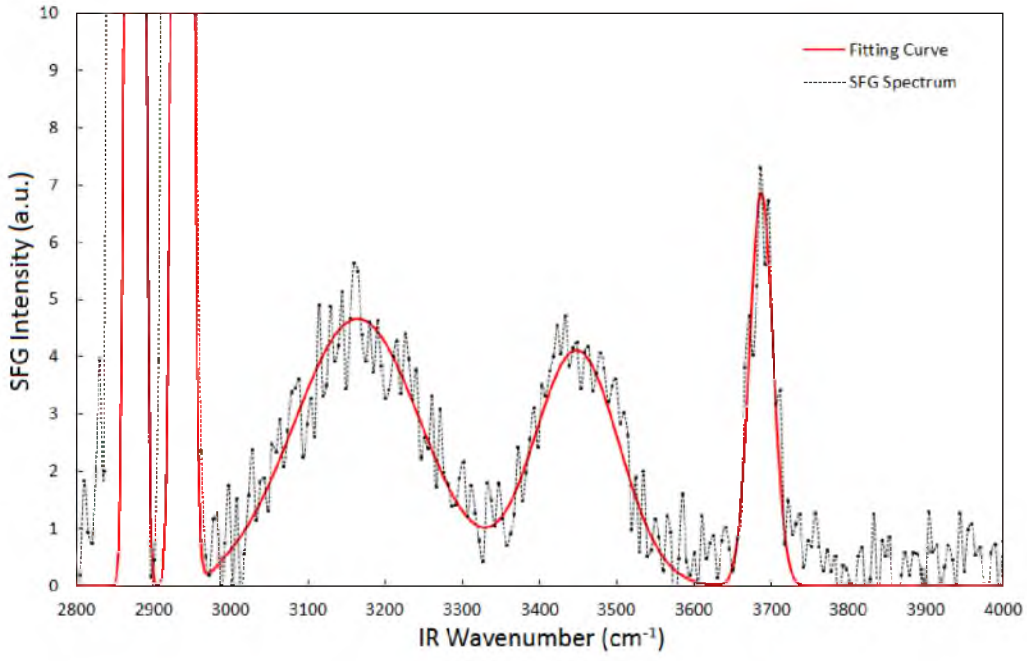

Figure 5.2. SFVS spectra (SSP) of OTS monolayer/water interface (spectra normalized to lasers' energy, natural pH = 5.7, ionic strength is not controlled).

Due to the lack of hydrogen bonding doners from the carbon chain of the OTS molecules, the interfacial water molecules at the OTS monolayer only have relatively weak VdW interactions with the surface. Thus, OH groups of the straddling interfacial water molecules are dangling at the OTS-water interface and characterized by the 3700 cm^{-1} "free-OH" peak in the SFVS spectrum. The SFVS spectrum confirms the MDS results reported in section 4.1 that the interfacial water molecules have "free OH" vibrations at the OTS monolayer.

In addition, there are two relatively small peaks at 3200 cm^{-1} and 3450 cm^{-1} (around 60% of the 3700 cm^{-1} "free OH" peak in height) in the SFVS spectrum of interfacial water molecules at the OTS monolayer, representing the "ice-like" and "liquid-like" water, respectively. The OTS monolayer was coated on the quartz substrate using the self-assembling technique. The previous SFVS study has revealed that water molecules are able to diffuse into the self-assembled OTS monolayer on the quartz substrate, so the intermolecular hydrogen bonding associated with interfacial water molecules at the self-assembled OTS monolayer may be detected by SFVS (Shen et al., 2001).

The SFVS spectrum of interfacial water molecules at the graphite multilayer coated on the quartz substrate is shown in Figure 5.3. Compared to the self-assembled OTS monolayer, the 3200 cm^{-1} "ice-like" water peak and 3450 cm^{-1} "liquid-like" water peak for the graphite multilayer are much smaller, which are only about 25% of the 3700 cm^{-1} "free-OH" peak in height. This is consistent with a previous SFVS study of the water/graphene/Au interface (Politano and Chiarello, 2013). In the SFVS spectrum of the graphite multilayer, a small peak at 2925 cm^{-1} represents the CH_2 stretching, which might be the results of slight oxidation of the graphite multilayer.

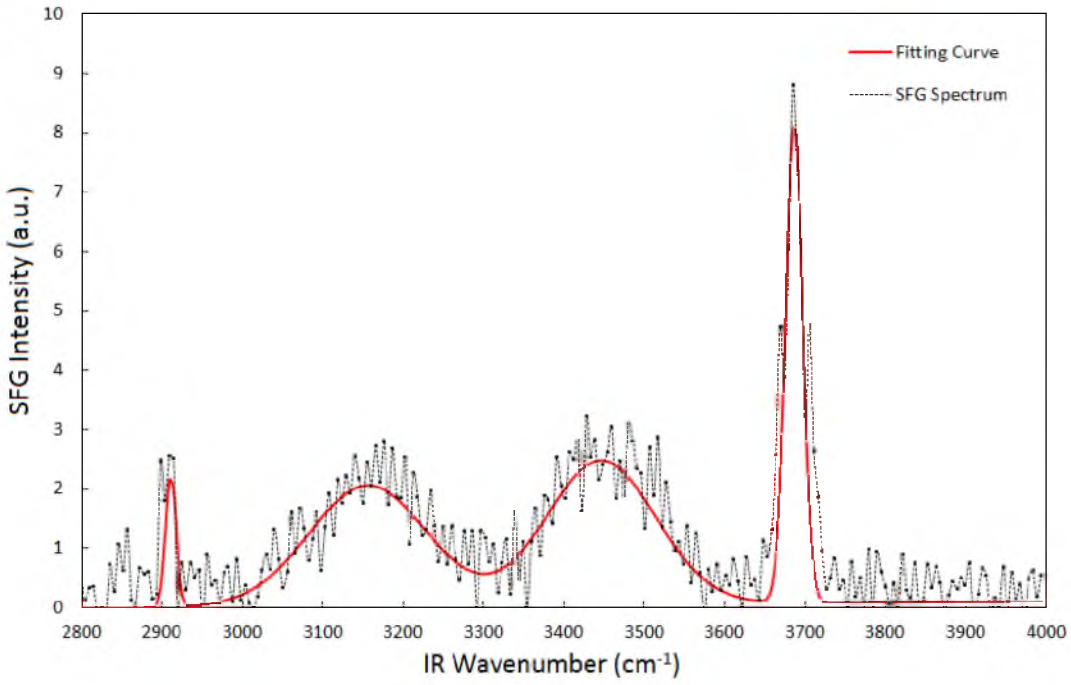

Figure 5.3. SFVS spectra (SSP) of graphite multilayer/water interface (spectra normalized to lasers' energy, natural pH = 5.7, ionic strength is not controlled).

Contact angle for the graphite multilayer is 93° by the captive bubble method, which indicates a hydrophobic surface state of the graphite multilayer and is close to the contact angle for the bulk graphite (Werder et al., 2003). Similar to the OTS monolayer, the graphite multilayer only has relatively weak VdW interactions with the interfacial water molecules, so the nonhydrogen bonded interfacial water molecules at the graphite multilayer are characterized by the 3700 cm^{-1} "free-OH" peak in the SFVS spectrum.

The SFVS spectrum of interfacial water molecules at the graphite multilayer and OTS monolayer on the quartz substrate are consistent with the MDS interfacial water features of the selected hydrophobic mineral surfaces, such as the presence of "water exclusion zone" in the water number density profile, "free OH" vibration as revealed by water dipole orientation, relatively short interfacial water residence time, and less hydrogen bonds per water at the interface.

5.3 Selected Hydrophilic Surfaces

The SFVS spectra of the quartz/water interface at pH = 5.7 are shown in Figure 5.4. The quartz/water interface exhibits two main peaks at 3200 cm^{-1} and 3450 cm^{-1}, which is consistent with previous studies (Ostroverkhov et al., 2004; Shen et al., 2001). As is mentioned, the 3200 cm^{-1} and 3450 cm^{-1} peaks represent OH stretching modes of strongly hydrogen bonded water molecules and asymmetrically bonded water molecules with either asymmetric or bifurcated hydrogen bonds.

Existence of these two main peaks in the SFVS spectra of the quartz/water interface reveals that interfacial water molecules form strong hydrogen bonds between each other and possibly with the oxygen atoms at the quartz surface. This is consistent with the hydrophilic surface state of quartz, as revealed by experimental and MDS contact angles.

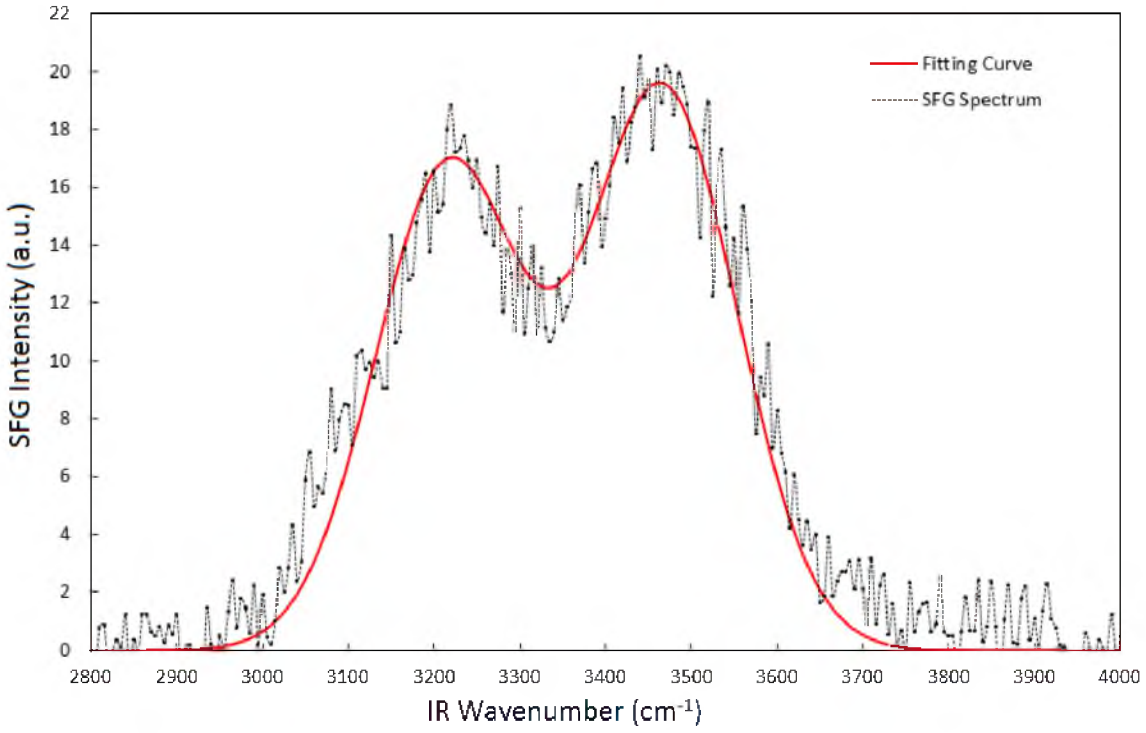

Figure 5.4. SFVS spectra (SSP) of quartz/water interface (spectra normalized to lasers' energy, natural pH = 5.7, ionic strength is not controlled).

According to the MDS, interfacial water molecules have comparably stronger interactions, such as hydrogen bonding, at the quartz (001) surface than at the selected hydrophobic surfaces. In addition, SFVS studies of interfacial water at other mineral surfaces , such as fluorite and sapphire, also reported the 3200 cm^{-1} peak "ice-like" water and 3450 cm^{-1} "liquid-like" water peak in the SFVS spectrum (Hsu and Dhinojwala, 2012; Zhang et al., 2008; Zhang et al., 2014). The main peaks at 3200 cm^{-1} and 3450 cm^{-1} representing the hydrogen bonding between interfacial water molecules and solid surface are characteristic for hydrophilic mineral surfaces.

The sapphire surface is considered to be hydrophilic but exhibits the 3700 cm^{-1} "free OH" peak in its SFVS spectrum (Hsu and Dhinojwala, 2012; Zhang et al., 2008); see Figure 5.5.

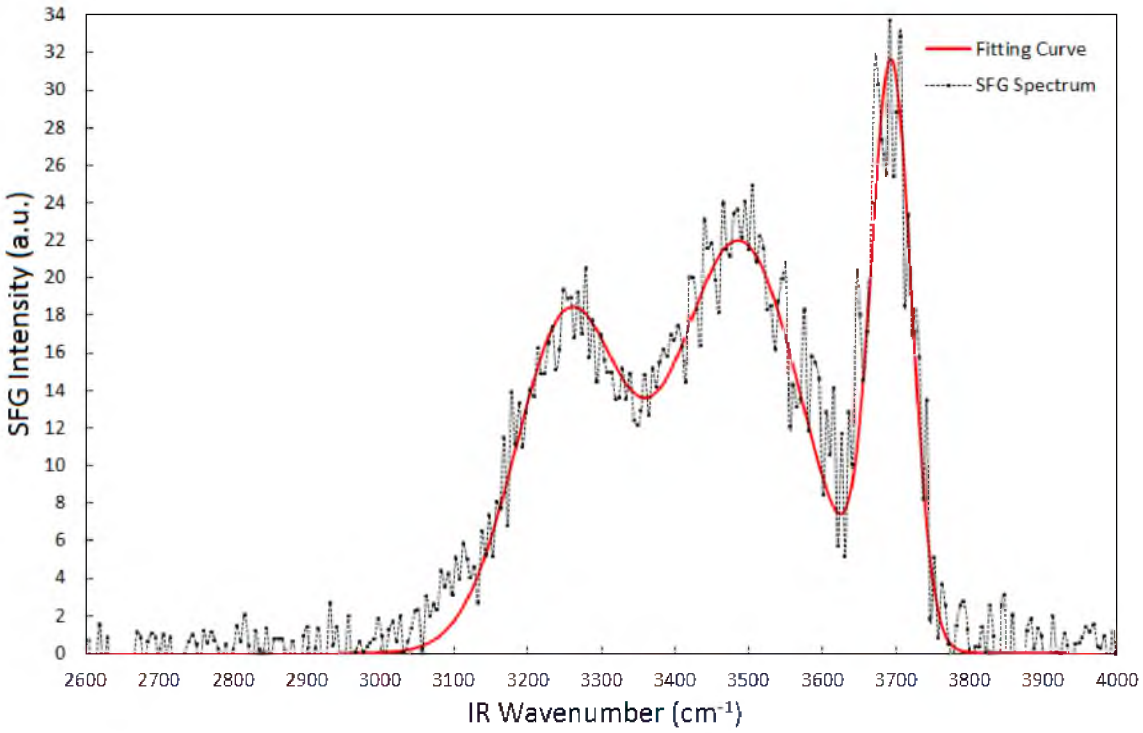

Figure 5.5. SFVS spectra (SSP) of sapphire/water interface (spectra normalized to lasers' energy, natural pH = 5.7, ionic strength is not controlled).

The sessile drop contact angle for the sapphire surface in this dissertation is 14°, which indicates some modest hydrophobic character, although the captive bubble contact angle is 0° (water film not break). Besides the 3200 cm^{-1} "ice-like" water peak and 3450 cm^{-1} "liquid-like" water peak which can be found in the SFVS spectrum of other hydrophilic surfaces, such as quartz and fluorite, a sharp peak at 3700 cm^{-1} presents in the SFVS spectrum of the sapphire/water interface, and represents the "free-OH" vibrations. However, the MDS interfacial water analysis indicates that the interfacial water molecules at the sapphire (001) surface have hydrogen bonding interactions with the surface oxygen atoms, and this is consistent with the hydrophilic surface state revealed by the captive bubble contact angle measurements. According to a previous SFVS study about the sapphire/water interface, this 3700 cm^{-1} peak represents the OH groups on the sapphire surface after hydration but not the OH groups from interfacial water molecules, which is proved by existence of this 3700 cm^{-1} peak in the SFVS spectrum of the hydrated sapphire/air interface (Zhang et al., 2008).

In order to clarify the origin of the "free-OH" signal detected at the sapphire/water interface, the sapphire/D_2O interface was studied by SFVS to compare with the sapphire/water interface. The SFVS spectrum of the sapphire/D_2O interface is shown in Figure 5.6. In addition to the 3700 cm^{-1} "free-OH" peak, a sharp peak exhibits at 2720 cm^{-1} in the SFVS spectrum of the sapphire/D_2O interface, representing the free DO stretching (Sovago et al., 2008). The bulk D_2O aqueous does not provide any OH vibration, so this "free OH" peak detected at the sapphire/D_2O interface should be the result of the vibration from OH groups on the hydrated sapphire surface. It is well known that OD and OH can have isotopic substitution (Fowler, 1974).

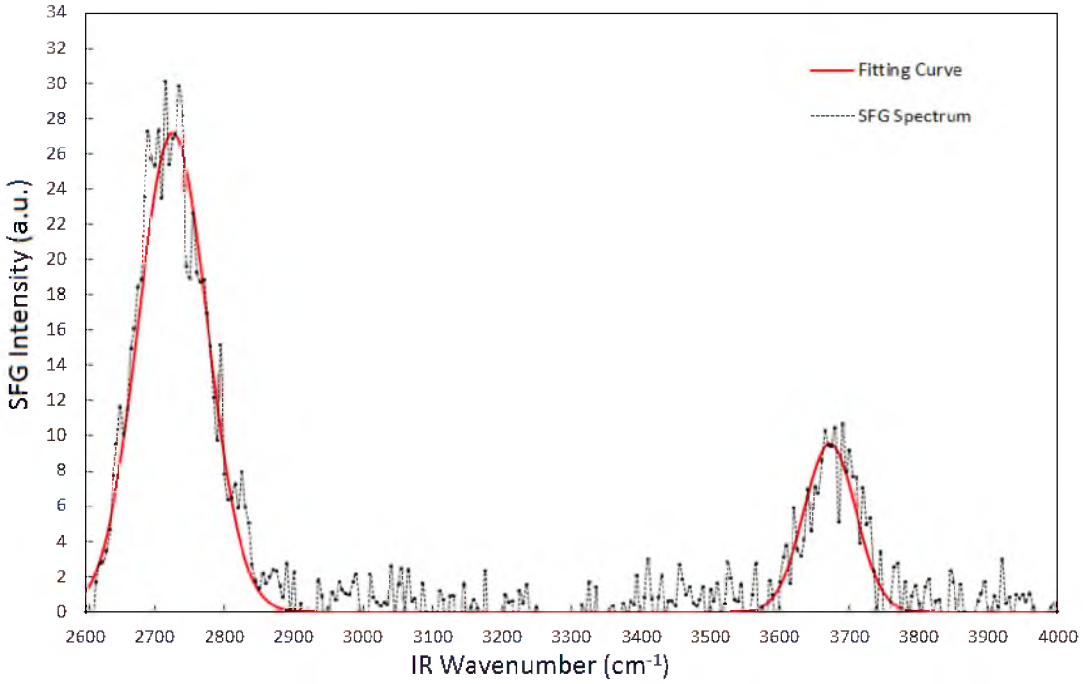

Figure 5.6. SFVS spectra (SSP) of sapphire/deuterium oxide interface (spectra normalized to energy, natural pH = 5.7, ionic strength is not controlled).

As a result, some OH groups at the hydrated sapphire surface were substituted by OD groups, and the "free-OD" vibration is detected at the sapphire/D_2O interface.

The structure of the hydrated sapphire surface is similar to gibbsite, which is an aluminum hydroxide mineral (Franks and Gan, 2007). According to the MDS results reported in section 4.2, the interfacial water molecules form hydrogen bonds with the gibbsite OH groups, but there are 2.85 times the number of gibbsite OH groups over the first layer water molecules at the gibbsite (001) surface. As a result, besides the OH groups hydrogen bonded with the interfacial water molecules, forming $H_3O_2^-$ bihydroxide anions (Abu-Dari et al., 1979), there are a large number of free or nonhydrogen bonded OH groups left at the gibbsite (001) surface. Similarly, the OH groups that have not formed hydrogen bonds with interfacial water molecules might be responsible for the "free-OH" vibration detected at the hydrated sapphire surface.

5.4 Summary

The interfacial water structures at the selected hydrophobic or hydrophilic surfaces have been studied by SFVS. For the selected hydrophobic surfaces, in addition to the 3200 cm^{-1} "ice-like" water and 3450 cm^{-1} "liquid-like" water peaks, representing the hydrogen bonding of interfacial water molecules, a 3700 cm^{-1} "free-OH" peak is found in the SFVS spectrum, which represents the nonhydrogen bonded vibration of interfacial water molecules because of the relatively weak interaction between the interfacial water molecules and hydrophobic surface such as might exist at the water exclusion zone. On the other hand, for the selected hydrophilic surfaces, two main peaks at the 3200 cm^{-1} and 3450 cm^{-1} indicate the hydrogen bond interaction not only among the interfacial water molecules but also between the interfacial water and selected hydrophilic surfaces, due to the presence of hydrogen bonding doners or accepters, such as oxygen atoms, at the selected hydrophilic surfaces. The SFVS spectra of the selected hydrophobic or hydrophilic surfaces validate the MDS interfacial water analysis that the interfacial water molecules have relatively weak interaction with the hydrophobic surface when compared the hydrophilic surface. SFVS spectra of the sapphire/water and sapphire/D_2O interfaces are reported to clarify that the origin of the "free-OH" vibration at the hydrated sapphire surface is not from interfacial water molecules, and that "free-OH" vibration is possibly from the OH groups that have not formed hydrogen bonds with interfacial water molecules at the hydrated sapphire surface, as revealed by the MD simulation of gibbsite/water interface.

CHAPTER 6

SESSILE DROP CONTACT ANGLES

In this chapter, both experimental and MDS sessile drop contact angles are reported for selected hydrophobic and hydrophilic surfaces and the results are discussed regarding spreading time, advancing/receding contact angles, and the effect of drop size.

6.1 Spreading Time

Spreading of mm sized water drops only takes a few microseconds as observed by high-speed cameras (Stapelbroek et al., 2014). For hydrophobic surfaces, an equilibrium contact angle is realized in a short time period. The effect of water evaporation can play an important factor which influences spreading time associated with sessile drop contact angle measurements. Under such circumstances, the volume of the water drop decreases and the sessile drop contact angle measurement becomes a receding contact angle measurement as time goes by, an effect which will be discussed in section 6.2. In sessile drop experiments, it is hard to maintain water vapor saturated atmosphere. However, for MDS sessile drop contact angle measurements where the atmosphere is in a saturated condition, the water drop volume remains constant, so the spreading time associated with the MDS sessile drop contact angle measurements can be explored without consideration of water evaporation.

Figure 6.1 shows the spreading of a water drop containing 1300 water molecules over a molybdenite (001) surface, which is an example of a hydrophobic mineral surface. After 0.5 ns, the water drop reaches equilibrium and reveals a sessile drop contact angle of about 80°, as is shown in Figure 6.2. These results confirm that the MDS sessile drop contact angles for selected hydrophobic mineral surfaces measured after a simulation time of 0.5 ns reach an equilibrium condition. Note that the "water exclusion zone" mentioned in Chapter 4 exists between the water drop and the molybdenite (001) surface, which indicates relatively weak interaction between the molybdenite (001) surface and interfacial water molecules.

In Figure 6.3, when a water drop with same number of water molecules spreads over the quartz (001) surface, the water drop spreads rapidly in 0.5ns and there is no "water exclusion" between the water drop and quartz (001) surface, which is consistent with the MDS results in Chapter 4. Unlike the interfacial water molecules at the molybdenite (001) surface which are "excluded" from the surface, during the spreading process, water molecules reach the quartz (001) surface and form hydrogen bonds with surface oxygen atoms. As a result, instead of reaching equilibrium, the water drop keeps spreading on the quartz (001) surface. As shown in Figure 6.3, the MDS sessile drop at the quartz (001) surface decreased by 4° from 0.5 ns to 1.0 ns, then it decreased slowly until reaching an equilibrated contact angle of 2° at 3.0 ns, when the water drop becomes a thin water film over the quartz (001) surface.

According to the MDS results for the spreading of a water drop at the quartz (001) surface, the MDS advancing contact angle of a hydrophilic mineral surface may need about 3 ns simulation time to reach an equilibrium condition.

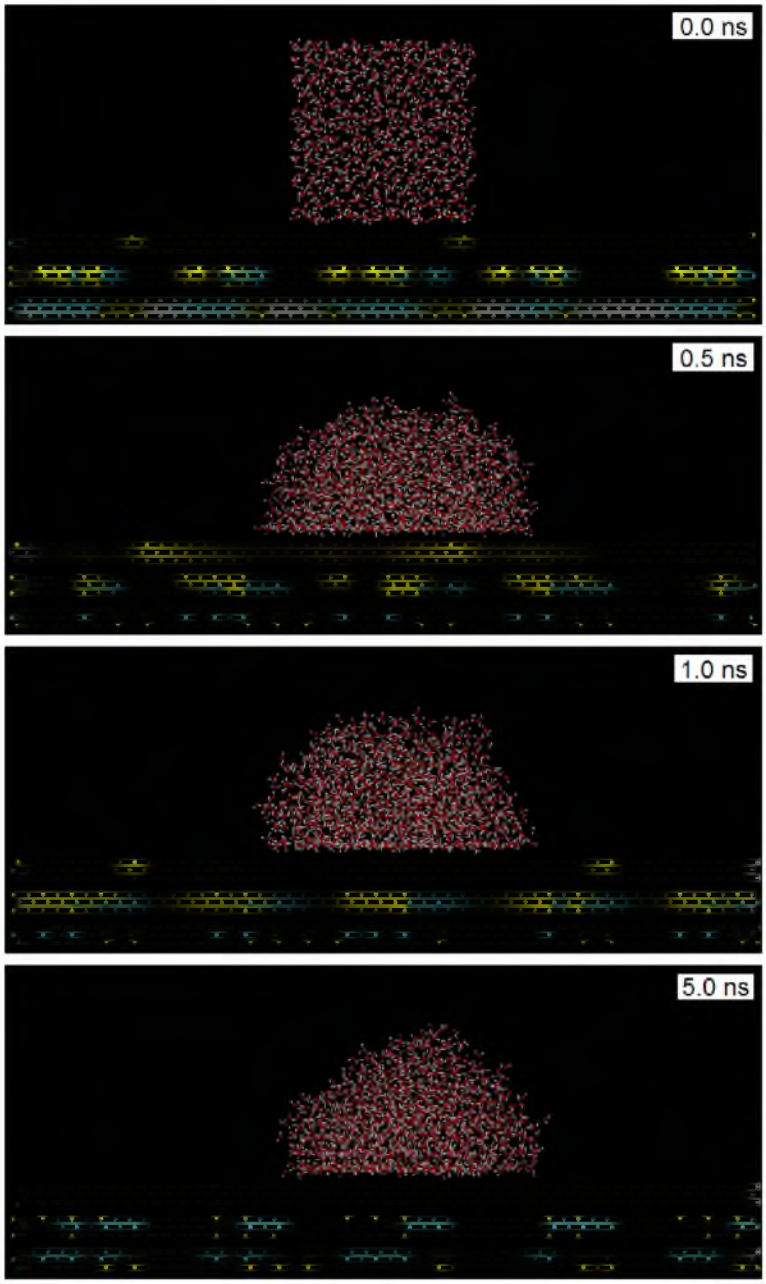

Figure 6.1. Water drop containing 1,300 water molecules at a molybdenite (001) surface from 0 ns to 5 ns. The atoms' color code is as follow: cyan, Mo; yellow, S; red, O; white, H.

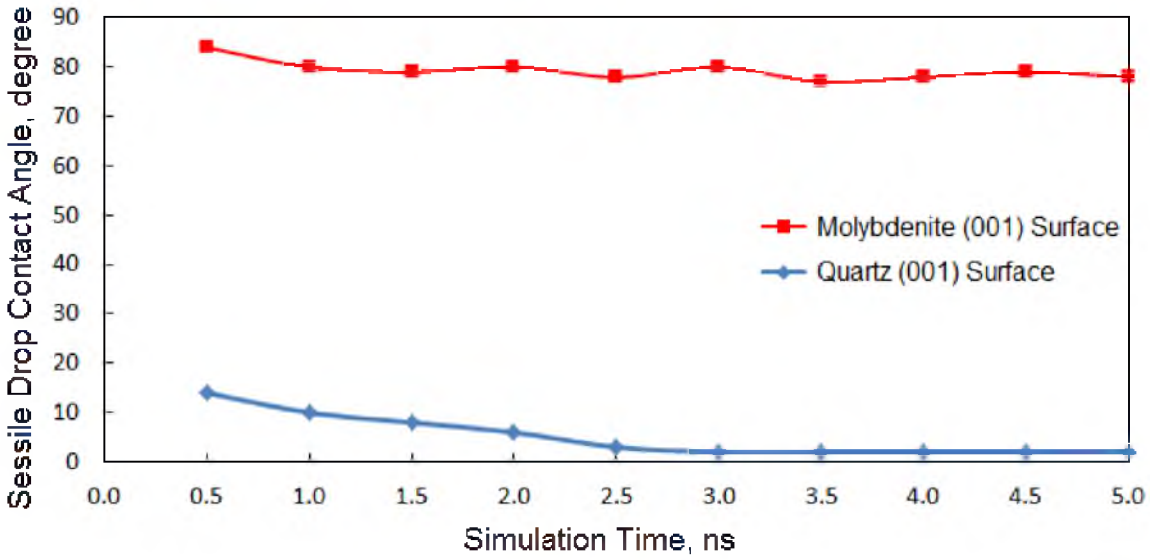

Figure 6.2. MDS advancing sessile drop contact angles for molybdenite (001) and quartz (001) surfaces versus simulation time.

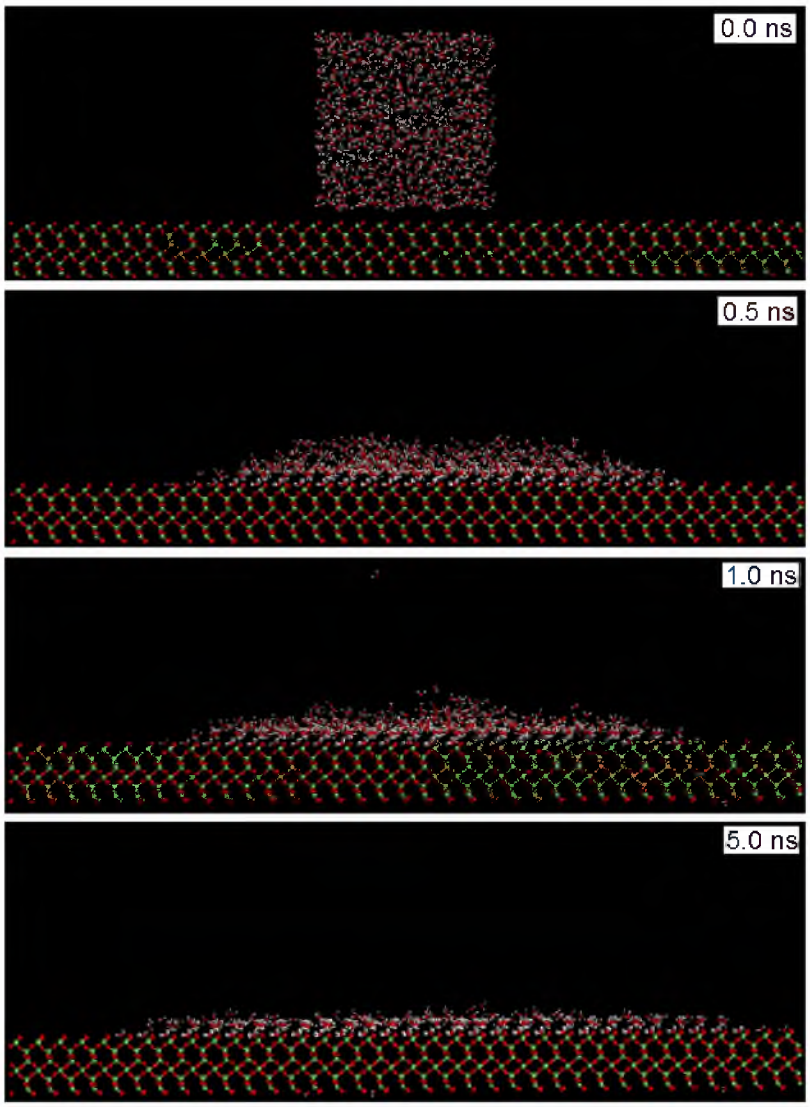

Figure 6.3. Water drop containing 1,300 water molecules at a quartz (001) surface from 0 ps to 5 ps. The atoms' color code is as follow: lime, Si; red, O; white, H.

However, in order to decrease the computational expenses, an equilibration time of 1ns was used as a compromise between simulation time and equilibrium for the MDS contact angle measurements of selected hydrophilic mineral surfaces.

6.2 Advancing and Receding Contact Angles

Advancing and receding sessile drop contact angles at the molybdenite (001) and quartz (001) surfaces for both experimental and MDS measurements are listed in Table 6.1. For the quartz (001) surface, the experimental sessile drop advancing and receding contact angles are very similar, but the simulation values have a difference of 7°. According to section 6.1, it takes about 3 ns to reach an equilibrium for the spreading of a water drop containing 1300 water molecules at the quartz (001) surface, which is a thin water film. The MDS advancing sessile drop contact angle for the quartz (001) surface was measured at 1 ns simulation time, when the equilibrium has not been reached. On the other hand, for the MDS receding sessile drop contact angle measurement at the quartz (001) surface, the initial state is a thin water film at the quartz (001) surface. Thus, after the same simulation time period (1 ns), the MDS receding sessile drop contact angle measured for the quartz (001) surface is smaller than the MDS advancing sessile drop contact angle.

Table 6.1. Advancing and Receding Sessile Drop Contact Angles of Molybdenite (001) and Quartz (001) Surfaces.

Mineral Surface		Sessile Drop Contact Angle, degree	
		MDS	Experimental Value
Molybdenite (001) Surface	Advancing	84	85
	Receding	80	68
Quartz (001) Surface	Advancing	9	5
	Receding	2	4

For the molybdenite (001) surface, it is as expected that the experimental advancing contact angle is larger than the experimental receding contact angle (Drelich et al., 1996), but the MDS advancing contact angle is close to the MDS receding contact angle. Figure 6.4 shows the snapshots from the MD simulation of receding sessile drop contact angle measurements. From 0 ns to 0.5 ns, the contact angle increases to a stable value and the water film returns to the expected water drop at the molybdenite (001) surface. After equilibration, the MDS receding water drop at the molybdenite (001) surface stops receding and reaches a stable state. These results are different from experimental results. Since water evaporation never stops, in the experimental receding contact angle measurements, the water drop continues to recede. Thus, the MDS advancing/receding sessile drop contact angles are similar to each other, but experimental values are different.

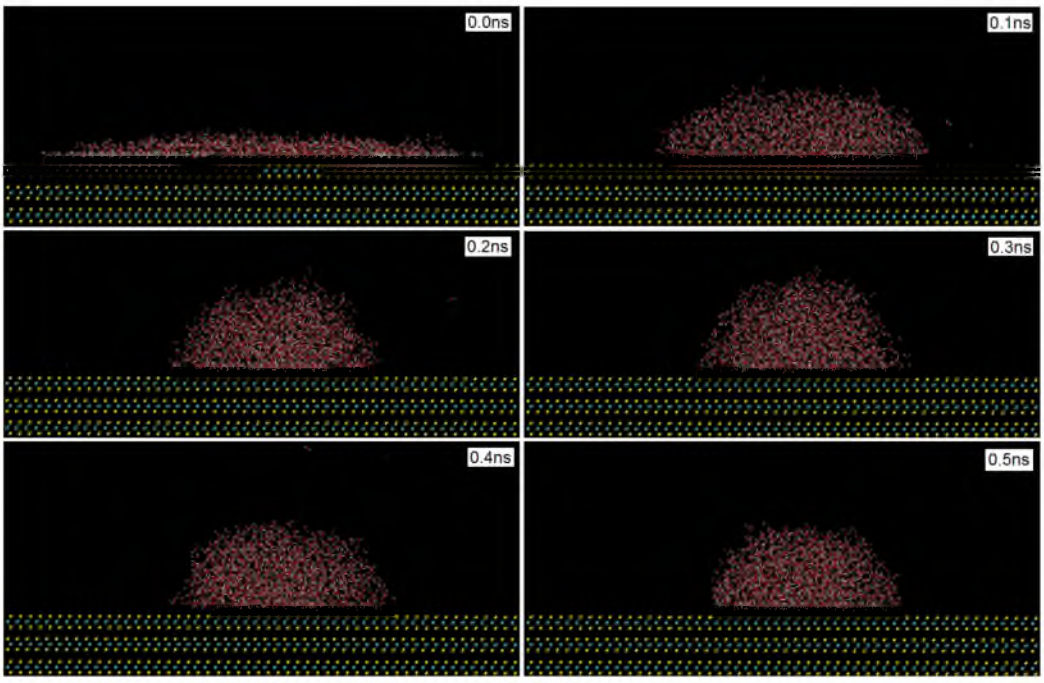

Figure 6.4. Snapshots of MDS receding contact angle of molybdenite (001) surface from 0ns to 0.5ns.

The simulation results of MDS advancing and receding sessile drop contact angles at the molybdenite (001) and quartz (001) surfaces indicate that the water drop shape (water drop vs. water film) does not have much influences on the results. This also confirms that the MDS sessile drop contact angles measured in this dissertation research which use a water drop as the initial state are capable to determine wettability of selected mineral surfaces.

6.3 Effect of Drop Size

One of the most distinct differences between MDS and experimental sessile drop contact angle measurements is the scale of the water drop. Though MDS can be used to measure the sessile drop contact angle, the droplet size is much smaller compared to the experiments, due to capacity limits of computational systems. Photographs of water drops of different size of the molybdenite (001) and quartz (001) surfaces are shown in Figure 6.5 and 6.6, respectively. The spreading of water on the quartz (001) surface does not show any difference with different water drop size, but the water drop with the diameter of 1.24 mm spreads better than other droplets with smaller sizes on the molybdenite (001) surface.

The experimental and MDS sessile drop contact angles of water drops with different sizes are listed in Figure 6.7. The droplet size does not have much effect on the hydrophilic quartz (001) surface in both MDS and experiments for the size ranges considered. For the molybdenite (001) surface, the MDS sessile drop contact angle is not influenced much by the drop size in the nm scale. However, at the mm scale, experimental results show that larger drop size results in a smaller contact angle.

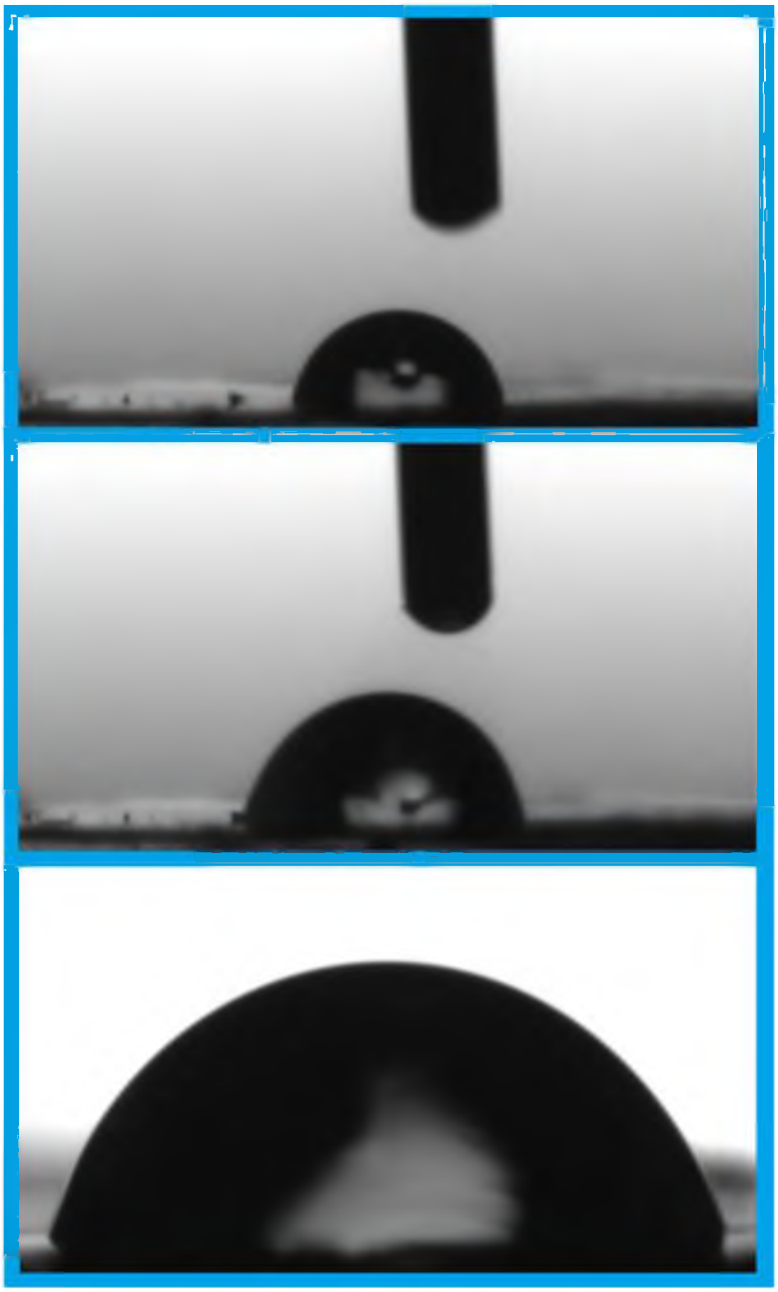

Figure 6.5. Water drop with diameters of 0.45mm (top), 0.58mm (middle), and 1.24mm (bottom) at the molybdenite (001) surface.

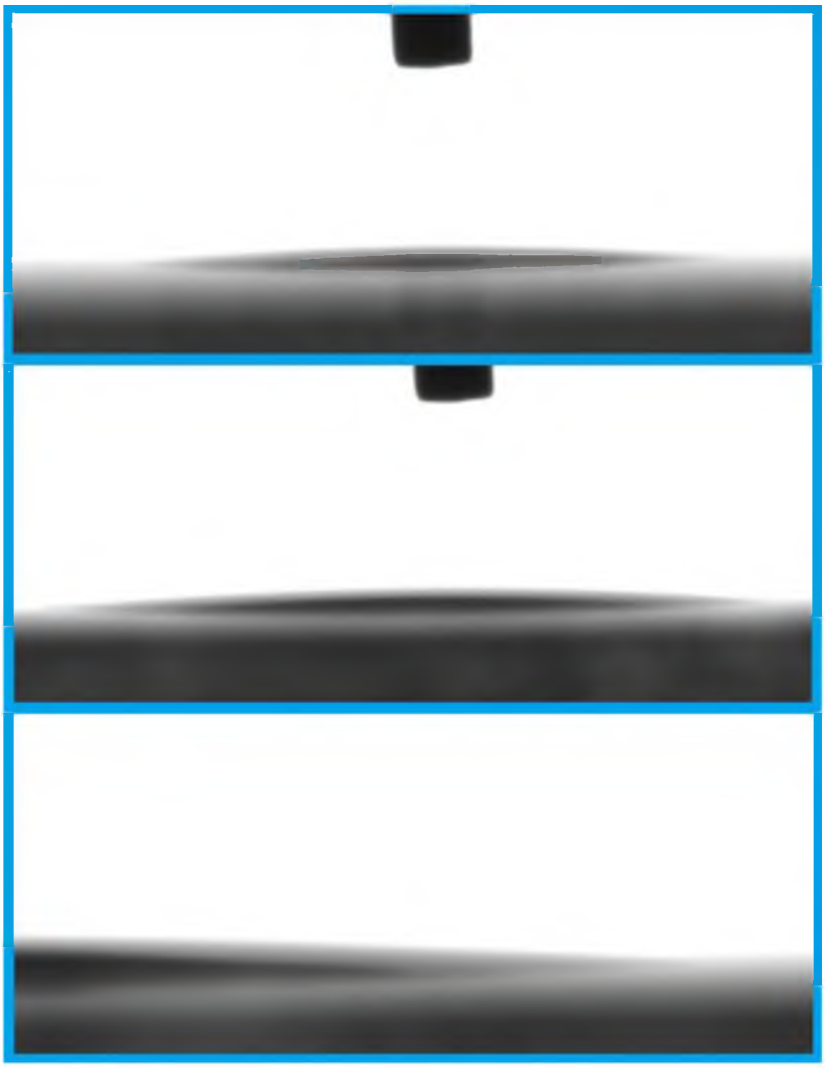

Figure 6.6. Water drop with the diameter of 0.45mm (top), 0.58mm (middle), and 1.24mm (bottom) at quartz (001) surface.

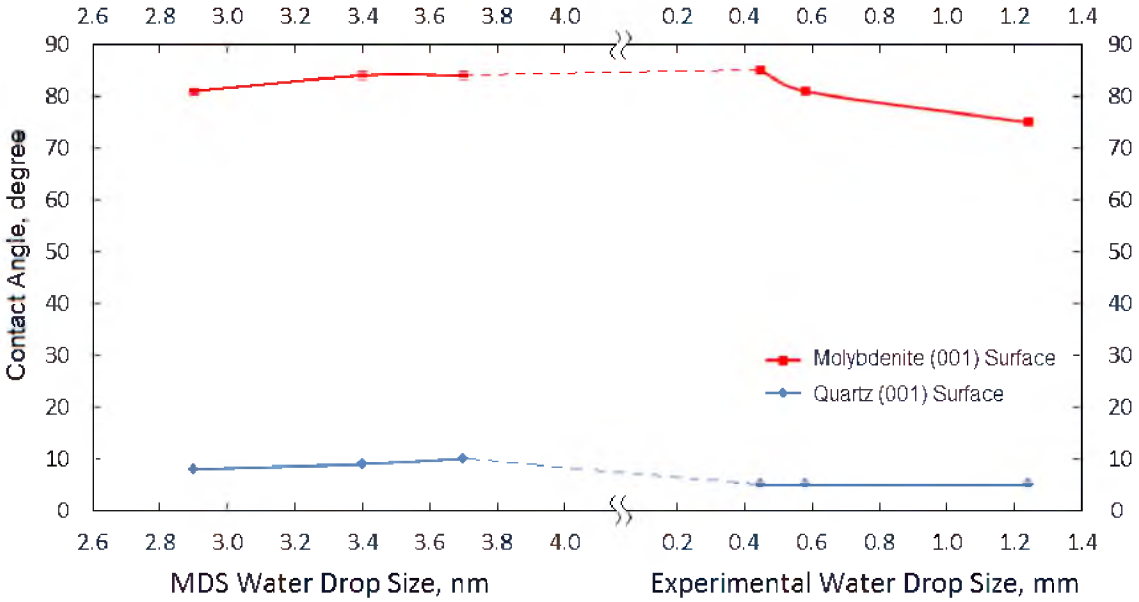

Figure 6.7. Comparison of sessile drop contact angles at molybdenite (001) and quartz (001) surfaces for MDS drops (nm) with experimental drops (mm).

This is consistent with previous experimental study about effect of drop size on sessile drop contact angles. The surface roughness makes a contribution to the decrease of contact angle with large droplet (Drelich and Miller, 1994).

To examine the surface roughness of the fresh molybdenite (001) surface used for sessile drop contact angle measurements, a SEM image of fresh molybdenite (001) surface prepared according to the procedures mentioned in section 2.2.3 is taken and shown in Figure 6.8.

There are two kinds of surface roughness shown at the molybdenite (001) surface. One is the step-type crystal defects in the middle of the SEM image. These are the edge surfaces of MoS_2 layers for the molybdenite crystal surface. According to previous study, the molybdenite edge surface is less hydrophobic than the molybdenite face surface (Chander and Fuerstenau, 1972). This may contribute to the smaller contact angle measured with the large drop at the molybdenite (001) surface.

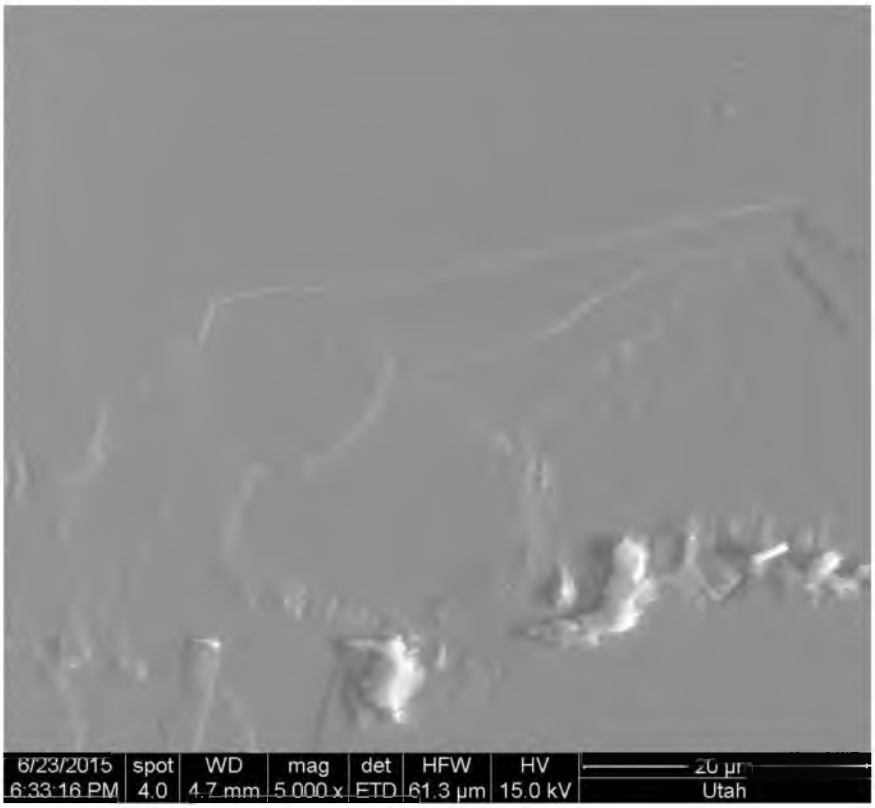

Figure 6.8. SEM image of natural molybdenite (001) surface.

In addition, several MoS_2 steps with the size of a few microns on the molybdenite (001) surface probably have even more influence on contact angle measurements, due to their comparably large dimensions. It is possible that the smaller water droplets avoid the steps on the fresh molybdenite (001) surface while larger droplets cannot. As a result, the large droplets give smaller contact angles than the smaller droplets.

6.4 Summary

According to the MDS results, a water drop containing 1300 water molecules spreading at the molybdenite (001) surface reached equilibrium after 0.5 ns, at which time a contact angle of about 80° was established. However, it takes about 3 ns simulation time to reach an equilibrium for spreading of the same water drop at the quartz (001)

surface.

In the case of molybdenite, the MDS advancing and receding contact angles for the molybdenite (001) surface have similar values, while the experimental advancing contact angle is larger than the experimental receding contact angle. For quartz, the experimental advancing and receding contact angles are the same, but the MDS advancing contact angle is 7° larger than the MDS receding contact angle.

The experimental contact angle of the molybdenite (001) surface decreases when the drop size increases, because of the increment of surface roughness. However, regardless of the influence from surface roughness, the experimental contact angles of mm size water drops and MDS contact angles of nm size water drops are similar for the selected hydrophobic mineral surface (MoS_2) and for the selected hydrophilic mineral surface (SiO_2).

CHAPTER 7

FILM STABILITY AND BUBBLE ATTACHMENT

In this chapter, MD simulations regarding the attachment of a nanometer scale nitrogen bubble at a hydrophobic mineral surface and the lack of attachment at a hydrophilic mineral surface are reported. Film stability is revealed and MDS bubble attachment contact angles are compared with experimental results as well as with sessile drop contact angles for the selected hydrophobic or hydrophilic mineral surfaces.

For the first time, MDS has been used to examine film stability between a bubble and selected mineral surfaces. In the case of a hydrophobic surface, the film is unstable, rupture occurs, followed by film displacement and bubble attachment. Finally, MDS contact angles are measured. The MD simulation system for film stability and bubble attachment includes a nitrogen bubble containing 900 nitrogen molecules in an aqueous phase containing around 70,000 water molecules and a mineral crystal containing around 20,000 atoms. The total number of atoms for the film stability and bubble attachment simulation is about a quarter of a million, which requires a relatively high computation capability to accomplish the simulation. Details of the MDS procedures for film stability and bubble attachment contact angle measurements are provided in section 3.5.2. In the MD simulations of bubble attachment at the selected mineral surfaces, there is no gravity and no buoyant force compared to experimental captive bubble contact angle

measurements, and MDS intermolecular interactions are represented by Lennard-Jones potentials and electrostatic interactions (Jones, 1924).

7.1 Bubble Attachment

The quartz (001) surface was selected as an example of hydrophilic mineral surfaces, and the molybdenite (001) surface was selected as an example of hydrophobic surfaces.

7.1.1 Quartz (001) Surface

Snapshots of the initial (0 ns) and final (1 ns) status of the MD simulation system for a nitrogen bubble containing 900 nitrogen gas molecules at the quartz (001) surface are shown in Figure 7.1. The atoms in the quartz crystal are represented by spheres with diameter of 0.8 Å. The nitrogen molecules are represented by relatively large spheres with diameter of 2.5 Å and water molecules are represented by lines. If the scales of nitrogen and water molecules were the same, it would be difficult to see the nitrogen bubble and visualize its behavior. However, the snapshots still clearly show that the film between nitrogen bubble and quartz surface is stable. Rupture does not occur at the quartz (001) surface, which is consistent with current experimental results presented in section 7.2 and a previous experimental contact angle study of the quartz surface (Subrahmanyam et al., 1999).

To have a better view of the simulation, a thin section with thickness of 2 nm in the middle of the simulation periodic box has been selected. Thin sections of the initial (0 ns) and final (1 ns) are shown in Figure 7.2, in which the quartz, nitrogen, and water molecules are represented by spheres with equal size (0.8 Å).

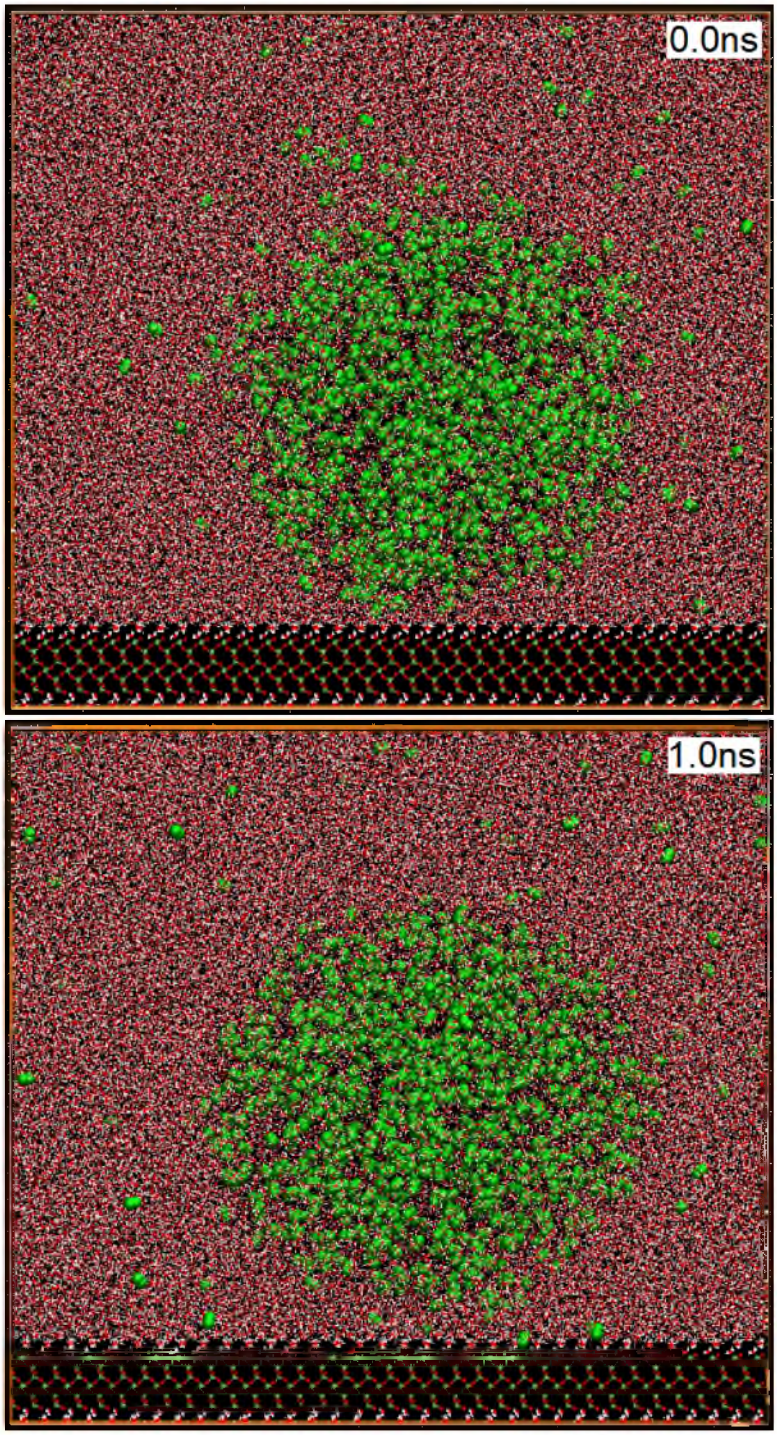

Figure 7.1. Snapshots of initial and final status of nitrogen bubble at quartz (001) surface. The atoms' color codes are as follow: green, N; lime, Si; red, O; white, H. Sphere Scale: quartz, 0.8 Å; nitrogen, 2.5 Å; water, lines.

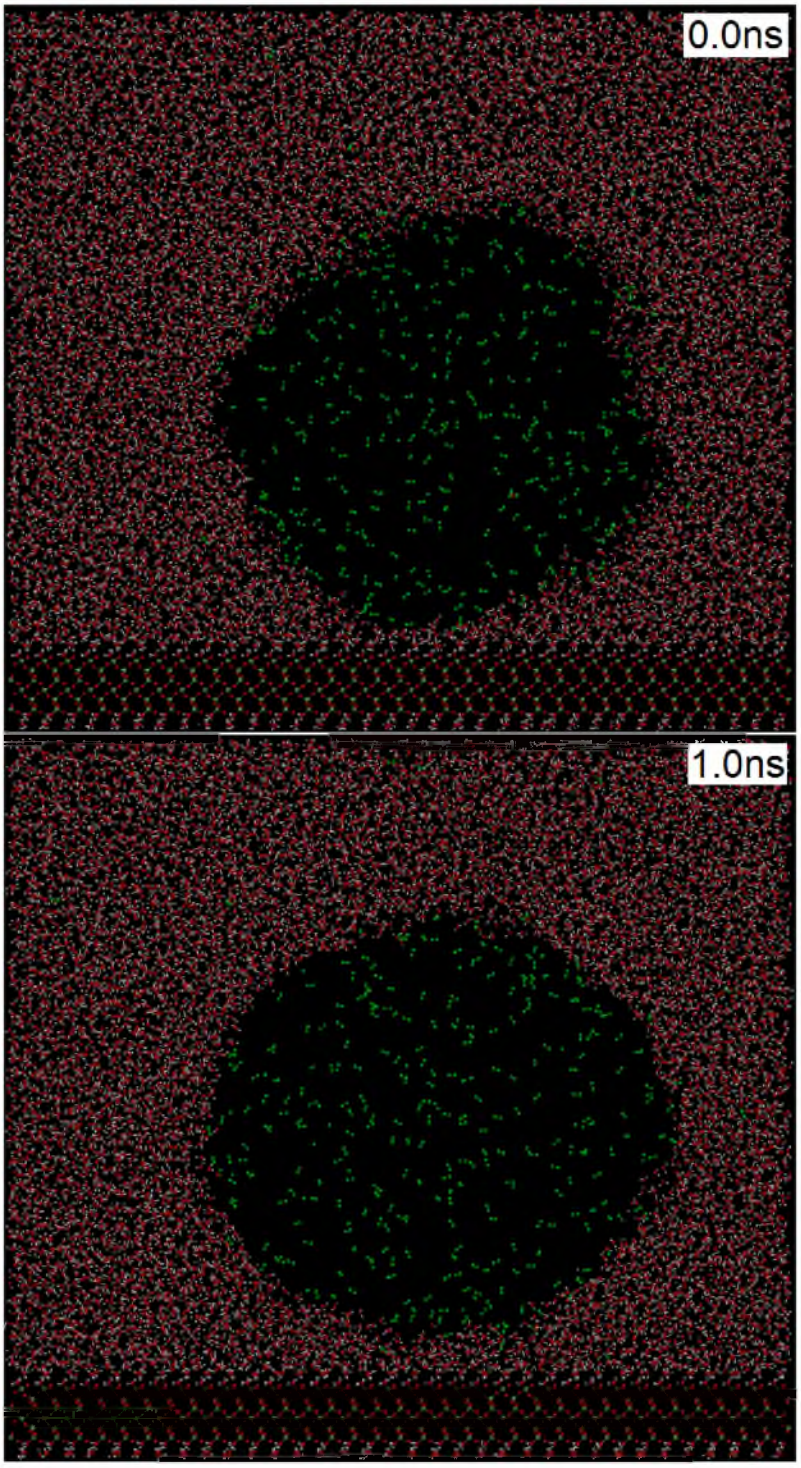

Figure 7.2. Thin sections of initial and final status of nitrogen bubble at quartz (001) surface. The atoms' color codes are as follow: green, N; lime, Si; red, O; white, H. Sphere Scale: quartz, 0.8 Å; nitrogen, 0.8 Å; water, 0.8 Å.

According to the thin sections, nitrogen molecules are dispersed in the gas bubble at a density of 28 g/L, significantly higher than the nitrogen gas density at standard temperature and pressure (1.25 g/L) but still much less than the density of liquid nitrogen at its boiling point (808 g/L).

The Young-Laplace equation for a nitrogen bubble in water is shown in equation (7.1), where Δp, γ, and R are the pressure difference across the nitrogen/water interface, the surface tension for water (72.8 dyne/cm at 298 K), and the radius of the bubble, respectively.

$$\Delta p = \frac{2\gamma}{R} \tag{7.1}$$

According to the Young-Laplace equation, pressure must increase as the bubble size decreases. For the nitrogen bubble with diameter of 7 nm (R = 3.5 nm) at 298 K, the pressure inside of the bubble is 41.6×10^7 dyne/cm^2. A previous study has confirmed this relationship (Takahashi et al., 1979).

At high pressure, the ideal gas law is not valid, so the corrected real gas law at high pressure is applied for the nitrogen bubble, as shown in equation (7.2).

$$p(V - nb) = nRT \tag{7.2}$$

where V, p, and n are the volume, pressure, and moles of nitrogen. For nitrogen gas, the constant b is 0.04 L/mol. T equals to 298 K, and R is the molar gas constant (8.314 J·K^{-1}·mol^{-1}). Calculation of the number of molecules in the nitrogen bubble with diameter of 7 nm is 1086, which is close to the number of nitrogen molecules (906) in the MD simulation.

Due to the lack of hydrogen bonding donors at the nitrogen/water interface, the interfacial water molecules form fewer hydrogen bonds than other water molecules in the

bulk solution (Somasundaram et al., 1999), resulting in higher entropy at the nitrogen/water interface. Because of the comparably strong hydrogen bonding interactions between water molecules in the aqueous phase, water molecules around the nitrogen bubble give pressure toward the center of the bubble to reduce its surface area. In the bulk water, because the pressures the nitrogen bubble received from all directions are equal, the bubble forms a spherical shape, which is proved by the MD simulation. According to the thin sections in Figure 7.2, the MDS interfacial water analysis of the quartz (001) surface reported in Chapter 4, as well as a previous SFG study of the interfacial water structure at a quartz surface (Wang et al., 2009), interfacial water molecules at the quartz (001) surface are very ordered and form hydrogen bonds with surface oxygen atoms at the quartz (001) surface. On the other hand, nitrogen molecules only have VdW interactions with the quartz (001) surface, which energy is much less than that of hydrogen bonding. As a result, the interfacial water molecules form a stable water film covering the quartz (001) surface. Rupture and displacement of the film does not occur at the quartz (001) surface. The thickness of the water film at the quartz (001) surface will be compared with experimental results and discussed in section 7.2. Due to this stable water film at the quartz (001) surface, the nitrogen gas bubble receives a pressure from the direction of the quartz (001) surface which is as strong as the pressures from other directions. Thus, film rupture and displacement of water molecules at the quartz (001) surface does not occur.

7.1.2 Molybdenite (001) Surface

MDS snapshots of the initial (0.0 ns) and final (1.0 ns) states of the nitrogen gas bubble at the molybdenite (001) surface are shown in Figure 7.3. The atoms in the molybdenite crystal are represented by spheres with diameter of 0.8 Å. The nitrogen and water molecules are represented by relatively large spheres with diameter of 2.5 Å and lines respectively. Initially, there was a water film about 1 nm thick between the nitrogen bubble and the molybdenite (001) surface, but the water film ruptured and the nitrogen bubble attached to the molybdenite (001) surface to form a hemisphere. Thin sections of the initial (0.0 ns) and final (1.0 ns) states of the nitrogen bubble attached at the molybdenite (001) surface are shown Figure 7.4, in which the molybdenite, nitrogen, and water molecules are represented by spheres with equal size (0.8 Å). The thin sections are consistent with the snapshots. According to the discussions in Chapter 4, the "water exclusion zone" indicates the relatively weak interaction between the interfacial water molecules and solid surface. In Figure 7.4, a "water exclusion zone" about 3Å thick is present at the molybdenite (001) surface. Thus, the interactions of the interfacial water molecules and the nitrogen gas molecules at the molybdenite (001) surface are relatively weak. It is well known that attachment of an air bubble at a hydrophobic surface includes film thinning, film rupture, and film displacement (Somasundaran, 2006; Wilson et al., 2000). Experimental techniques, such as high speed video, can catch the process of bubble attachment at mineral surface (Drelich and Miller, 2012; Niecikowska et al., 2012). However, MDS results for the attachment of the nitrogen bubble at the molybdenite (001) surface provide molecular scale information to examine the phenomena reported by previous researchers.

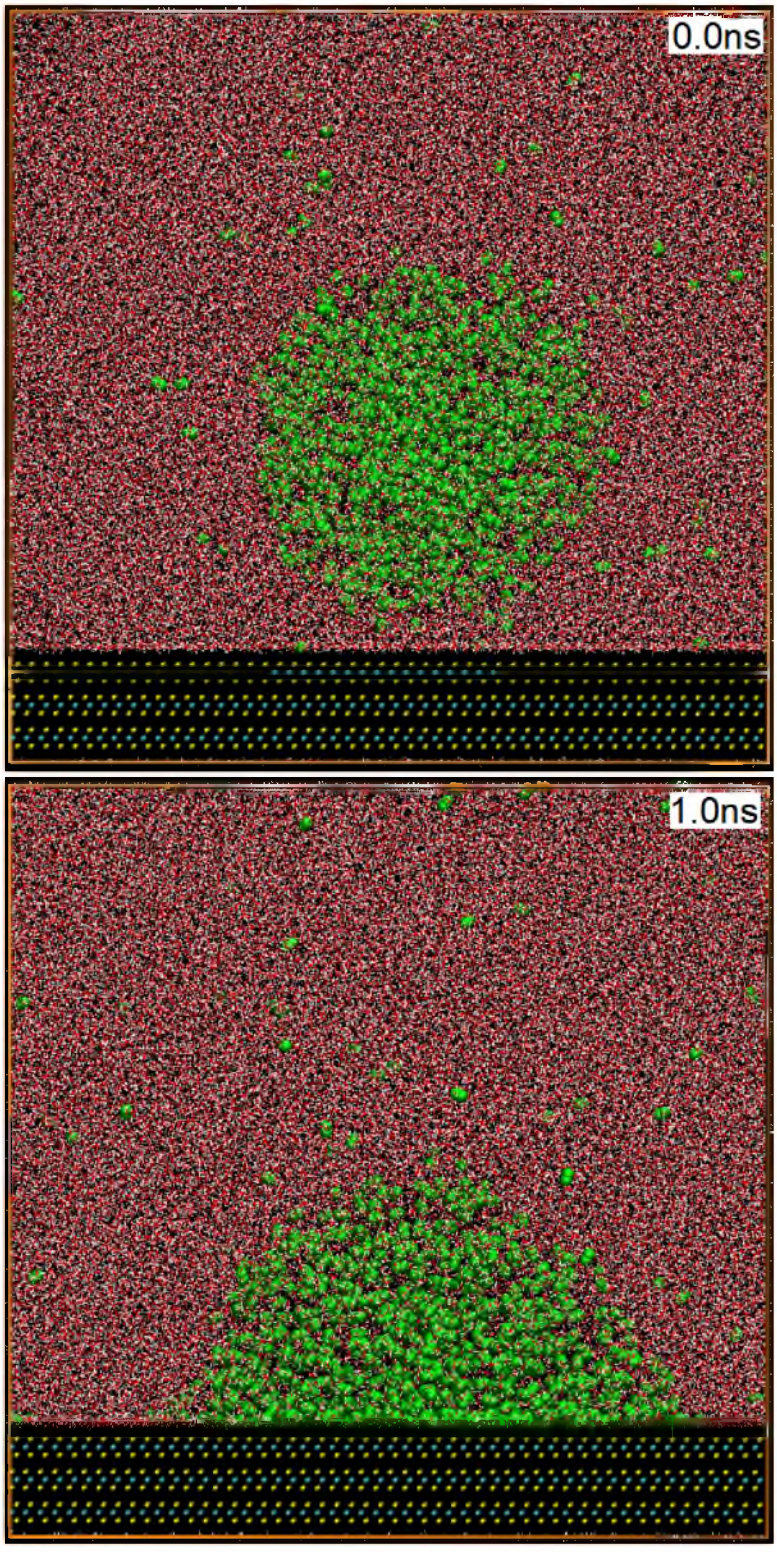

Figure 7.3. Snapshots of initial and final status of nitrogen bubble at molybdenite (001) surface. The atoms' color codes are as follow: green, N; cyan, Mo; yellow, S; red, O; white, H. Sphere Scale: molybdenite, 0.8 Å; nitrogen, 2.5 Å; water, lines.

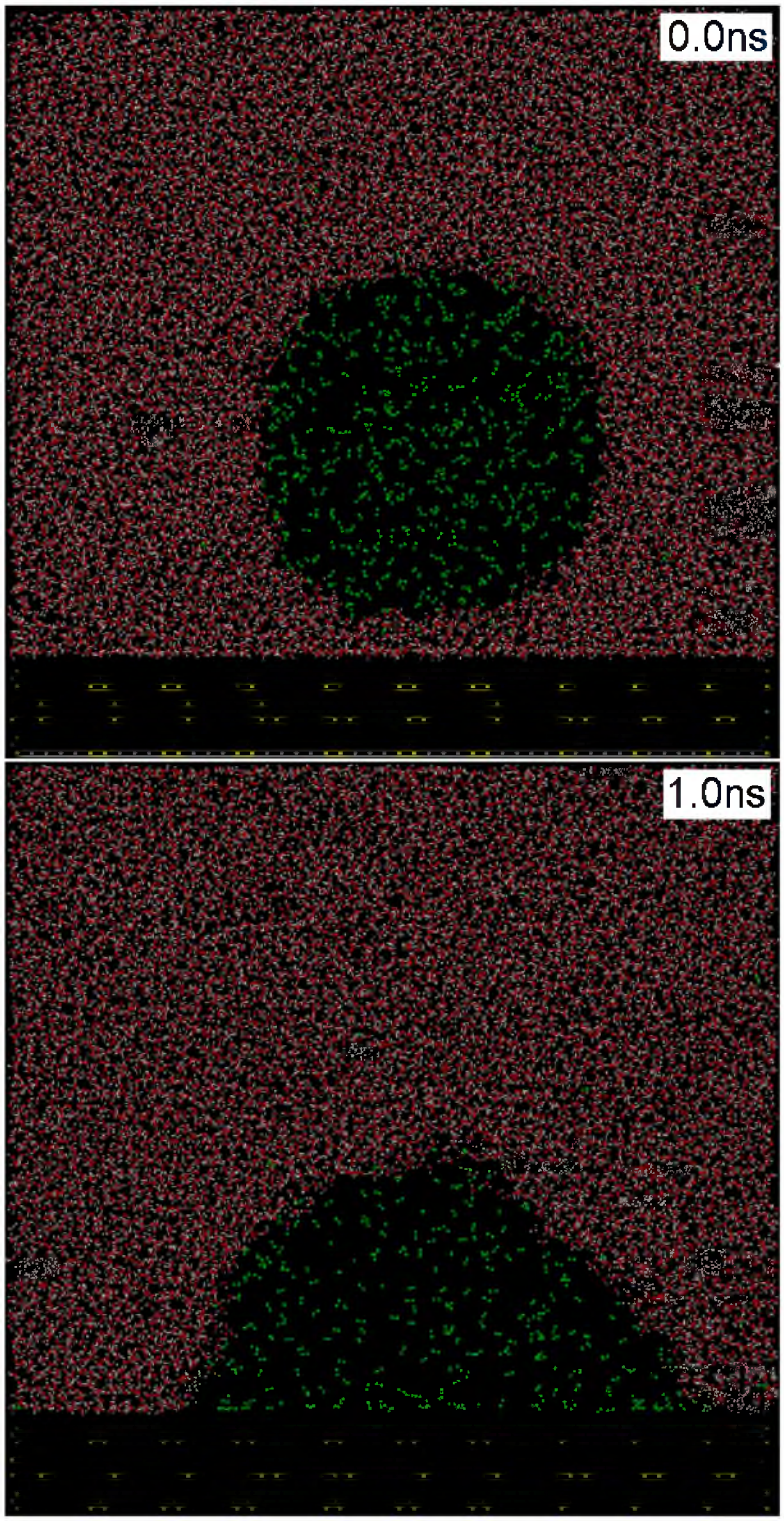

Figure 7.4. Thin sections of initial and final status of nitrogen bubble at molybdenite (001) surface. The atoms' color codes are as follow: green, N; cyan, Mo; yellow, S; red, O; white, H. Sphere Scale: molybdenite, 0.8 Å; nitrogen, 0.8 Å; water, 0.8 Å.

During attachment of the nitrogen bubble at the molybdenite (001) surface, the gas/solid interface is generated and stabilized. Table 7.1 lists the equivalent diameter of the attachment area (solid-gas interface) for different simulation times. The 0.7 nm equivalent diameter of attachment area at 0.1 ns simulation time indicates that a few nitrogen molecules have reached the molybdenite (001) surface, as a result of the film thinning process. The equivalent diameter of attachment area increased sharply from 0.7 nm to 4.0 nm during the simulation time from 0.1ns to 0.2ns, so film rupture and displacement occurred during this 100 ps simulation period. Then, the equivalent diameter of attachment area slowly increased to around 8 nm during film displacement in the following 800 ps simulation time.

Figure 7.5 shows the water film thinning and rupture process, in which nitrogen molecules start to reach the molybdenite (001) surface. Similar to the quartz/water interface, interfacial water molecules at the molybdenite (001) surface interact with each other to form hydrogen bonds. However, unlike the quartz (001) surface, at the molybdenite (001) surface there is no hydrogen bonding donor for interfacial water molecules. According to the MDS interfacial water hydrogen bonding analysis in Chapter 4 and 8, there are about 4.7 hydrogen bonds per water at the quartz (001) surface and 1.6 hydrogen bonds per water at the molybdenite (001) surface. The interaction between interfacial water molecules and the molybdenite (001) surface is relatively weak. As reported in Chapter 4 and 8, water residence time at the molybdenite (8.5 ps) is much less than at the quartz (001) surface (44.6 ps), so unlike the hydrophilic quartz surface, the water film at the molybdenite (001) surface is unstable. Thus, the nitrogen molecules are able to diffuse through the water film and reach the molybdenite (001) surface.

Table 7.1. Variation of Equivalent Diameter of Bubble Attachment Area with Time for the Simulation of Nitrogen Bubble Attachment at the Molybdenite (001) Surface

Simulation Time, ns	Equivalent Diameter of Attachment Area, nm
0.0	0.0
0.1	0.7
0.2	4.0
0.3	5.2
0.4	5.8
0.5	6.6
0.6	7.0
0.7	7.2
0.8	7.7
0.9	8.1
1.0	8.3

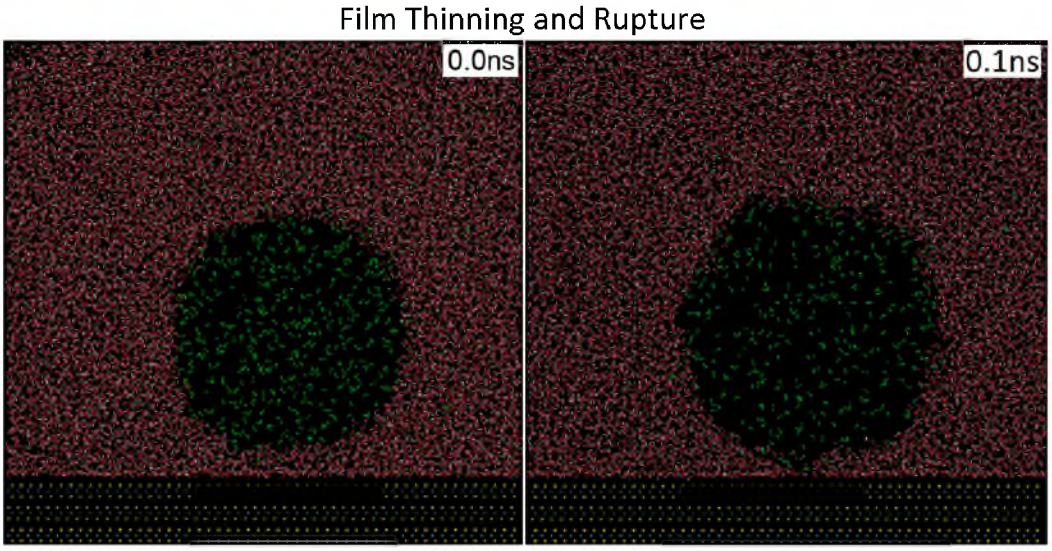

Figure 7.5. Thin sections of nitrogen bubble at molybdenite (001) surface for "film thinning and rupture" process. The atoms' color codes are as follow: green, N; cyan, Mo; yellow, S; red, O; white, H. Molecular Scale: molybdenite, 0.8 Å; nitrogen, 0.8 Å; water, 0.8 Å.

As listed in Table 7.1, the equivalent diameter of the attachment area is 0.7 nm at 0.1 ns, which corresponds to an attachment area of about 0.4 nm^2, so the film rupture started. Figure 7.6 shows the process of water film rupture and displacement, in which a bridge between the nitrogen bubble and molybdenite (001) surface is formed. The attachment area at 0.12 ns and 0.14 ns simulation time are 2.1 nm^2 and 7.7 nm^2, respectively. At this point, the film has ruptured, and the attachment area is expanding rapidly, due to film displacement. As a result, a nitrogen bridge has formed between the nitrogen bubble and molybdenite (001) surface.

Figure 7.7 shows further film displacement and the attached nitrogen bubble forms a hemisphere at the molybdenite (001) surface. More nitrogen molecules rush into the bridge formed as the film is displaced, and the attachment area keeps expanding. Finally (after 1 ns simulation time), the equilibrium state is achieved as indicated by the fact that a hemi-spherical shape of the bubble has been established.

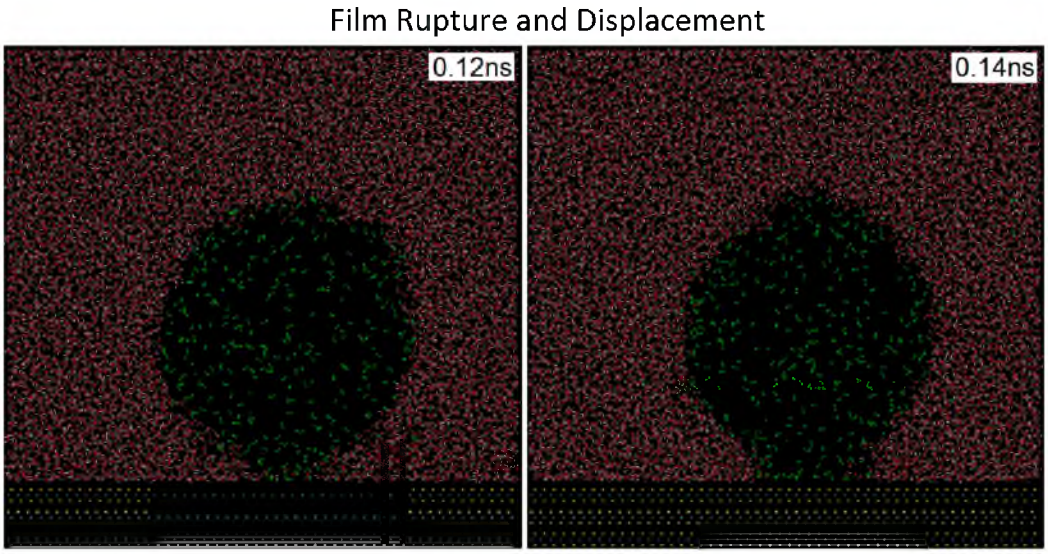

Figure 7.6. Thin sections of nitrogen bubble at molybdenite (001) surface for "film rupture and displacement" process. The atoms' color codes are as follow: green, N; cyan, Mo; yellow, S; red, O; white, H. Molecular Scale: molybdenite, 0.8 Å; nitrogen, 0.8 Å; water, 0.8 Å.

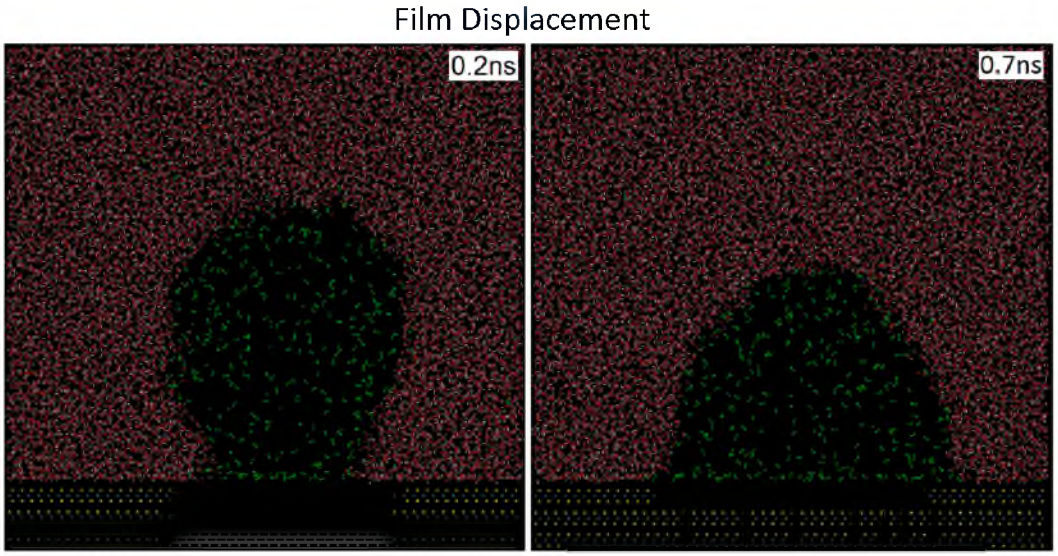

Figure 7.7. Thin sections of nitrogen bubble at molybdenite (001) surface for "film displacement" process. The atoms' color codes are as follow: green, N; cyan, Mo; yellow, S; red, O; white, H. Molecular Scale: molybdenite, 0.8 Å; nitrogen, 0.8 Å; water, 0.8 Å.

7.2 Contact Angles

The spherical shape of the established nitrogen bubble at the quartz (001) surface is verified by the 2-dimensional number density plot of nitrogen molecules in the x-z plane shown in Figure 7.8, based on a 100 ps simulation after the 1 ns simulation period. This is consistent with the experimental captive bubble measurements at the quartz surface, in which film rupture does not occur. Thus, both the MDS bubble attachment and experimental captive bubble contact angles at the quartz (001) surface are 0°. However, in the MD simulations there is no gravity, nor buoyant force, so the MDS bubble attachment contact angles are only influenced by the interatomic electrostatic and VdW interactions.

According to the 2-dimensional number density plot, the nitrogen gas/water interface is not very smooth, because of the diffusion of nitrogen gas and water molecules. The thickness of the water film at the quartz (001) surface is around 1 nm, which is much smaller than the experimental value 100 nm reported previously (Wang et al., 2014). The cut-off distance in this simulation is set at 1 nm, i.e., the interaction between two atoms over 1nm distance is not calculated. This cut-off distance is an empirical value validated for MDS studies of intermolecular interactions (Dang and Smith, 1995). In MD simulation, if two molecules are over 1 nm from each other after reaching equilibrium, the intermolecular interactions should be very weak. Thus, the MDS water film thickness at the quartz (001) surface indicates the very weak interaction between the nitrogen bubble and the quartz (001) surface.

The experimental captive bubble contact angle at the molybdenite (001) surface prepared by the procedures provided in section 2.2.3 is 75°, which is consistent with a previous study (Beaussart et al., 2012).

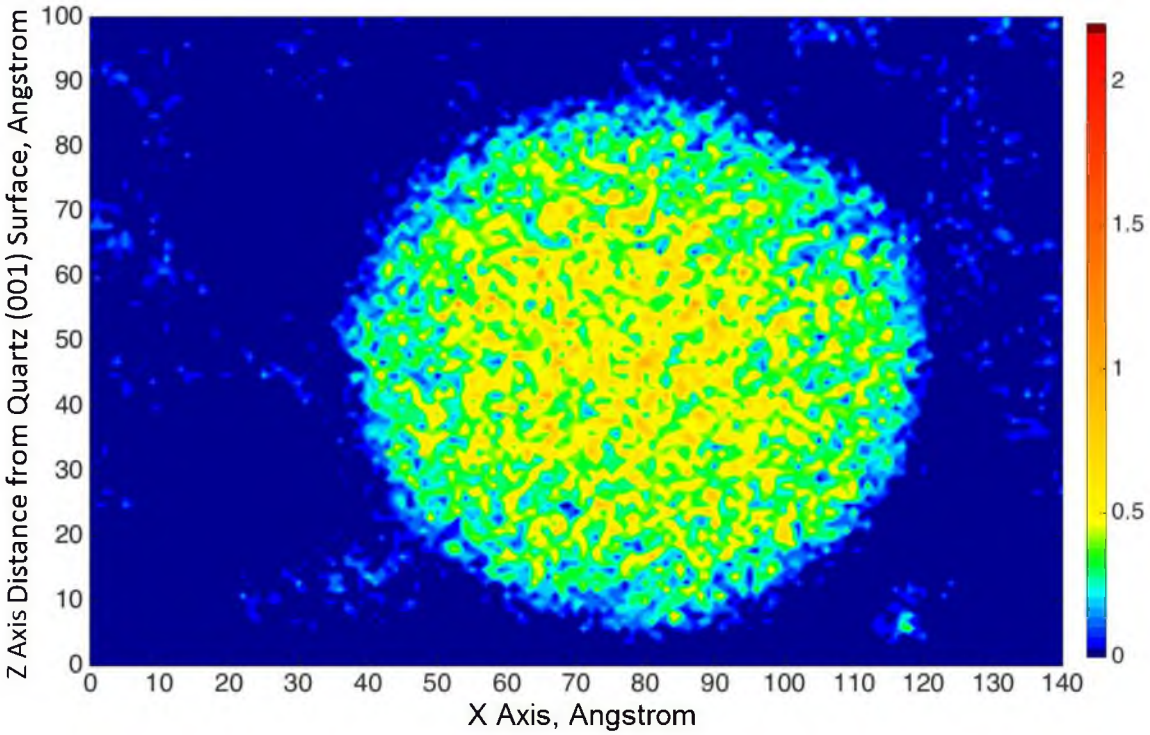

Figure 7.8. 2-dimentional number density distribution of nitrogen molecules at quartz (001)/water interface in the z-x plane. Color coded as number density of nitrogen per square average of projected area.

The 2-dimensional number density plot of nitrogen molecules for the nitrogen bubble at the molybdenite (001) surface in the z-x plane is shown in Figure 7.9. Using a method similar for MDS sessile drop contact angle measurements, in which the contact angles measured at a distance of 8 Å from the solid surface in the z-x plane and the z-y plane were then averaged, the MDS bubble attachment contact angle for the molybdenite (001) surface is 110°. This is larger than the experimental result.

However, according to the height (about 45Å) and width (about 95Å) of the nitrogen bubble in the 2-dimensional density plot, the shape of the nitrogen bubble attached to the molybdenite (001) surface is close to a hemisphere. By drawing a circle at the edge of the nitrogen bubble and a tangential line at the three-phase line of contact, a contact angle of about 90° can be measured.

Drawing the tangential line at a distance of 8 Å from the solid surface and at the three-phase line of contact give different MDS bubble attachment contact angles of the molybdenite (001) surface, but both results indicate the hydrophobic surface state of the molybdenite (001) surface. The two point model for nitrogen molecules used in this simulation may need further improvement to simulate the nitrogen bubble attachment by MDS. A three point model for nitrogen molecules will be used in future MDS bubble attachment studies (Somasundaram et al., 1999).

7.3 Summary

According to the film stability and bubble attachment MD simulations, film rupture did not occur at the selected hydrophilic surface, quartz, while the bubble attached to the selected hydrophobic mineral surface, molybdenite, and a contact angle was established.

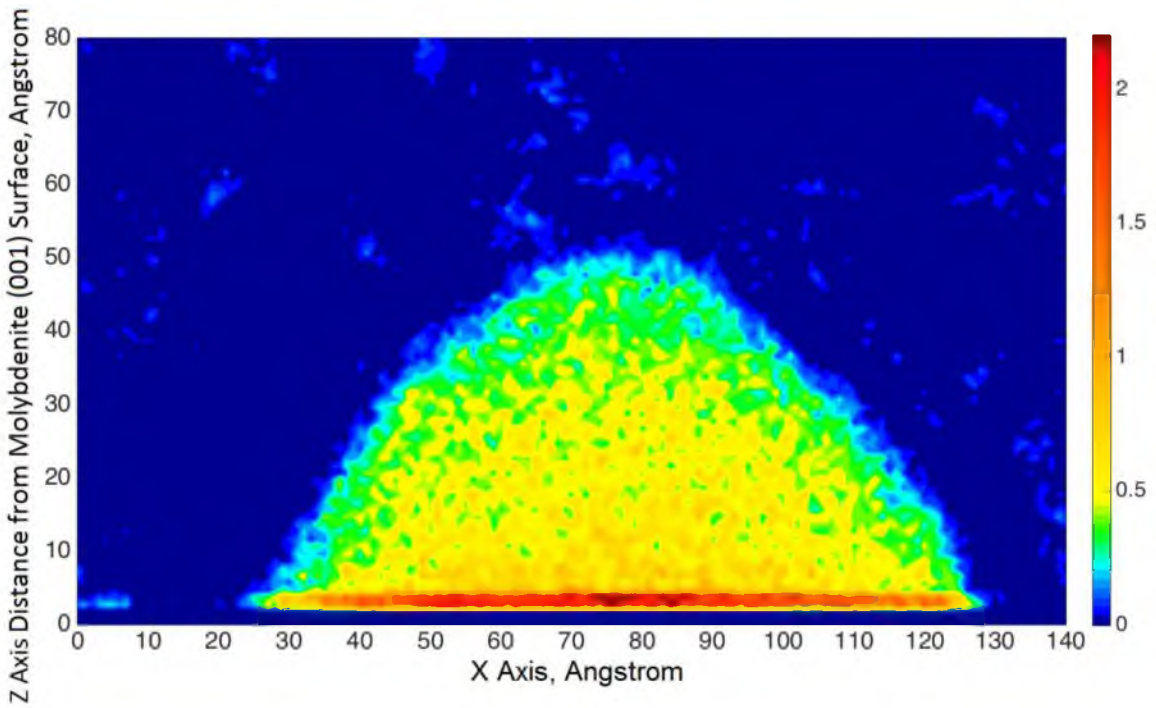

Figure 7.9. 2-dimentional number density distribution of nitrogen molecules at molybdenite (001)/water interface in the z-x plane. Color coded as number density of nitrogen per square average of projected area.

The film thinning, film rupture, and film displacement processes during bubble attachment at the molybdenite surface have been explored with MDS. The relatively weak interaction between the interfacial water molecules and the surface is the origin of bubble attachment. The MDS contact angles at the molybdenite surface and at the quartz surface are consistent with experimental results.

In future research, perhaps there is an opportunity that surface tensions can be calculated from MD simulations (Dang and Chang, 1997). The MDS surface tensions would be compared with experimental values and used to validate the contact angles by Young's equation.

CHAPTER 8

SULFIDE/TELLURIDE SURFACES

8.1 Sulfide/Telluride Mineral Surfaces under Anaerobic Conditions

The MDS contact angles of selected sulfide/telluride mineral surfaces under anaerobic conditions are compared with experimental results. Then, MDS results of the interfacial water structures at the selected sulfide/telluride mineral surfaces are reported and discussed to explain the native hydrophobicity of sulfide/telluride minerals.

8.1.1 Comparison of MDS and Experimental Contact Angles

MDS and experimental contact angles of the selected sulfide/telluride mineral surfaces are listed in Table 8.1. The MDS contact angles were measured by sessile drop method. However, in order to control the anaerobic condition, the experimental contact angles of the pyrite (100), galena (100), and sphalerite (110) surfaces were measured by captive bubble approach in DI water blown with pure Nitrogen gas for 5 minutes to decrease the composition of dissolved Oxygen in water. Due to the lack of large crystal specimens, experimental contact angle of the calaverite (001) surface is a sessile drop contact angle. All the simulation values are for a specific sulfide/telluride mineral surface, but the experimental contact angles for chalcopyrite (Drelich and Miller, 2012) is just for a random surface of the sulfide mineral.

Table 8.1 Simulated Contact Angles and Experimental Values of Selected Sulfide and Telluride Mineral Surfaces.

Mineral Surface	MDS Contact Angles, degree	Experimental Contact Angles, degree
Molybdenite Face	83	84
Calaverite (001) Surface	81	80
Pyrite (100) Surface	77	64
Chalcopyrite (012) Surface	72	74 (Random Surface)
Galena (100) Surface	65	82
Sphalerite (110) Surface	48	44
Molybdenite Armchair-Edge	54	36
Molybdenite Zigzag-Edge	24	

As a matter of fact, the experimental contact angle values for pyrite (100) and galena (100) surfaces are very close to the contact angle value for a random surface reported in literature (Jańczuk et al., 1992; Raichur et al., 2000). The experimental contact angles of the molybdenite face and edge surfaces are from a previous study (Chander and Fuerstenau, 1972). It is not known whether the experimental contact angle for the molybdenite edge is for the armchair-edge or the zigzag-edge; there probably are contributions from each edge surface. Thus, the experimental and simulated contact angles for chalcopyrite and the two molybdenite edges are not expected to be exactly the same. However, the experimental and simulated contact angles should be similar (i.e., the

simulation provides a reasonable prediction of the experimental value).

For the molybdenite face, calaverite (001), pyrite (100), chalcopyrite (012), and sphalerite (110) surfaces, the MDS contact angles are consistent with the experimental values. The MDS contact angle of the galena (100) surface indicates a hydrophobic surface state, but it is relatively smaller than the experimental value. The force field for galena used in this dissertation research may need improvements to give better predictions of the experimental contact angle of the galena (100) surface.

Furthermore, for the molybdenite edge surfaces, it seems that the edge surface used in the experimental contact angle measurement might be a combination of the two different edges, because the experimental value is approximately the average of the two simulated contact angles for the molybdenite armchair-edge surface and zigzag-edge surface calculated from the modified force fields. Based on the simulated contact angle measurements, the molybdenite zigzag-edge surface is much more hydrophilic than the molybdenite armchair-edge surface. According to the crystal structure for the molybdenite armchair-edge surface, the Mo and S atoms at the top layer of the surface are exposed to the water phase as the three-atom arms (each arm contains one Mo atom and two S atoms). The top view for one of the three-atom arms is highlighted in a green box in the snapshot (k) of Figure 8.1. Based on the atomic partial charge for the Mo and S atoms for molybdenite in the force fields, each of the three-atom arms in the molybdenite armchair-edge surface is overall electrically neutral, so the armchair edges of the moly-sulfur layers are not charged as a whole. But for the molybdenite zigzag-edge surface, the top layer of the surface is composed of rows of either Mo or S atoms, depending on which kind of atoms the zigzag-edge of the moly-sulfur layer exposes to the water phase.

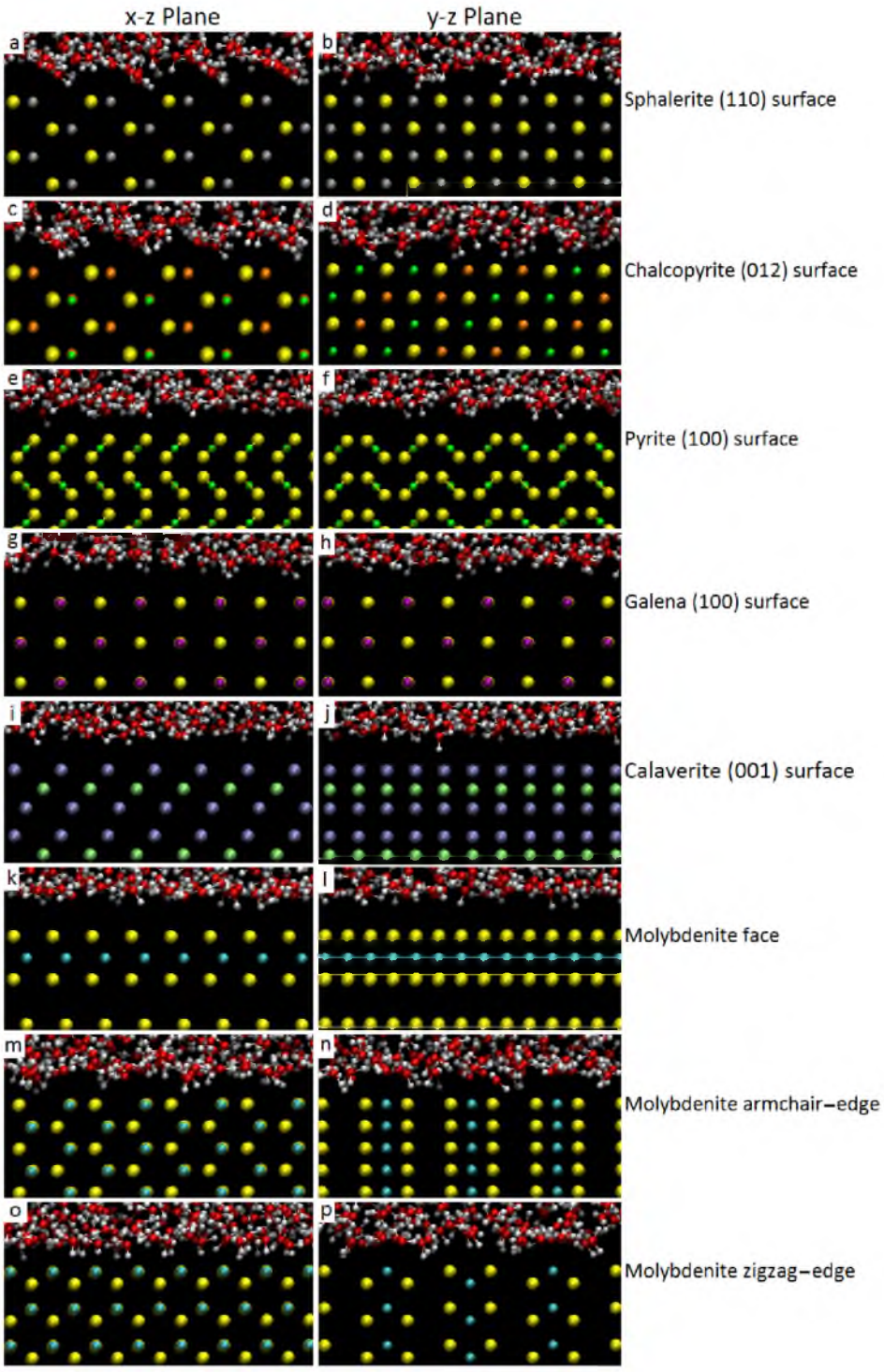

Figure 8.1. Snapshots of mineral/water interfaces: (a), (b), sphalerite (110) surface; (c), (d), chalcopyrite (012) surface; (e), (f), pyrite (100) surface; (g), (h), galena (100) surface; (i), (j), calaverite (001) surface; (k), (l), molybdenite face; (m), (n), molybdenite armchair-edge surface; (o), (p), molybdenite zigzag-edge surface. The simulation time is at 2 ns. The atoms' color codes are as follow: yellow, S; grey, Zn; orange, Cu; green, Fe; purple, Pb; lime, Au; iceblue, Te; cyan, Mo.

As shown in the snapshot (p) in Figure 8.1, if one of the zigzag-edges of the moly-sulfur layer exposes Mo atoms at the top, the two adjacent zigzag edges will expose S atoms at the top, and vice versa. The zigzag-edge with Mo atoms on the top becomes positively charged, and the zigzag-edge with S atoms on the top becomes negatively charged. Thus, the interfacial water molecules have much stronger electrostatic interaction with the molybdenite zigzag-edge surface. This could explain the relatively smaller contact angle for the molybdenite zigzag-edge surface than for the molybdenite armchair-edge surface. According to the simulated contact angles for each of the selected mineral surfaces, they can be divided into two groups: 1) a hydrophobic group composed of the molybdenite face, calaverite (001) surface, pyrite (100) surface, chalcopyrite (012) surface, and galena (100) surface, and 2) a less hydrophobic group, including the sphalerite (110) surface, molybdenite armchair-edge, and molybdenite zigzag-edge.

8.1.2 MDS Interfacial Water Structures

MDS snapshots in the x-z plane (left column) and in the y-z plane (right column) for the selected sulfide/telluride mineral-water interfaces are presented in Figure 8.1. Among all eight selected sulfide/telluride mineral surfaces, except the galena (100) surface, the crystal structures appear different in the two planes. According to the snapshots for the interfacial water molecules, water molecules at the sphalerite (110) surface, chalcopyrite (012) surface, and the two molybdenite edges display differences between the two planes, but water at the four other surfaces looks similar from both directions. Also, the water structures at the sphalerite (110) surface and chalcopyrite (012) surface are very similar, because of the similarity of the crystal structures for these two surfaces. Thus, the crystal

structure of selected sulfide mineral surfaces has a significant influence on their interfacial water structures.

Furthermore, the gap presented between the water phase and the sulfide mineral surfaces, reflecting the "water-excluded volume" (Abraham, 1978; Yu et al., 1999), is relatively larger for the molybdenite face, calaverite (001) surface, pyrite (100) surface, and galena (100) surface than for the other surfaces. This finding indicates that the interaction between the water molecules and these four mineral surfaces is weak, which is the origin of their macroscopic hydrophobic character.

In addition, it is obvious that the water-excluded volumes for the molybdenite armchair-edge and zigzag-edge surfaces are much smaller than for the molybdenite face surface, which indicates the relatively stronger interaction between the interfacial water and atoms of these two surfaces and their relatively weak hydrophobic character compared to the molybdenite face.

The relative number density is the fraction of the absolute number density over an average number density for the bulk water. Thus, for both oxygen and hydrogen atoms in the water phase, their relative number densities remain 1 over the distance of 8 Å away from the surface, where the surface atoms have little influence on the water density. The relative number density distribution functions for oxygen and hydrogen atoms in water molecules along the surface normal for selected sulfide mineral surfaces are plotted in Figures 8.2 and 8.3 for hydrophobic surfaces (molybdenite face, calaverite (001) surface, pyrite (100) surface, chalcopyrite (012) surface, and galena (100) surface) and less hydrophobic surfaces (sphalerite (110) surface, molybdenite armchair-edge, and molybdenite zigzag-edge).

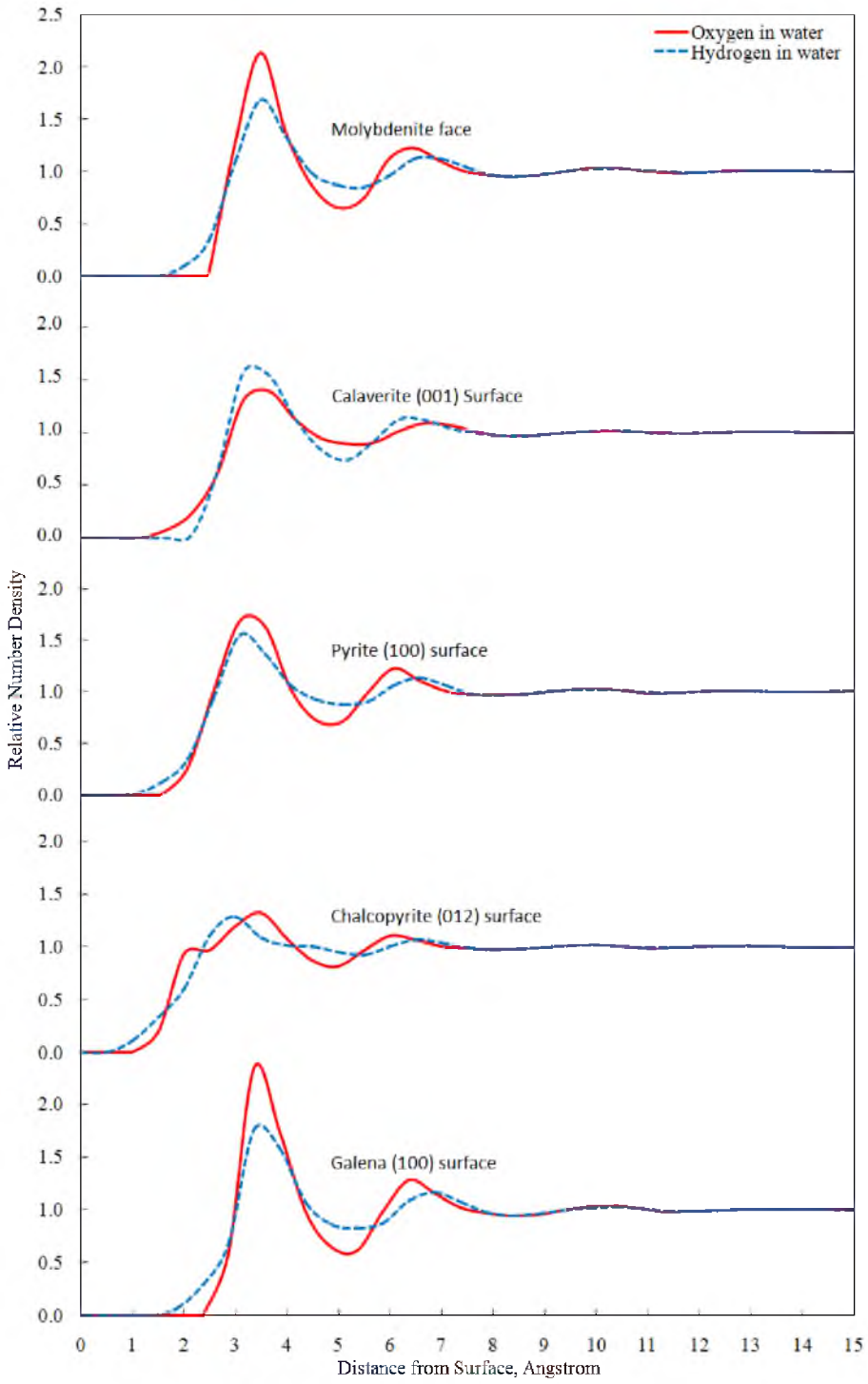

Figure 8.2. Relative number density profiles for hydrophobic sulfide/telluride mineral surfaces: molybdenite face; calaverite (001) surface; pyrite (100) surface; chalcopyrite (012) surface; galena (100) surface.

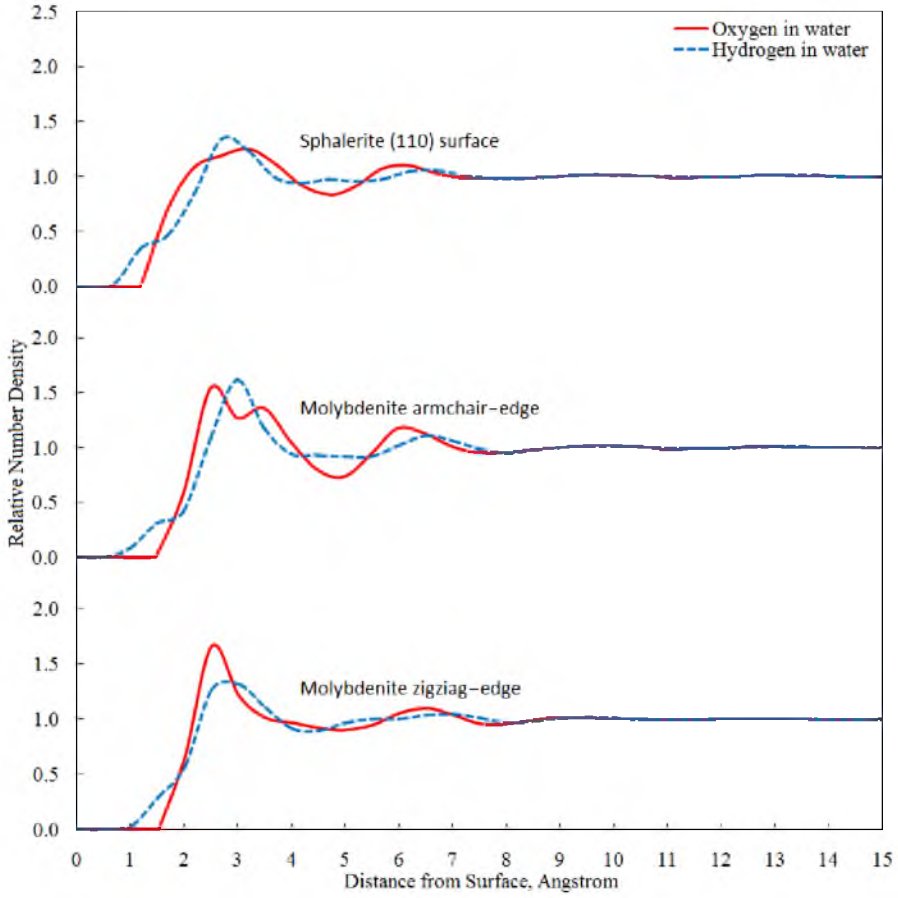

Figure 8.3. Relative number density profiles for relatively less hydrophobic sulfide mineral surfaces: sphalerite (110) surface; molybdenite armchair-edge surface;molybdenite zigzag-edge surface.

In a water molecule, the oxygen atom is only 0.065 Å away from the center of mass for water; therefore, the number density distribution of the oxygen atoms can represent the number density distribution of the center of mass for water molecules (i.e., the relative water number density distribution). The first peak of the relative water number density distribution for which the value is greater than 1 is considered as the "primary water density peak" for this surface, which means the water in this region is more condensed than in the bulk. As expected, due to the natural hydrophobicity of the molybdenite face, calaverite (001) surface, pyrite (100) surface, chalcopyrite (012)

surface, and galena (100) surface, water molecules are excluded from these surfaces. The primary water density peaks for these surfaces are located at least 3.2 Å away from the surface, and this distance is greater than the distance between hydrogen-bonded water/water molecules, which is approximately 2.8 Å (Dang and Pettitt, 1990; Lee and Rossky, 1994; Lynden-Bell and Rasaiah, 1997; Rasaiah and Zhu, 1990). This result demonstrates the weak interaction between the water molecules and these five sulfide mineral surfaces. On the other hand, water molecules interact more strongly with the metal and sulfur atoms at the sphalerite (110) surface, molybdenite armchair-edge surface, and molybdenite zigzag-edge surface. The distance between the surface and the primary water density peak for these three surfaces is between 2.2 Å and 2.5 Å, which is much smaller than the distance found for the five more hydrophobic surfaces. The distinct differences in the water-excluded volume for selected sulfide/telluride mineral surfaces, which are indicated by the primary water density peak, confirm the different interfacial water characteristics for hydrophobic and hydrophilic surfaces.

In addition, the relative number density distributions for hydrogen and oxygen atoms can provide excellent information for the water structures at selected sulfide mineral surfaces. As is shown in Figure 8.2, the hydrogen and oxygen relative number density distributions at the molybdenite face, calaverite (001) surface, pyrite (100) surface, and galena (100) surface appear to be very similar. At these four surfaces, the primary relative number density peak for hydrogen and oxygen atoms are located at almost the same position, which is between 3.2 Å and 3.5 Å away from the surface. This indicates that water molecules with oxygen and hydrogen atoms the same distance from the surface are the majority of the water molecules in the primary water density layer for these three

surfaces. However, it can be seen from the snapshots that the OH groups of some interfacial water molecules at the molybdenite face, calaverite (001) surface, pyrite (100) surface, and galena (100) surface are toward the mineral surface. Thus, water molecules in the primary water density layer should be vibrating or rotating along the water dipole moment with initial and final status as the water dipole moment and two hydrogen atoms parallel to the surface, resulting in the "free OH". This is the result of their relatively weak interaction with metal and sulfur atoms of these four surfaces.

By comparing the relative number density of oxygen and hydrogen atoms at the chalcopyrite (012) surface in Figure 8.2 and the sphalerite (110) surface in Figure 8.3, it can be found that they have similar interfacial water structures. In addition, both surfaces have two water peaks close to the surface, although the two water peaks for the sphalerite (110) surface are not as obvious as they are for the chalcopyrite (012) surface. Unlike the molybdenite face, calaverite (001) surface, pyrite (100) surface, and galena (100) surface, for which the surface atoms are organized in a relatively smooth and flat structure, the chalcopyrite (012) surface and sphalerite (110) surface have trenches with a depth of approximately 1.9 Å at their surfaces, as is shown in Figure 8.1. This kind of crystal structure will allow some of the water molecules above the trenches to move closer toward the surface, which accounts for the two water peaks at these two surfaces. The first water peak at the chalcopyrite (012) surface has a relative number density value that is less than 1, so it is not the primary water density peak, which means the water density in this region is less than that in the bulk water. For the sphalerite (110) surface, the first water peak in the region, which is only 2.2 Å from the surface and is more condensed than the bulk water, is the primary water density peak, so the interfacial water molecules

have relatively stronger interaction with the Zn and S atoms of the sphalerite (110) surface than with the Cu, Fe, and S atoms of the chalcopyrite (012) surface. Other evidence is the small but obvious hydrogen peak 1.2 Å away from the sphalerite (110) surface, which indicates that a large number of water molecules in the first water layer have their hydrogen atoms oriented toward the surface; this is not the case for the chalcopyrite (012) surface. In the force fields, although the Fe atom in chalcopyrite has a very similar atomic partial charge to the Zn atom, the value of the atomic partial charges for the Zn and S atoms in sphalerite is much larger than it is for the Cu and S atoms in chalcopyrite. If the surface atoms had larger atomic partial charges, they would have more intensive electrostatic interactions with the interfacial water molecules. Also, the Lennard-Jones parameters, r_m, for the Zn atom are the smallest among all the atoms, which means the Zn atom has the relatively weakest short-range repulsion and the interfacial water molecules can get closer to it than to other atoms. As a result, the sphalerite (110) surface has stronger interaction with the interfacial water molecules than the chalcopyrite (012) surface and a relatively weak hydrophobic character.

Both the molybdenite armchair-edge surface and the molybdenite zigzag-edge surface have a large and obvious primary water density peak 2.5 Å from their surfaces, indicating a stronger interaction between water molecules and surface atoms. In addition, the molybdenite armchair-edge surface has a second water density peak at the distance of 3.5 Å from the surface.

As shown by the snapshot of the molybdenite armchair-edge surface in Figure 8.1, the water molecules that are close to the S atoms exposed at the surface and on top of the crystal gaps between moly-sulfur layers get to move closer (about 2.5 Å) to the surface.

Also, some of these water molecules have their hydrogen atoms oriented toward the sulfur atoms in the surface, which explains the small hydrogen peak about 1.5 Å from the surface. However, the water molecules on top of the Mo atoms keep a distance approximately 3.5 Å from the surface. Thus, there are two water density peaks with different distances from the molybdenite armchair-edge surface.

From the snapshot for the molybdenite zigzag-edge surface shown in Figure 8.1, the water molecules on the top of the Mo atoms will have their oxygen atoms toward the Mo atoms, and the water molecules close to the S atoms will have their hydrogen atoms toward the S atoms. However, most of these interfacial water molecules have similar distances from the surface, so there is only one water density peak appearing in the relative number density profile for the molybdenite zigzag-edge surface. The interfacial water structures at the molybdenite armchair-edge surface and the molybdenite zigzag-edge surface will be further discussed with the results of water dipole orientation analysis.

The water dipole moment and hydrogen position relative density distributions for the molybdenite face, calaverite (001) surface, pyrite (100) surface, and galena (100) surface are shown in Figure 8.4. For these four surfaces, the majority of water molecules in the primary water density layer between 3.2 Å and 3.5 Å from the surface, which is mentioned in the relative number density section, have very similar water dipole orientations and hydrogen positions.

For these water molecules, the water dipole moment is perpendicular (90°) to the surface normal and in the plane parallel to the four selected sulfide/telluride mineral surfaces, which is revealed by the peak for the α angle at 90°.

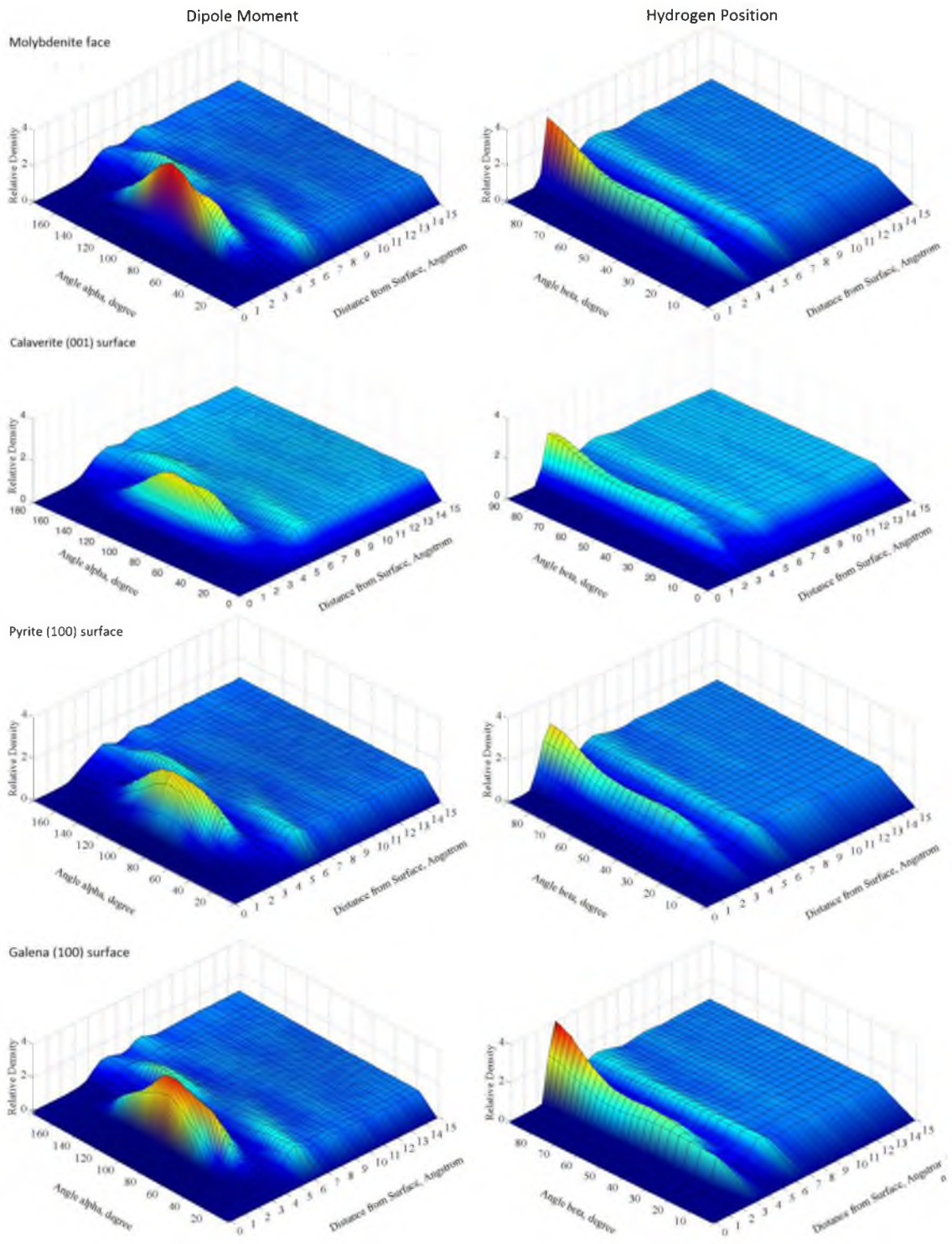

Figure 8.4. Water dipole moment (angle α) and hydrogen position (angle β) relative density distribution along the surface normal for selected sulfide mineral surfaces: molybdenite face; calaverite (001) surface; pyrite (100) surface; galena (100) surface.

The peak for the β angle at 90° and shoulder from 0° to 70° show that interfacial water molecules are vibrating or rotating along the dipole moment with the initial and final state of the line connecting the two hydrogen atoms in the plane parallel to the surface, which results in the "free OH" vibration at such hydrophobic interface. This is consistent with the number density profiles of the oxygen and hydrogen atoms in water. Thus, the interfacial water molecules at the molybdenite face, calaverite (001) surface, pyrite (100) surface, and galena (100) surface have relatively weak interaction with the metal, S, and Te atoms at the surface.

For the chalcopyrite (012) and the sphalerite (110) surfaces, the water dipole moments and hydrogen position relative density distributions shown in Figure 8.5 confirm the two water layers 2.2 Å and 3.3 Å from the surfaces, which are mentioned in the relative number density analysis.

According to the water dipole moment and hydrogen position relative density distributions, a large number of water molecules in the first water layer at the chalcopyrite (012) surface are parallel to the surface, because both the angle α and angle β have modest peaks around 90° in the region of the first water layer for the chalcopyrite (012) surface. However, for the sphalerite (110) surface, approximately 2 Å from the surface, a large relative density peak for the angle α at 90° and a modest relative density peak for the angle β at 50° indicate that the majority of water molecules in the first water layer have their water dipole moment perpendicular to the surface normal (i.e., parallel to the surface) and a large proportion of water molecules in this region have the two hydrogen atoms oriented about 50° to the surface normal (i.e., only one of the two hydrogen atoms in the water molecule is inclined toward the surface).

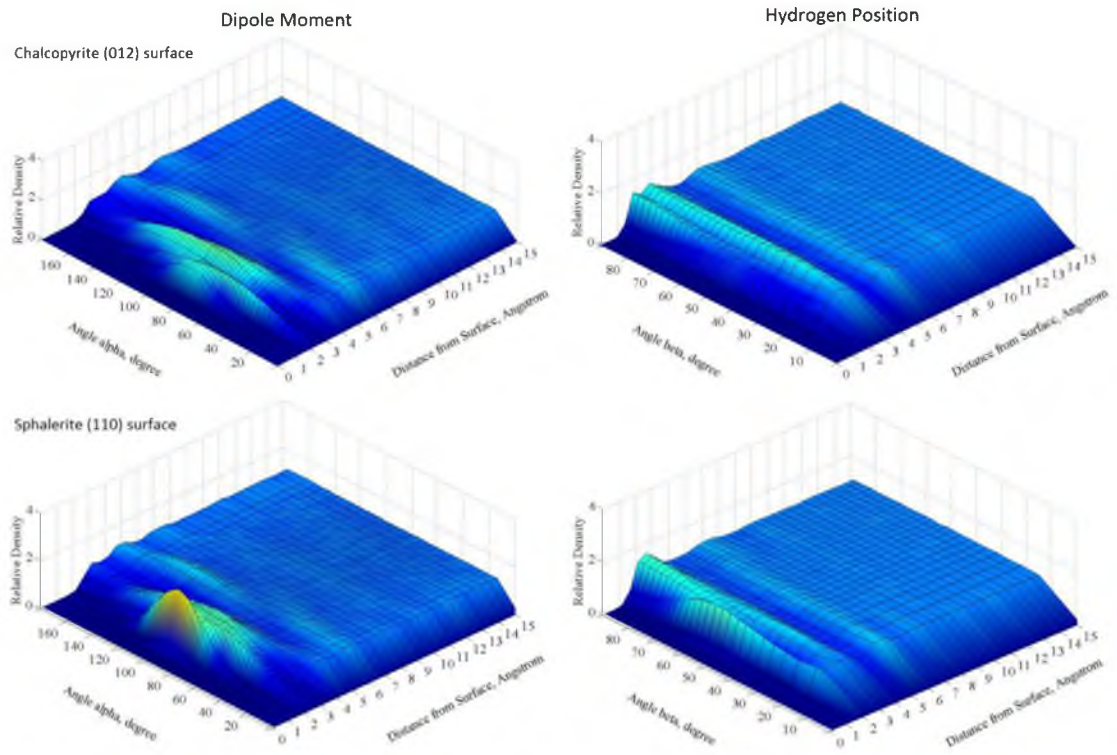

Figure 8.5. Water dipole moment (angle α) and hydrogen position (angle β) relative density distribution along the surface normal for selected sulfide mineral surfaces: chalcopyrite (012) surface; sphalerite (110) surface.

The large proportion of water molecules in the first water layer with one of the two hydrogen atoms inclined to the sphalerite (110) surface is responsible for the small but obvious hydrogen peak 1.2 Å from the sphalerite (110) surface. This orientation is revealed in the relative number density profile, which indicates the relatively stronger interaction between the interfacial water and surface atoms for the sphalerite (110) surface than for the chalcopyrite (012) surface. As discussed in the relative number density section, this is the result of the different force field parameters for the metal and S atoms of chalcopyrite and sphalerite in the force fields. The water molecules in the second water layer at the two surfaces have similar water dipole moments and hydrogen position relative density distributions, and a large number of them are vibrating along the

dipole moment which is perpendicular to the surface normal, so they have relatively weak interactions with the surface atoms. This also can help explain why the chalcopyrite (012) surface with its second water layer as the primary water density layer has a hydrophobic character.

From the water dipole moment and hydrogen position relative density distribution for the molybdenite zigzag-edge surface shown in Figure 8.6, two groups of water molecules with different types of dipole moment orientations and hydrogen positions are found in the region of the primary water density layer; see the two distinct peaks for both the angle α and β. The water molecule in the first group has the oxygen atom toward the surface and both hydrogen atoms toward the water phase, for which the α angle is 40° and the β angle is 90°.

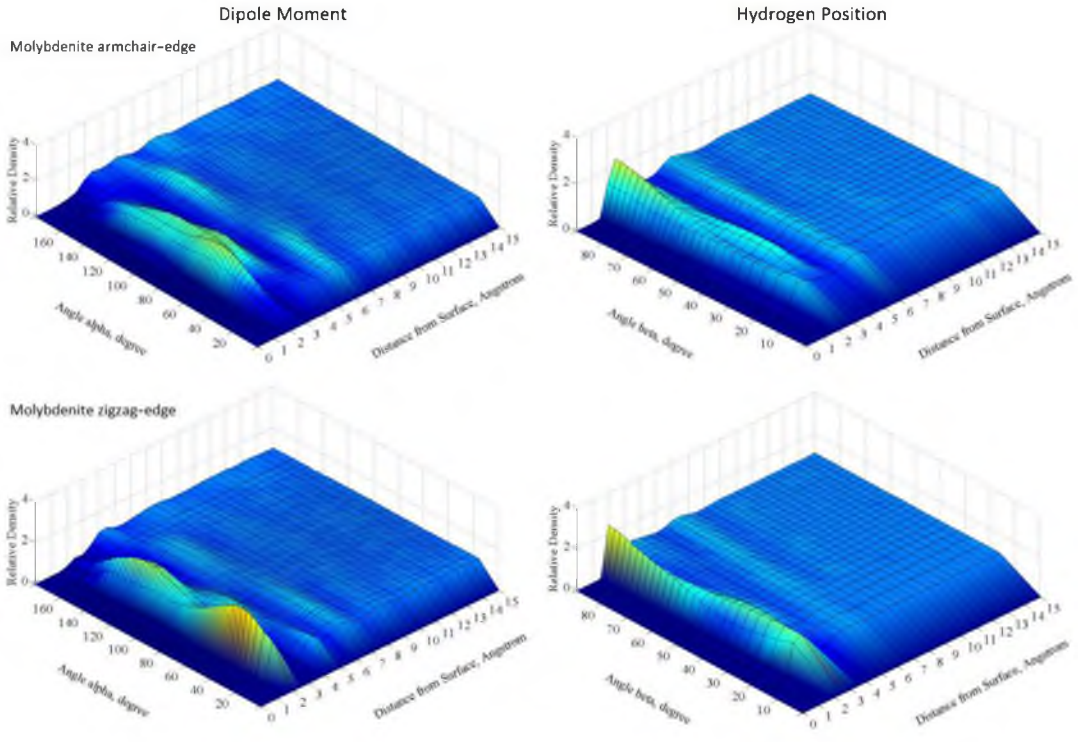

Figure 8.6. Water dipole moment (angle α) and hydrogen position (angle β) relative density distribution along the surface normal for selected sulfide mineral surfaces: molybdenite armchair-edge surface; molybdenite zigzag-edge surface.

The water molecule in the second group has the oxygen atom toward the water phase and one of the two hydrogen atoms toward the surface, for which the α angle is approximately 130° and the β angle ranges from approximately 10° to 40°. Because of the electrostatic interaction between the positively charged Mo atoms and the negatively charged oxygen atoms in water molecules, the first group of water molecules should be above the zigzag-edge of moly-sulfur layers where the top atoms are Mo. In the same way, the second group of water molecules should be on top of the zigzag- edge of moly-sulfur layers where the top atoms are S. This confirms the two groups of water molecules at the molybdenite zigzag-edge surface found from the snapshots. However, as shown in the water dipole moment and hydrogen position relative density distribution, the two groups of water molecules are only 0.5 Å from each other, which is the smallest distance that the analysis program can calculate. As a result, there is only one water density peak shown in the relative number density profile. Also, the water dipole moment and hydrogen position relative density distribution for the molybdenite armchair-edge surface is shown in Figure 8.6. Not much clear information can be extracted for the molybdenite armchair-edge surface from Figure 8.6. Compared to the molybdenite zigzag-edge surface, the relatively disordered water molecules at the molybdenite armchair-edge surface result from the relatively weak interaction between the interfacial water and surface atoms, which indicates a modest hydrophobic character.

The water residence time for selected sulfide mineral surfaces within 5 Å from the surface are listed in Table 8.2. The two peaks for the water residence time along the surface normal for the chalcopyrite (012), sphalerite (110), and molybdenite armchair-edge surfaces confirm the two water layers found at these three surfaces.

Table 8.2 Water Residence Time for Selected Sulfide/Telluride Mineral Surfaces within 5 Å from the Surface.

Mineral Surface	Water Residence Time			
	First Peak		Second Peak	
	Distance from Surface (Å)	Magnitude (ps)	Distance from Surface (Å)	Magnitude (ps)
Molybdenite Face	3.5	8.5		
Calaverite (001) Surface	3.6	6.7		
Pyrite (100) Surface	3.5	7.5		
Galena (100) Surface	3.6	9.3		
Chalcopyrite (012) Surface	2.5	7.4	3.6	5.5
Sphalerite (110) Surface	2.2	7.8	3.2	6.5
Molybdenite Armchair-Edge	3.0	9.0	4.0	5.0
Molybdenite Zigzag-Edge	3.0	10.5		

The molybdenite zigzag-edge surface has a water residence-time peak around the region of its primary water layer the magnitude of which is much larger (10.5 ps) than it is for other selected sulfide mineral surfaces. This reveals the relatively stronger interaction between the interfacial water molecules and surface atoms of the molybdenite zigzag-edge surface. This result is consistent with the weak hydrophobic character for the molybdenite zigzag-edge surface relative to all other selected sulfide mineral surfaces. Also, the smaller magnitude for the two water residence-time peaks at the chalcopyrite (012) surface compared to the two peaks at the sphalerite (110) surface confirms the hydrophobic character of the chalcopyrite (012) surface.

The magnitudes of the residence times for selected sulfide/telluride mineral surfaces are apparently much smaller than for these relatively hydrophilic nonsulfide mineral surfaces, such as the quartz (001) surface (44.6 ps), which indicates that the interfacial water molecules at all the selected sulfide/telluride mineral surfaces are not as tightly bonded with the surface when compared to these hydrophilic nonsulfide mineral surfaces. This is due to the different surface atoms between the selected sulfide/telluride mineral surfaces and the hydrophilic nonsulfide surfaces. The metal, S, and Te atoms at the selected sulfide/telluride mineral surfaces do not provide many hydrogen-bonding doners and accepters for the interfacial water molecules. Thus, they have relatively weak interaction with the interfacial water molecules, compared to the oxygen atoms from the oxide/silicate surfaces. This confirms the relatively hydrophobic character for the six selected sulfide/telluride minerals.

Distribution of the average number of hydrogen bonds per water molecule along the surface normal for selected sulfide/telluride mineral surfaces is shown in Figure 8.7.

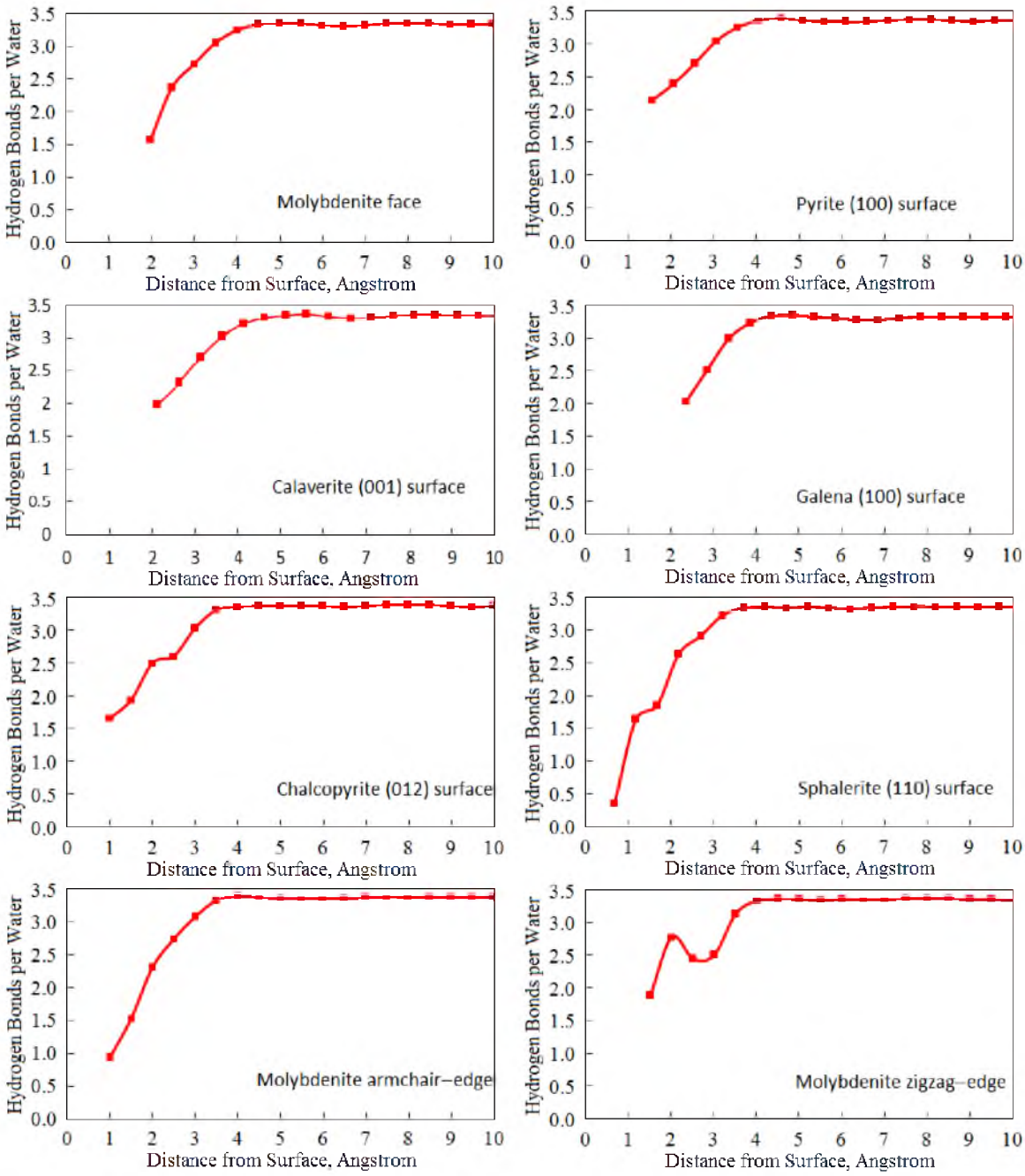

Figure 8.7. Distribution of hydrogen-bonding number per water molecule along the surface normal for selected sulfide mineral surfaces: molybdenite face; calaverite (001) surface; pyrite (100) surface; galena (100) surface; chalcopyrite (012) surface; sphalerite (110) surface; molybdenite armchair-edge surface; molybdenite zigzag-edge surface.

For all the selected sulfide/telluride mineral surfaces, from surface to the bulk water, the number of hydrogen bonds per water molecule increases until it reaches a plateau value around 3.35 about 4 Å from the surface, which is very close to the value of 3.5 reported in the literature (Nieto-Draghi et al., 2003). Although the number of hydrogen bonds per water molecule for the chalcopyrite (012) surface, sphalerite (110) surface, and molybdenite zigzag-edge surface fluctuate somewhat before they reach the plateau, none of them gets above the plateau value of 3.35 for bulk water. These fluctuations are mainly caused by two reasons. The first reason is the surface atomic roughness, such as the chalcopyrite (012) surface and sphalerite (110) surface which have trenches on the surface. These trenches significantly influence the number density distribution of interfacial water molecules, and thus influence the hydrogen bonding. The second reason is the particular interfacial water orientation, such as the sphalerite (110) surface and molybdenite zigzag-edge surface. For these two surfaces, a large number of interfacial water molecules is perpendicular to the surface, which has a relatively greater possibility of becoming hydrogen bonded with other water molecules.

On the other hand, the distribution of the number of hydrogen bonds per water molecule at the hydrophilic quartz surface has a large and distinct peak about 4.6 less than 1 Å from the surface, as is mentioned in section 4.2.2. These results suggest that most of the interfacial water molecules are tetrahedrally bonded at the hydrophilic quartz surface. Because of the exclusion of water molecules at the selected sulfide/telluride mineral surfaces, there are very few hydrogen bonds in the interfacial region over a distance of 1 Å from the surface. The distinct differences between the distributions of the number of hydrogen bonds per water molecule for the hydrophilic quartz surface and

selected sulfide mineral surfaces reveal the natural hydrophobic character for the selected sulfide/telluride mineral surfaces under anaerobic conditions.

8.1.3 Summary

The MDS for interfacial water molecules at the selected sulfide/telluride mineral surfaces under anaerobic conditions provide detailed information regarding interfacial water structures and dynamic properties. The simulation results reveal the natural hydrophobic character for the selected sulfide/telluride mineral surfaces in the absence of oxygen. The relatively strong hydrophobicity for the molybdenite face surface, pyrite (100) surface, calaverite (001) surface, chalcopyrite (012) surface, and galena (100) surface under anaerobic conditions was confirmed in the simulation. The weak interaction between the surface atoms of these surfaces and the interfacial water molecules are the primary reasons for this. On the other hand, the sphalerite (110) surface and two molybdenite edge surfaces were shown from the simulation results to have a modest hydrophobic character. For the sphalerite (110) surface, both the surface atomic structure and the larger partial charge for the Zn and S atoms in sphalerite cause a relatively strong interaction with interfacial water molecules. For the molybdenite armchair-edge surface and zigzag-edge surface, the exposed Mo and S atoms at the two edge surfaces also have relatively strong interaction with interfacial water molecules. Furthermore, because of the atomic surface structure of the molybdenite zigzag-edge, the surface becomes charged so that it interacts even more strongly with the interfacial water molecules and exhibits a weak hydrophobic character.

8.2 Oxidized Pyrite (100) Surface

The accommodation of a ferric hydroxide molecule at the pyrite (100) surface was studied by DFT simulations to describe the famous oxidation mechanism which involves formation of a metal deficient layer. Then, the crystal structures of polysulfide and elemental sulfur at the pyrite (100) surface were generated by DFT calculations.

In addition to experimental results, the following simulated surface states without/with the presence of ferric hydroxide were examined for a pyrite (100) surface using MD simulations:

- Fresh unoxidized (100) surface
- Polysulfide at the (100) surface
- Elemental sulfur at the (100) surface

8.2.1 DFT Study of Oxidized Pyrite (100) Surface Structures

The initial and final positions of the ferric cation and three hydroxide anions at the pyrite (100) surface, based on DFT quantum chemical calculations, are shown in Figure 8.8. During the whole geometry optimization process, the total energy of the system decreased from -2920937.5 kcal/mol to -2921125.7 kcal/mol. Both the Z coordinates for the Fe atoms in the pyrite (100) surface before and after the simulation are about 9.30Å. However, the Z coordinate for the ferric cation increased from 9.30Å to 11.27Å during the simulation, which means that the ferric cation was stabilized at a distance of almost 2Å from the pyrite crystal surface. This is consistent with the pyrite oxidation mechanism revealed in a previous XPS study (Buckley and Woods, 1987), in which iron hydroxide products and an underlying metal-deficient surface are formed.

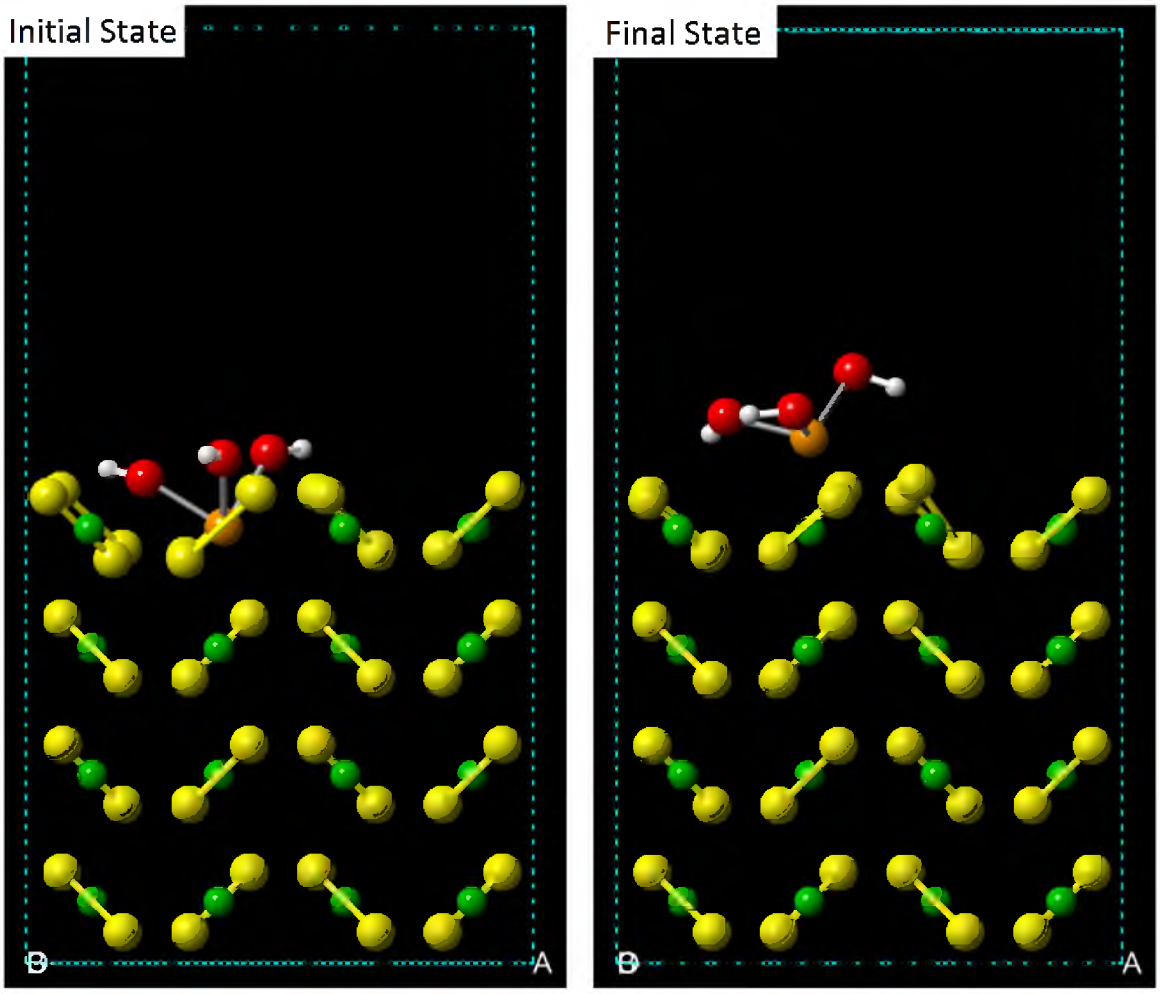

Figure 8.8. Snapshots for the initial state and final state of the DFT calculations for ferric hydroxide organized at the pyrite (100) surface. The atoms' color codes are as follow: yellow, S; green, Fe in pyrite crystal; orange, ferric cation; red, O; white, H.

The number of S atoms adjacent to the ferric cation before and after the simulation is also evidence for the well-known pyrite oxidation mechanism. The distance between an Fe atom and an adjacent S atom in pyrite is around 2.26Å. Before the simulation, there were five S atoms adjacent to the ferric cation (about 2.3Å). However, only two S atoms are adjacent to this ferric cation (2.49Å and 2.57Å) after the geometry optimization. These results suggest that there is not much interaction between the ferric cation and the pyrite (100) surface. The average distance between the ferric cation and the oxygen atoms

in hydroxide anions decreased from 1.966Å to 1.855Å during the simulation. The formation of $Fe(OH)_3$ in this way requires that the iron atom leave the pyrite (100) surface.

Pyrite oxidation is a complex process because of the structure of the oxidized pyrite surface and the environmental conditions, such as pH value of the aqueous phase. This DFT simulation is just a simple case to illustrate that the Fe atoms on the pyrite (100) surface will leave the surface once oxidized to ferric cations and form iron hydroxide with hydroxide anions, which is consistent with previous experimental studies. The surface state is important to create the crystal structure of the oxidized pyrite (100) surface, such as stabilization of polysulfide and/or elemental sulfur at the (100) surface, for our MDS study of interfacial water molecules.

The crystal structure of the polysulfide at the pyrite (100) surface generated from DFT quantum chemical calculations are shown in Figure 8.9 (a, b). The top view of the polysulfide (100) surface shows very good symmetry. There are four sulfur dimers around each Fe atom, and every two Fe atoms share one sulfur dimer. As a result, the electrical charge distribution on the polysulfide (100) surface is homogeneous.

Two elemental sulfur states at the (100) surface have been studied in this paper: the elemental sulfur dimers at the (100) surface, as shown in Figure 8.9 (c, d), and the elemental sulfur 8-member rings at the (100) surface, which are shown in Figure 8.9 (e, f).

The total energies of these two surfaces are almost the same (-2270090.3 kcal/mol vs. -2270089.7 kcal/mol). However, the simulated densities for elemental sulfur at these two surfaces are very different ($2.59 g/cm^3$ vs. $1.9 g/cm^3$).

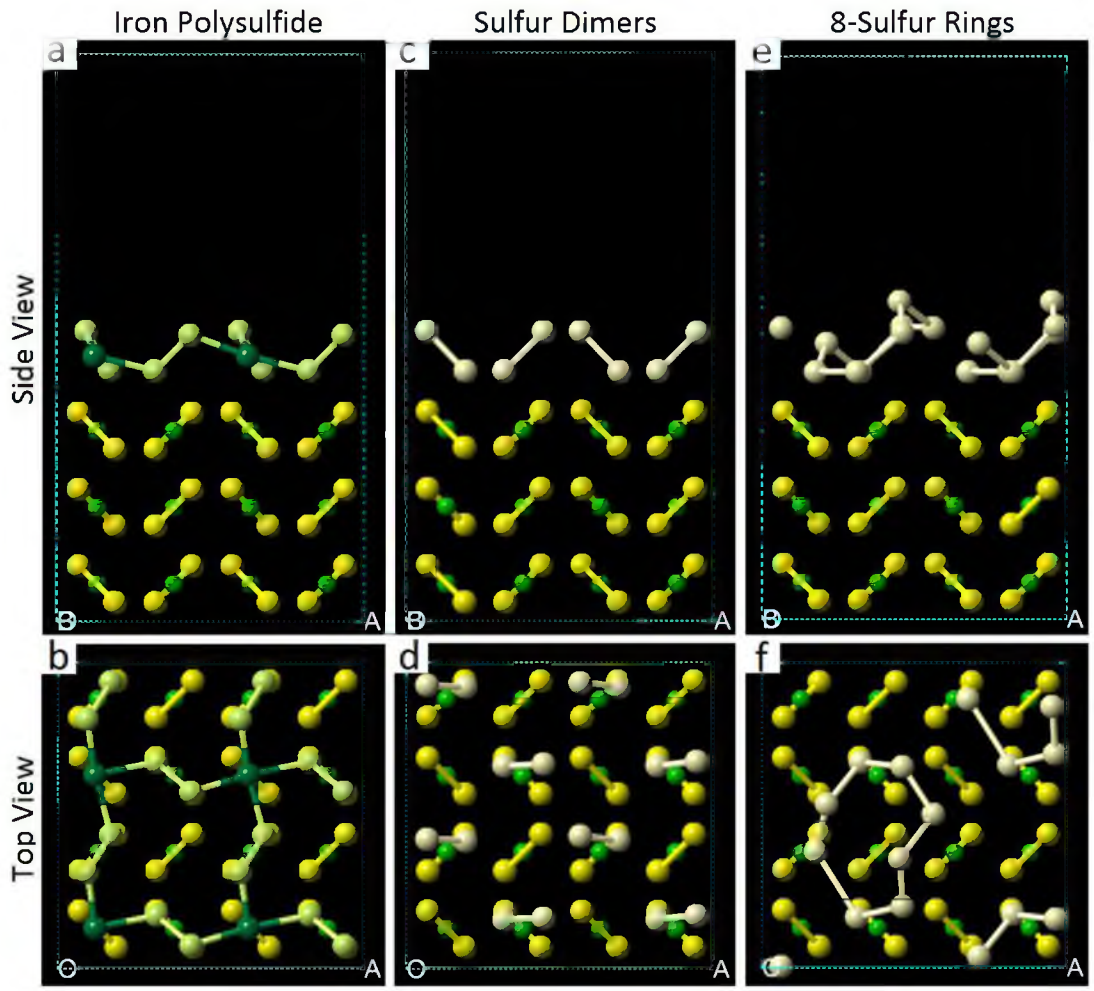

Figure 8.9. Top and side views of the polysulfide and two elemental sulfur states at the pyrite (100) surface. The atoms' color codes are as follow: yellow, S in pyrite crystal; green, Fe in pyrite crystal; dark green, Fe atoms in polysulfide; light green, S atoms in polysulfide; light yellow, elemental sulfur.

The simulated density for the elemental sulfur 8-member rings (100) surface is much closer to the literature values for elemental sulfur density at room temperature, which are all about 2 g/cm^3 (Steudel and Eckert, 2003). The wrong estimation of elemental sulfur density for the elemental sulfur dimers at the (100) surface could be a result from a local energy minimum during the DFT quantum chemical calculations. Both of these two elemental sulfur (100) surfaces have been studied using MDS for simulated contact angle measurements and interfacial water analysis.

8.2.2 Comparison of Experimental and MDS Contact Angles

The polished fresh pyrite (100) surface for experimental contact angle measurements is flat and smooth as established by the SEM image shown in Figure 8.10 (a).

In contrast, as shown in Figure 8.10 (b), after oxidation in the 30% hydrogen peroxide solution for 90 seconds, the pyrite (100) surface has a large number of very obvious light colored islands about 1 to 2 microns in diameter. Also, scratches on the oxidized pyrite (100) surface become more distinct. These bright spots are expected to be iron oxide/hydroxide. Since iron oxides (Fe2O3) are nearly insulators (Palacky, 1988), electrons would gather on the islands and make them brighter than the background pyrite crystal.

Figure 8.10 (c) shows the SEM image of the oxidized pyrite (100) surface washed with EDTA. As expected, after being washed with the saturated EDTA solution, the oxidized pyrite (100) surface became clean and smooth again when examined by SEM. The light iron oxide/hydroxide islands were dissolved and washed away by the saturated EDTA solution.

EDAX analysis found oxygen present at the pyrite (100) surface after 90 seconds oxidation in 30% hydrogen peroxide solution, which helps to confirm that the islands in the SEM image for the oxidized pyrite (100) surface are iron oxide/hydroxide. Unfortunately, the EDAX analysis is not able to show the composition change of the metal deficient layer at the oxidized pyrite (100) surface. The thickness of the metal deficient layer formed during the 90 seconds oxidation of pyrite in 30% hydrogen peroxide solution appears to be much smaller than the minimum depth SEM could distinguish.

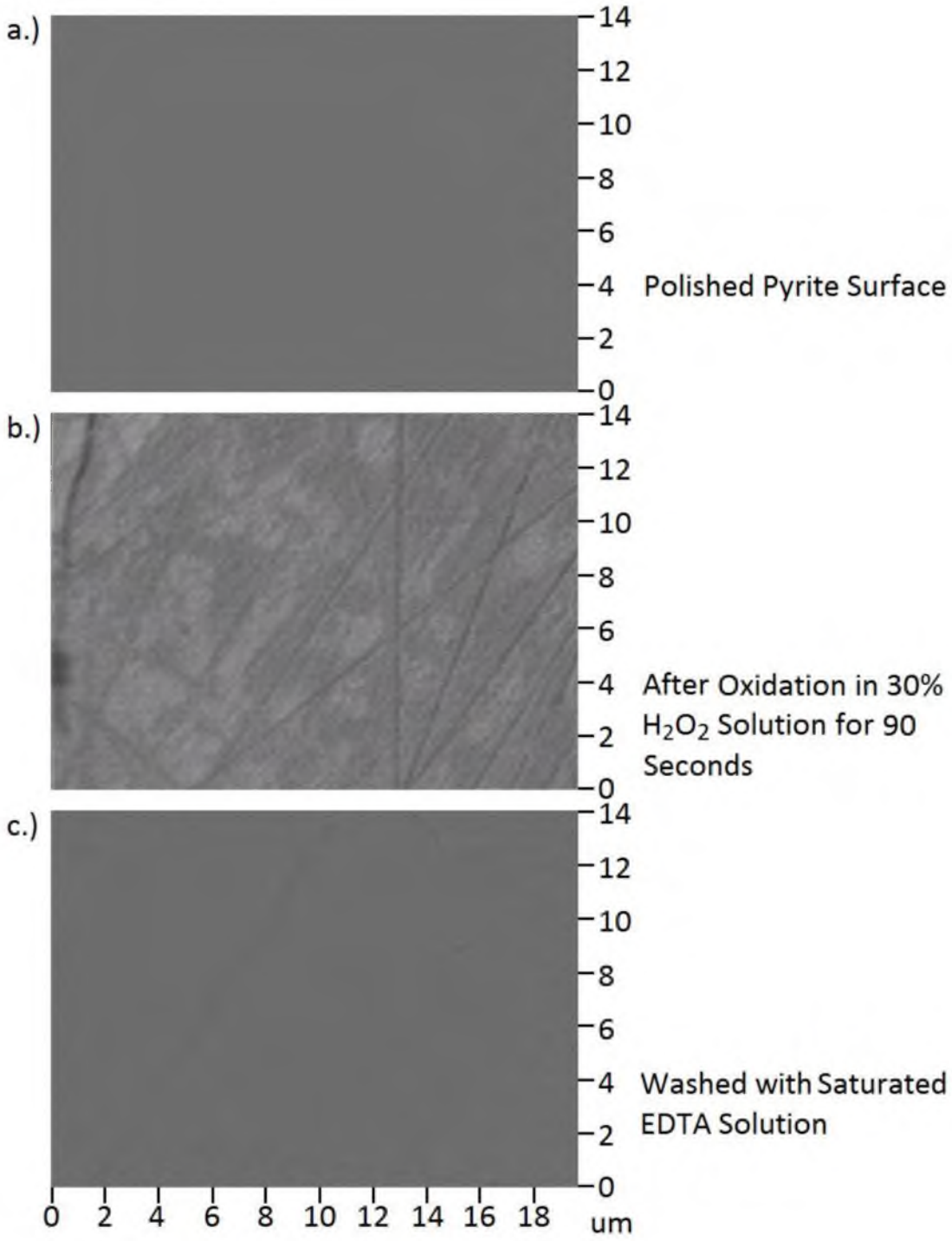

Figure 8.10. SEM images for: (a) the fresh pyrite (100) surface; (b) the pyrite (100) surface oxidized in 30% hydrogen peroxide solution for 90 seconds; (c) the oxidized pyrite (100) surface washed with EDTA.

More depth sensitive techniques, such as XPS, Scanning Tunneling Microscopy (STM) or Transmission Electron Microscopy (TEM), will be involved in future studies of pyrite oxidation. However, the results of both the SEM imaging and EDAX analysis are consistent with previous AFM studies on the oxidation of the pyrite surface (Du Plessis, 2004).

Experimental contact angles for the fresh and oxidized pyrite (100) surfaces measured by the captive bubble approach are listed in Table 8.3. The large contact angle for the polished fresh pyrite (100) surface (62.5°), which is consistent with that reported in the literature (Raichur et al., 2000), reveals the natural hydrophobic character and floatability for pyrite. However, after oxidation in 30% hydrogen peroxide solution for 90 seconds, the contact angle for the oxidized pyrite (100) surface decreased to 23 degrees, indicating that the surface has become more hydrophilic. This is again consistent with previous contact angle measurements on a random pyrite surface (Raichur et al., 2000).

As is discussed, after oxidation in 30% hydrogen peroxide solution for 90 seconds, part of the pyrite (100) surface is covered by an iron oxide/hydroxide surface deposit which is responsible for the hydrophilic character and wettability of the oxidized pyrite (100) surface.

How these iron hydroxide islands change the hydrophobic character of the pyrite (100) surface is discussed at the molecular level based on MDS. As the oxidation time increased to 180 seconds, the contact angle for the oxidized pyrite (100) surface decreased further. The coverage of iron oxide/hydroxide islands on the oxidized pyrite (100) surface is expected to increase as the oxidation time increases, making the oxidized pyrite (100) surface more hydrophilic.

Table 8.3 Experimental Contact Angles of Fresh and Oxidized Pyrite (100) Surfaces.

Pyrite (100) Surface	Contact Angle, Degree
After Polishing	62.5
Oxidized in 30% Hydrogen Peroxide Solution for 90 Seconds	23.0
Oxidized in 30% Hydrogen Peroxide Solution for 180 Seconds	12.0
Washed with EDTA Solution	64.5

The contact angle for the oxidized pyrite (100) surface washed with saturated EDTA solution is as large as the contact angle for the polished fresh pyrite (100) surface. As expected, when washed with the saturated EDTA solution, the oxidized pyrite (100) surface became hydrophobic again. After washing with EDTA solution, the iron oxide/hydroxide islands at the oxidized pyrite (100) surface were removed, so the surface becomes hydrophobic and is not well wetted by water. As a result, the collectorless flotation of oxidized pyrite can be obtained easily after complexing the iron with EDTA in solution (Smart et al., 2003).

Simulated contact angle measurements without and with ferric hydroxide were made for each case. The simulation results for the fresh unoxidized pyrite (100) surface without/with the presence of ferric hydroxide for the y-z plane are expressed as a best fit contour line, by way of example, in Figure 8.11. As is shown in Figure 8.11 (a), the water drop at the fresh unoxidized (100) surface without the presence of ferric hydroxide does not wet the surface and forms a hemispherical drop, indicating a hydrophobic surface.

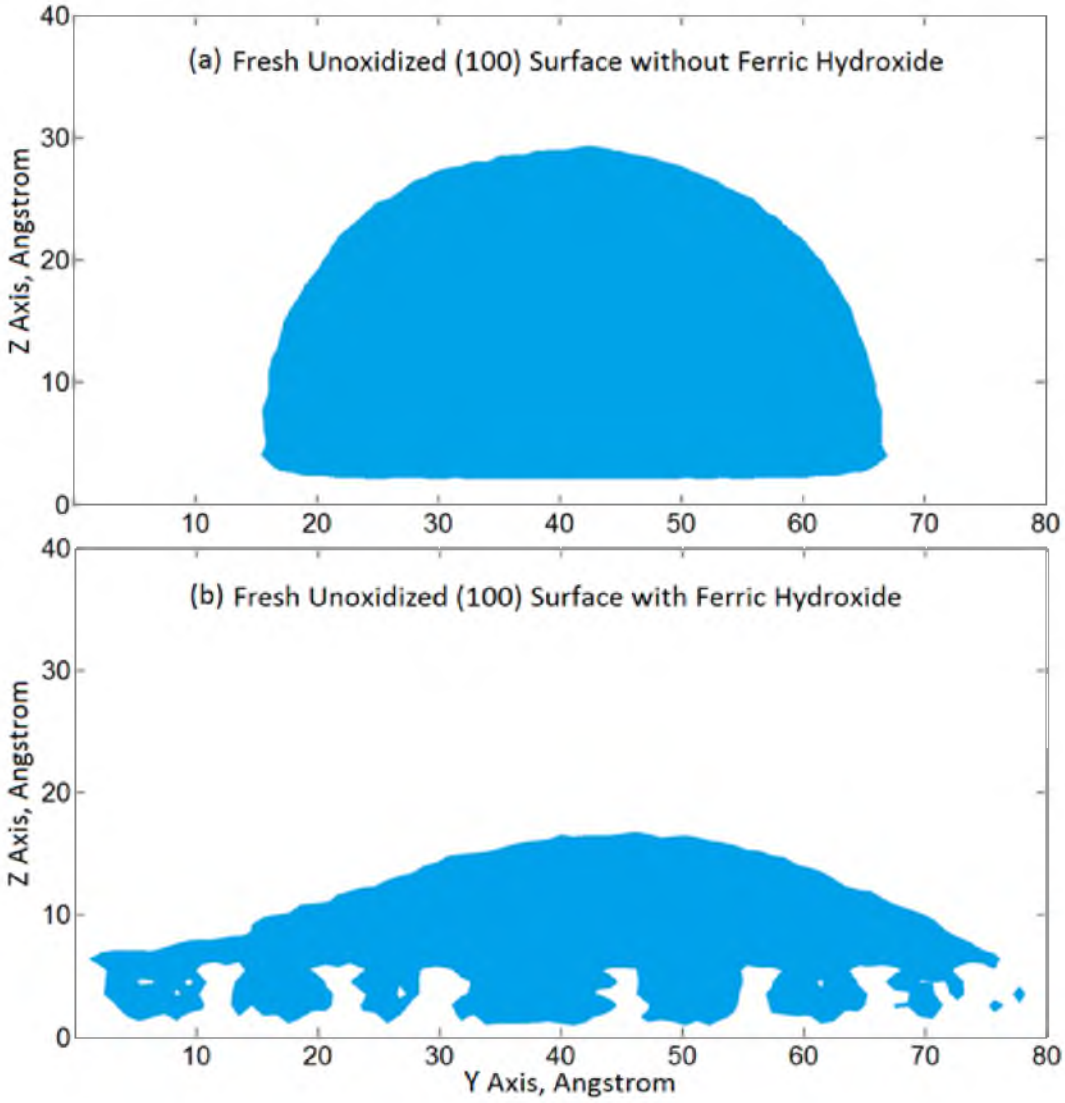

Figure 8.11. Water drop at a fresh unoxidized pyrite (100) surface: (a) without ferric hydroxide; (b) with ferric hydroxide.

However, for the fresh unoxidized (100) surface with the presence of ferric hydroxide shown in Figure 8.11 (b), the water drop spreads significantly on the surface, which reveals the relative hydrophilic character of the surface. A relatively small contact angle has been established at the fresh unoxidized (100) surface with the presence of ferric hydroxide. The spaces on the bottom of the water drop are the ferric hydroxide islands on the fresh unoxidized (100) surface; see Figure 8.12 (c, d).

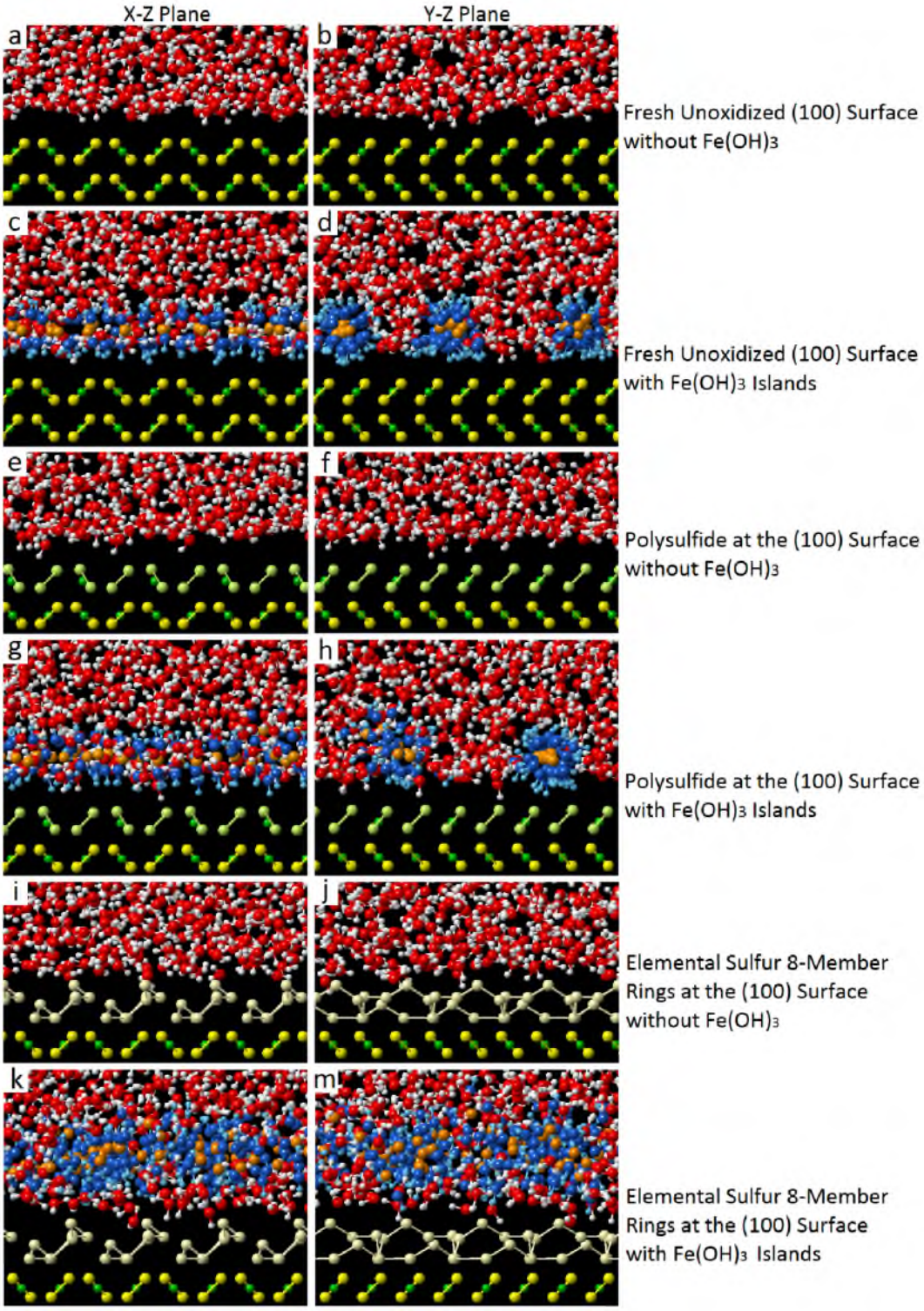

Figure 8.12. Snapshots for interfacial water at the pyrite (100) surface. The simulation time is at 2 ns. The atoms' color codes are as follow: red, O in water; white, H in water; blue, O in hydroxide; light blue, H in hydroxide; orange, ferric cation; yellow, S in pyrite; green, Fe in pyrite or polysulfide; light green, S atoms in polysulfide; light yellow, elemental sulfur.

As is shown in Figure 8.12 (g, h, k, and m) and as will be discussed later, interfacial water molecules for the polysulfide and elemental sulfur 8-member rings at the (100) surfaces with the presence of ferric hydroxide are influenced by the ferric hydroxide islands. Thus, the simulated contact angles should be measured at a distance from the fresh and oxidized pyrite (100) surfaces, in order to minimize the ferric hydroxide islands' influences on simulated contact angle measurement. In this dissertation research, the position of the fresh and oxidized pyrite (100) surfaces is defined by the top most atoms of the surface. The contact angle was measured by drawing a tangent line from the point at the foot of the contour line at a height of 10 Å away from the fresh and oxidized pyrite (100) surfaces also to avoid the influence from density fluctuations at the water/mineral interface (Werder et al., 2003) and the atomic roughness at the surface. In the same way, similar measurements were made for each case, and the results are presented in Table 8.4. As expected, the large simulated contact angle for the fresh unoxidized (100) surface without ferric hydroxide reveals the natural hydrophobiciy and floatability of pyrite, which is consistent with the experimental contact angle. However, once these ferric hydroxide islands are present on the fresh unoxidized (100) surface, the simulated contact angle decreased significantly, becoming more hydrophilic. The ferric hydroxide islands formed on the fresh unoxidized (100) surface make the surface wettable by water. This is important MDS evidence for the significance of the formation of ferric hydroxide islands and the corresponding hydrophilic surface state. Also, these results are consistent with the fact that after grinding, the pyrite surface becomes substantially covered by the hydrophilic iron hydroxide species and no significant flotation is observed without addition of collector (Smart et al., 2003).

Table 8.4 Simulated Contact Angles for the Fresh and Oxidized Pyrite (100) Surface.

Mineral Surface	Ferric Hydroxide	Contact Angle , Degree
Fresh Unoxidized (100) Surface	No	70.0
	Yes	24.0
Polysulfide at the (100) Surface	No	72.5
	Yes	22.0
Elemental Sulfur 8-Member Rings at the (100) Surface	No	71.0
	Yes	14.0
Elemental Sulfur Dimers at the (100) Surface	No	72.5
	Yes	14.0

The simulated contact angles for the polysulfide at the (100) surface without/with the presence of ferric hydroxide show very similar results to the fresh unoxidized (100) surface. The hydrophobic character of the polysulfide at the (100) surface without ferric hydroxide revealed by the relatively large simulated contact angle confirms the experimental contact angle measurements for the EDTA washed oxidized pyrite (100) surface. As expected, the simulated contact angle for the polysulfide at the (100) surface with the presence of ferric hydroxide is comparably small and indicates a more hydrophilic surface.

For the elemental sulfur dimers and elemental sulfur 8-memeber rings at the (100) surface without/with the presence of ferric hydroxide, the simulated contact angle measurements gave similar results. The elemental sulfur at the (100) surface without

ferric hydroxide is hydrophobic and floatable, while the elemental sulfur at the (100) surface with the presence of ferric hydroxide becomes relatively hydrophilic and wettable by water. Compared to the polysulfide at the fresh unoxidized (100) surface with ferric hydroxide, the elemental sulfur at the (100) surface with ferric hydroxide has a relatively smaller simulated contact angle. The comparably larger number of ferric hydroxide islands for the elemental sulfur (100) surface should be responsible for this relatively more hydrophilic surface state. More details about the formation of ferric hydroxide islands and the corresponding hydrophilic surface state will be discussed with respect to the interaction between interfacial water, ferric hydroxide, and the pyrite (100) surface in the following paragraphs.

8.2.3 MDS Interfacial Water Structures

MDS snapshots in the x-z plane (left column) and in the y-z plane (right column) for interfacial water at the fresh unoxidized pyrite (100) surface and the polysulfide and elemental sulfur 8-member rings at the (100) surface without/with the presence of ferric hydroxide are presented in Figure 8.12. For the fresh unoxidized (100) surface and the polysulfide at the (100) surface without ferric hydroxide shown in Figure 8.12 (a, b, e, and f), the gap presented between the water phase and the surface, reflecting the "water-excluded volume" or "water exclusion zone", indicates that the interaction between the water molecules and the surface is relatively weak, which is the origin of their macroscopic hydrophobic character. For the elemental sulfur dimers at the (100) surface without ferric hydroxide, which is not presented, the "water exclusion zone" reflecting the relatively weak interaction between water and the surface is also very distinct.

However, for the fresh unoxidized (100) surface and the polysulfide at the (100) surface with ferric hydroxide shown in Figure 8.12 (c, d, g, and f) as well as the elemental sulfur dimers at the (100) surface with ferric hydroxide, the "water exclusion zone" is still obvious. This means that the interaction between water molecules and the surfaces remains weak, even when ferric hydroxide is present at the surface making the surfaces hydrophilic. Thus, the interaction between water molecules and the surfaces is not the origin for the hydrophilic character for the surfaces with the presence of ferric hydroxide. Note that this "water exclusion zone" is not obvious for the elemental sulfur 8-member rings at the (100) surface without/with ferric hydroxide shown in Figure 8.12 (i, j, k, and m), because of the atomic roughness at the surface caused by the elemental sulfur 8-member rings. Although the "water exclusion zone" remains between the ferric hydroxide islands and the (100) surface with/without polysulfide/elemental sulfur, it is more important to note the water structure surrounding the ferric hydroxide.

As is shown in Figure 8.12 (c, d, g, and h), cylindrical ferric hydroxide islands are formed on the fresh unoxidized (100) surface and the polysulfide at the (100) surface. In the cylindrical ferric hydroxide islands, positively charged ferric cations are in the middle and surrounded by negatively charged hydroxide anions, which have their oxygen atoms oriented toward the ferric cations. This structure is the result of electrostatic interaction between the ferric cations and hydroxide anions. Because the cylindrical ferric hydroxide islands are surrounded by water molecules, the ferric cations and hydroxide anions will also have interaction with the surrounding water molecules, which is revealed by the fact that no "water exclusion zone" is present between the water molecules and the ferric hydroxide islands. As is shown in Figure 8.12 (k and m), for the elemental sulfur 8-

member rings at the (100) surface with ferric hydroxide, the ferric hydroxide islands are not cylindrical mainly because of the large number of ferric cations and hydroxide anions, but they still stay close to the elemental sulfur 8-member rings. Again, there is no "water exclusion zone" between the water molecules and the ferric hydroxide islands. The same thing happened in the case for elemental sulfur dimers at the (100) surface with the presence of ferric hydroxide. The interaction between ferric hydroxide and interfacial water molecules should be the origin of the macroscopic relatively hydrophilic character developed during pyrite grinding and the oxidation of the pyrite (100) surface. In this way, the surface has been modified. Air bubbles do not penetrate the water film at the surface. As a result, after oxidation, pyrite particles will be difficult to float at typical collector concentrations.

The number density profiles of water molecules, ferric cations, and hydroxide groups for the fresh unoxidized (100) surface without/with the presence of ferric hydroxide are shown, by way of example, in Figure 8.13. For the fresh unoxidized (100) surface without ferric hydroxide, the first water density peak is 3Å away from the surface, which means water molecules are excluded from the unoxidized fresh (100) surface. This result demonstrates the relatively weak interaction between the water and the fresh unoxidized (100) surface. The number density profiles for the polysulfide, elemental sulfur dimers and elemental sulfur 8-member rings at the (100) surface without ferric hydroxide are similar to the fresh unoxidized (100) surface without ferric hydroxide. The distances between the polysulfide, elemental sulfur dimers and elemental sulfur 8-member rings at the (100) surface without ferric hydroxide and their first water density peak are also about 3Å, indicating relatively weak interaction between interfacial water and such surfaces.

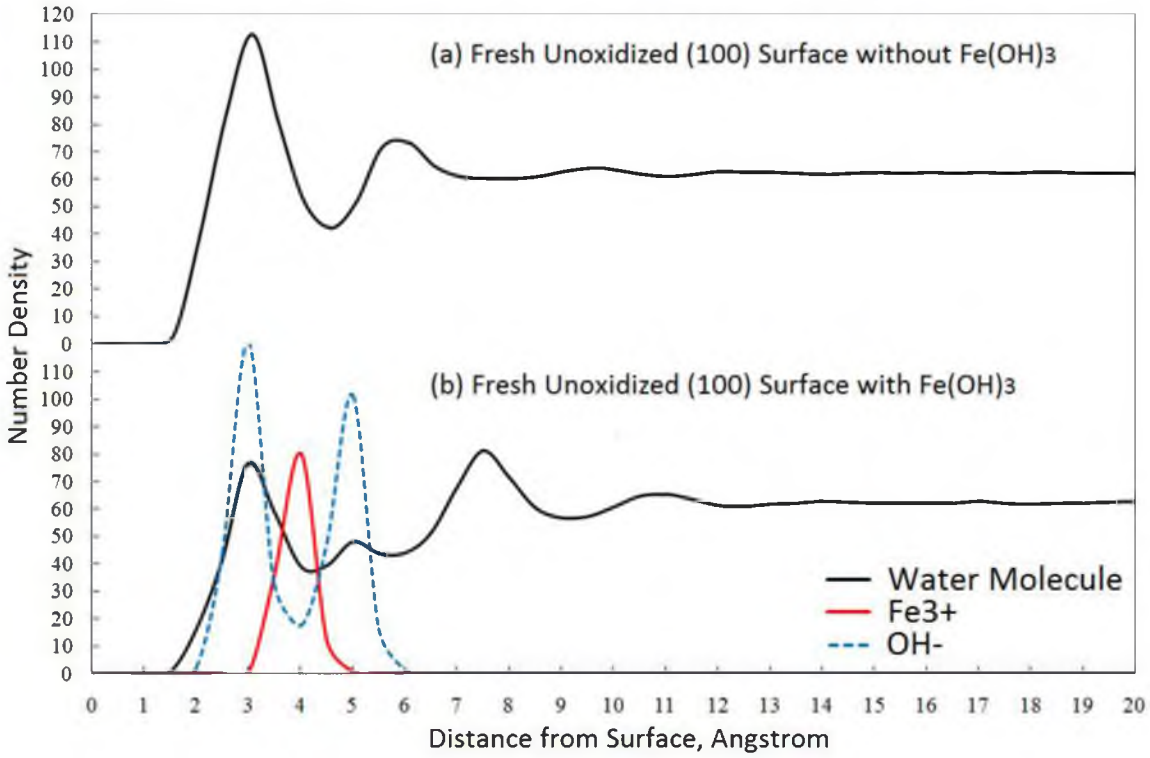

Figure 8.13. Number density distribution plots for the fresh unoxidized pyrite (100) surface without/with the presence of ferric hydroxide.

For the fresh unoxidized (100) surface with the presence of ferric hydroxide, the first water density peak is also about 3Å away from the surface. The number density profile for the polysulfide, elemental sulfur dimers and elemental sulfur 8-member rings at the (100) surface with the presence of ferric hydroxide (not presented) gave the same results. This is consistent with the "water exclusion zone" shown in the snapshots. The fresh unoxidized, polysulfide and elemental sulfur at the (100) surface do not have strong interactions with interfacial water molecules, even when ferric hydroxide is present.

As shown in Figure 8.13 (b), according to the position of the ferric cation and hydroxide anion peaks in the number density profile as well as the decrease of the first water density peak, the ferric hydroxide stays on the surface and occupies a large portion of space. The ferric cation peak is in the middle of two hydroxide anions peaks, which

confirms the structure of cylindrical ferric hydroxide islands observed in Figure 8.12 (c, d). The major point is that the number density profile for the fresh unoxidized (100) surface with ferric hydroxide confirms the elimination of the "water exclusion zone" between water molecules and the ferric hydroxide islands. The information about ferric hydroxide from the number density profile for the polysulfide, elemental sulfur dimers, and elemental sulfur 8-member rings at the (100) surface with ferric hydroxide are identical to the fresh unoxidized (100) surface with ferric hydroxide, except that the ferric cation and hydroxide anion peaks for the two elemental sulfur (100) surfaces are comparably higher and wider because of more ferric hydroxide added on the surface. The fact that the ferric hydroxide stays on the fresh unoxidized (100) surface and the polysulfide and elemental sulfur at the (100) surface during the whole simulation period of about 4 ns confirms the well-known low solubility of ferric hydroxide. The ferric hydroxide islands present on the surface would attract the surrounding water molecules by electrostatic interactions and hydrogen bonding. This condition accounts for the elimination of the "water exclusion zone" at the surface of the ferric hydroxide islands and the hydrophilic surface character induced by the ferric hydroxide.

The water dipole and hydrogen position relative density distributions for the fresh unoxidized pyrite (100) surface without/with the presence of ferric hydroxide are shown as an example in Figure 8.14. The results for polysulfide and elemental sulfur at the (100) surface are similar to the case for the fresh unoxidized (100) surface. For all the cases without the presence of ferric hydroxide, the majority of water molecules in the primary water density layer, which are about 3Å from the surface, have almost the same water dipole orientation and hydrogen position.

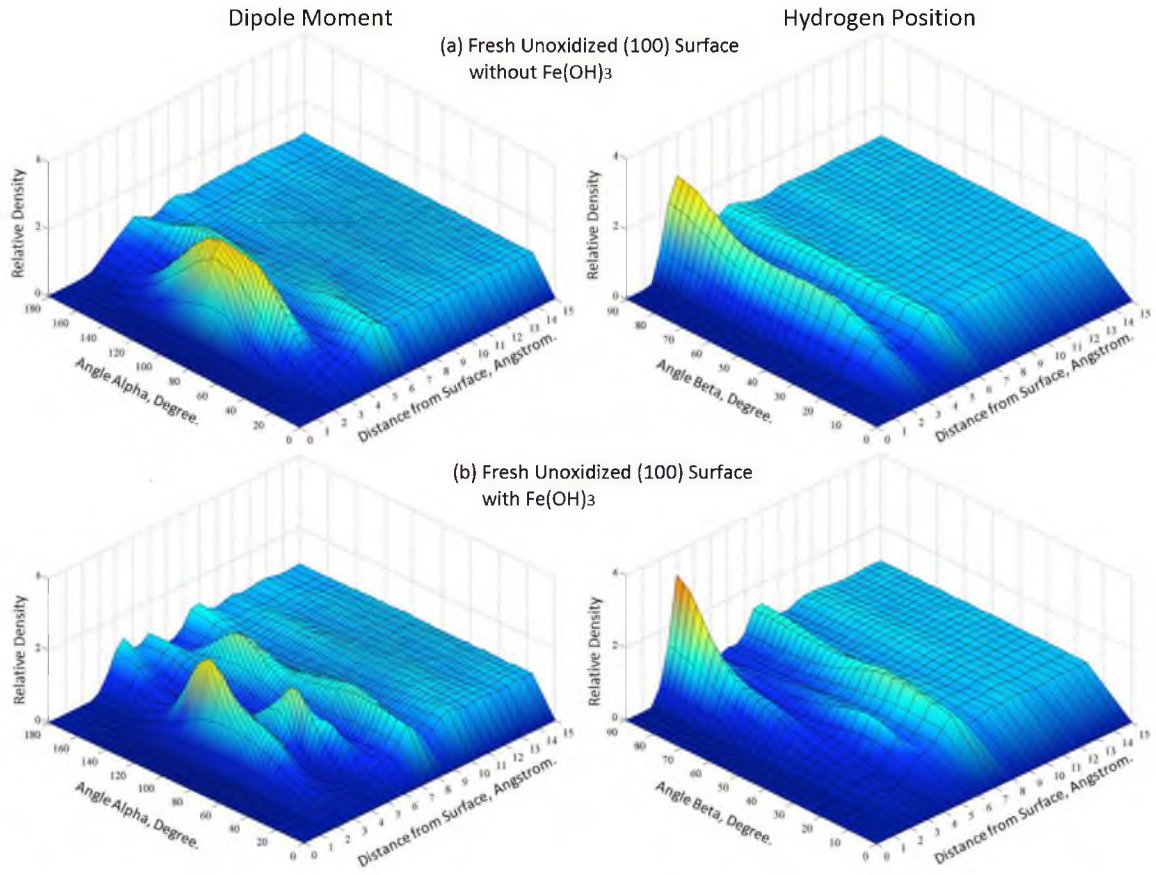

Figure 8.14. Water dipole moment (angle α) and hydrogen position (angle β) relative density distribution along the surface normal for the fresh unoxidized pyrite (100) surface without/with ferric hydroxide.

The water dipole moment is perpendicular to the surface normal and two hydrogens are vibrating or rotating along the dipole moment with the initial and final position parallel to the surface, according to the peak for the α angle at 90°, the peak for the β angle at 90°, and the shoulder of the β angle spreading from 70° to 0°. Thus, the interfacial water molecules for the fresh unoxidized (100) surface and the polysulfide and elemental sulfur at the (100) surface without the presence of ferric hydroxide have relatively weak interaction with the S or Fe atoms of the surface, which confirms the macroscopic hydrophobic character of these surfaces.

Figure 8.14 (b) shows the water dipole and hydrogen position relative density

distributions for the fresh unoxidized (100) surface with the presence of ferric hydroxide. As discussed, the ferric hydroxide islands occupy a large portion of space close to the surfaces. As a result, in the water dipole and hydrogen position relative density distributions for the fresh unoxidized (100) surface with the presence of ferric hydroxide, the volume of the peaks close to the surfaces is comparably smaller than for the fresh unoxidized (100) surface without ferric hydroxide. This is similar for the polysulfide at the (100) surface with ferric hydroxide and even more obvious for the elemental sulfur at the (100) surface with ferric hydroxide, because there is more ferric hydroxide added on the elemental sulfur at the (100) surface.

Instead of a 90° large peak for angle α about 3Å from the surface, for the fresh unoxidized (100) surface with ferric hydroxide, a 105° peak about 3Å from the surface and two other peaks about 5Å from the surface with 75°and 180° α angles are presented. Also, on the fresh unoxidized (100) surface with the presence of ferric hydroxide, there is a relatively large 90° peak for angle β about 3Å from the surface and a small 30° peak for angle β about 5Å away from the surface.

Note that water molecules in the primary water density layer 3Å from the surface are almost parallel to the surface but not rotating or vibrating, indicating relatively weak interaction to the surface but strong interaction with ferric hydroxide. This is also consistent with the water number density results. The relatively less ordered water dipole orientation and hydrogen position of water molecules about 5Å from the surface is the result of electrostatic interaction and hydrogen bonding induced by the ferric hydroxide. The water dipole and hydrogen position analysis results for the polysulfide and elemental sulfur (100) surfaces gave the same conclusion.

The water residence times at the fresh unoxidized (100) surface and the polysulfide and elemental sulfur 8-member rings at the (100) surface without/with the presence of ferric hydroxide are listed in Table 8.5. The water residence time results for the elemental sulfur dimers at the (100) surface is the same as for the elemental sulfur 8-member rings at the (100) surface.

The magnitude of water residence time at the fresh unoxidized (100) surface and the polysulfide and elemental sulfur 8-member rings at the (100) surface without ferric hydroxide is very similar to other hydrophobic selected sulfide mineral surfaces, such as galena (100), chalcopyrite (012), and molybdenite (001) surfaces. These values are much smaller than the over 20 ps water residence times reported for the hydrophilic kaolinite alumina or silica surfaces (Du and Miller, 2007a). The Fe and S atoms at the fresh unoxidized (100) surface and the polysulfide and elemental sulfur at the (100) surfaces without ferric hydroxide do not provide many hydrogen-bonding donors and accepters for the interfacial water molecules.

Table 8.5 Water Residence Time for the Pyrite (100) Surface.

Mineral Surface	Ferric Hydroxide	Water Residence time , ps
Fresh Unoxidized (100) Surface	No	7.5
	Yes	17.2
Polysulfide (100) Surface	No	7.0
	Yes	14.0
Elemental Sulfur 8-Member Rings (100) Surface	No	6.0
	Yes	18.6

Thus, they have relatively weak interaction with the interfacial water molecules, compared to the hydroxyl groups in the kaolinite alumina or silica surfaces. These results confirm the hydrophobic character for the fresh unoxidized (100) surface and for the polysulfide and elemental sulfur at the (100) surface without the presence of ferric hydroxide, as revealed by the experimental and simulated contact angle measurements.

On the other hand, the magnitude of water residence time at the fresh unoxidized (100) surface and the polysulfide and elemental sulfur 8-member rings at the (100) surface with ferric hydroxide is comparably much larger than it is for the cases without ferric hydroxide. These values are close to the water residence time for the hydrophilic sylvite (100) and muscovite (001) surfaces reported by previous MDS studies (Wang et al., 2013; Yin, 2012), which are around 20 ps. This is significant evidence for the strong interaction between the ferric hydroxide and interfacial water molecules at the fresh unoxidized (100) surface and the polysulfide and elemental sulfur at the (100) surface with the presence of ferric hydroxide.

As proven in the simulation, the ferric hydroxide has low solubility and stays on the fresh unoxidized (100) surface and on the polysulfide and elemental sulfur at the (100) surface. Because there are electrostatic interactions and hydrogen bonding between the ferric hydroxide and interfacial water molecules, the interfacial water molecules will be "slowed down" or "stabilized" by the ferric hydroxide islands present on the surface. Thus, the surfaces with the presence of ferric hydroxide have a comparably larger water residence time than the surfaces without ferric hydroxide. The strong interaction between the ferric hydroxide and interfacial water molecules is the origin of the corresponding macroscopic hydrophilic surface character.

Distribution of the average number of hydrogen bonds per water molecule along the surface normal for the fresh unoxidized (100) surface is shown, by way of example, in Figure 8.15. For the fresh unoxidized (100) surface without/with ferric hydroxide, from the surface to the bulk water, the total number of hydrogen bonds per water molecule increases until it reaches a plateau value close to 3.35 about 4 Å from the surface, which is very close to the value of 3.5 reported in the literature (Nieto-Draghi et al., 2003). Note that the number of hydrogen bonds from other water molecules per water molecule equals the total number of hydrogen bonds per water for the fresh unoxidized (100) surface without ferric hydroxide. Unlike the hydrophilic quartz surface, because of the exclusion of water molecules at the fresh unoxidized (100) surface without/with ferric hydroxide, there are very few hydrogen bonds in the interfacial region over a distance of 2 Å from the surface.

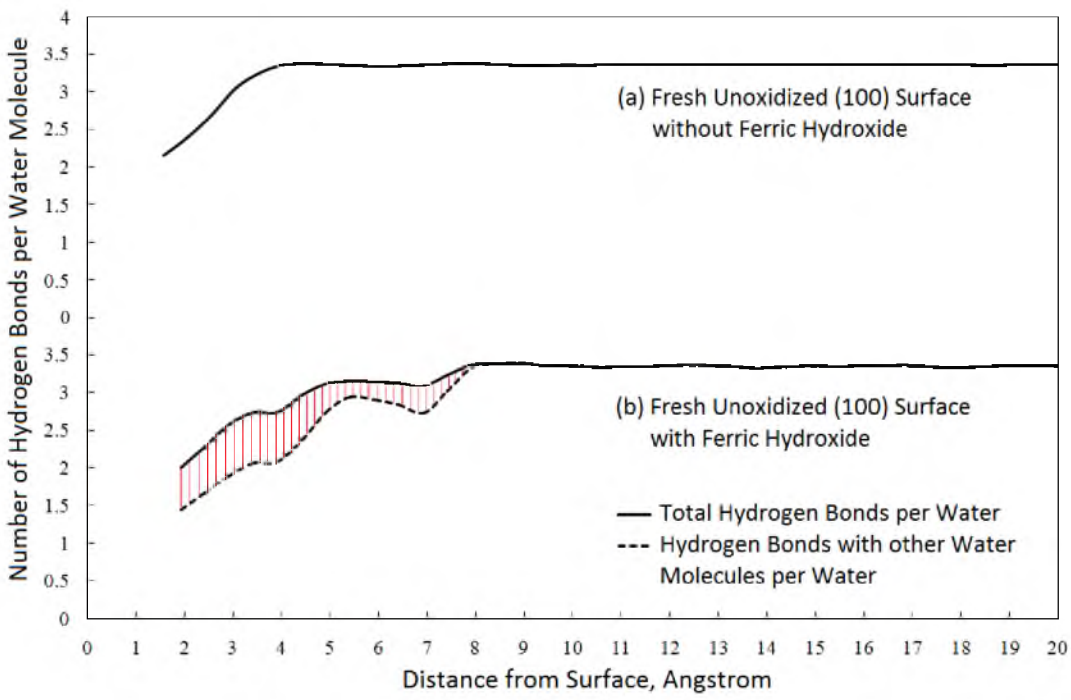

Figure 8.15. Distribution of hydrogen-bonding number per water molecule along the fresh unoxidized pyrite (100) surface without/with ferric hydroxide.

The distinct difference between the distribution of the number of hydrogen bonds per water molecule for the hydrophilic quartz surface and the fresh unoxidized (100) surface without/with ferric indicates that the hydrophilic character for the fresh unoxidized (100) surface with iron hydroxide does not come from the interaction between the surface atoms and interfacial water molecules. Distribution of the average number of hydrogen bonds per water molecule for polysulfide and elemental sulfur at the (100) surface without/with ferric hydroxide showed exactly the same results. This is consistent with our experimental and other simulation discussions.

For the fresh unoxidized (100) surface with the presence of ferric hydroxide, as is shown in Figure 8.15 (b), the red shadowed part between the total number of hydrogen bonds per water molecule and the number of hydrogen bonds from other water molecules per water molecule indicates the hydrogen bonds per water molecule contributed by hydroxide anions. The hydrogen bonding analysis for the polysulfide and elemental sulfur (100) surfaces gave very similar results. The hydroxide anion (OH^-) is a very good acceptor of hydrogen bonds, with the first water molecule binding strongly to form $H_3O_2^-$ (where the proton is off-center, giving rise to a low-barrier hydrogen bond) bihydroxide anions (Abu-Dari et al., 1979). This hydroxide ion $H_3O_2^-$ is much more stable than the hydrogen bonding between two water molecules. Furthermore, these bihydroxide anions will also form weak hydrogen bonding between them and adjacent water molecules. As a result, the hydroxide ions facilitate the interactions among water molecules and make a significant contribution to the hydrophilic character of the fresh unoxidized (100) surface and the polysulfide and elemental sulfur at the (100) surface with the presence of ferric hydroxide.

According to our number density analysis, the ferric hydroxide islands stay in the region less than 7Å from the fresh unoxidized (100) surface and the polysulfide and elemental sulfur at the (100) surface. Thus, Table 8.6 lists the percentage of hydrogen bonds between water and hydroxide anion in the total number of hydrogen bonds in the region less than 7Å from the fresh unoxidized (100) surface and the polysulfide and elemental sulfur at the (100) surface with ferric hydroxide.

For the fresh unoxidized (100) surface and the polysulfide at the (100) surface with ferric hydroxide, about 18% of the hydrogen bonds per water are hydrogen bonds between water molecules and hydroxide anions. This reveals that the hydrogen bonds of interfacial water at the fresh unoxidized (100) surface and the polysulfides at the (100) surface with ferric hydroxide are relatively stronger than at the fresh unoxidized (100) surface and the polysulfide at the (100) surface without ferric hydroxide.

Table 8.6 Proportions of Hydrogen Bonds between Water and Hydroxide in the Total Number of Hydrogen Bonds in the Region Less Than 7Å from the Pyrite (100) Surface.

Mineral Surface	Ferric Hydroxide	$Nh_{water\text{-}hydroxide}/Nh_{total}$, %
Fresh Unoxidized (100) Surface	No	0
	Yes	18.3
Polysulfide at the (100) Surface	No	0
	Yes	17.0
Elemental Sulfur 8-Member Rings at the (100) Surface	No	0
	Yes	22.8

The hydrogen bonding between the hydroxide anions and the interfacial water molecules makes a significant contribution to the macroscopic hydrophilic character for the fresh unoxidized (100) surface and the polysulfide at the (100) surface with the presence of ferric hydroxide. For the elemental sulfur 8-member rings at the (100) surface with the presence of ferric hydroxide, the percentage of hydrogen bonds between water and hydroxide anions is comparably higher, which means the hydrogen bonding interaction of the interfacial water molecules at this surface is relatively stronger. The elemental sulfur dimers at the (100) surface gave the same results. This is consistent with the comparably more hydrophilic character for the elemental sulfur at the (100) surface with the presence of ferric hydroxide revealed in the simulated contact angle measurement and water residence time analysis.

8.2.4 Summary

The famous pyrite oxidation mechanism involving the formation of a metal deficient layer was described using the DFT quantum chemical calculations about the accommodation of ferric hydroxide on the pyrite (100) surface. Based on this pyrite oxidation mechanism, the polysulfide, elemental sulfur dimers and elemental sulfur 8-member rings at the (100) surface were generated by the DFT quantum chemical calculations.

Results of SEM and experimental contact angle measurements for the fresh pyrite, oxidized pyrite and EDTA washed oxidized pyrite (100) surfaces indicate that the formation of iron hydroxide at the oxidized pyrite (100) surface is the origin of the hydrophilic surface state developed during pyrite oxidation.

The force field including the UFF Lennard-Jones parameters and Mulliken charges was used in this MDS study to predict the interfacial water characteristics at the fresh unoxidized (100) surface and the polysulfide and elemental sulfur at the (100) surface without/with the presence of ferric hydroxide.

The simulated contact angle measurements confirmed the relationship between the formation of ferric hydroxide and the corresponding hydrophilic character for the fresh unoxidized (100) surface and the polysulfide and elemental sulfur at the (100) surface with ferric hydroxide.

The MDS results about the interfacial water structures and dynamic properties reveal the hydrophobic character for the fresh unoxidized (100) surface and the polysulfide and elemental sulfur at the (100) surface without the presence of ferric hydroxide, which is consistent with the experimental results. The relatively weak interactions between the surface atoms and the interfacial water molecules are the primary reason for this. On the other hand, for the fresh unoxidized (100) surface and the polysulfide and elemental sulfur at the (100) surface with the presence of ferric hydroxide, the electrostatic interaction and hydrogen bonding between the ferric hydroxide and interfacial water molecules are the origin of their macroscopic hydrophilic character and wettability, according to the MDS analysis about the interfacial water structures and dynamics properties.

8.3 Cu^{2+} Activated Sphalerite (110) Surface

In addition to the experimental contact angle measurements of the fresh and Cu^{2+} activated sphalerite surface as well as the covellite (001) surface, the interfacial water

features at the fresh sphalerite-ZnS (110), copper-zinc sulfide-$CuZnS_2$ (110), villamaninite-CuS_2 (100), and covellite-CuS (001) surfaces are discussed, including simulated contact angles, water number density profiles, water residence time, water dipole orientation, and hydrogen bonding.

8.3.1 Comparison of MDS and Experimental Contact Angles

Table 8.7 lists the simulated contact angles and experimental values for the fresh sphalerite-ZnS (110), Cu^{2+} activated sphalerite, copper-zinc sulfide-$CuZnS_2$ (110), villamaninite-CuS_2 (100), and covellite-CuS (001) surfaces. The relatively small contact angle for the sphalerite-ZnS (110) surface indicates its modest hydrophobic character, which is also revealed by the incomplete flotation of sphalerite in the absence of collectors (Fornasiero and Ralston, 2006; Fuerstenau and Sabacky, 1981).

The experimental contact angle for Cu^{2+} activated sphalerite surface shows a 15° increase from the fresh sphalerite surface. Under similar Cu^{2+} activation conditions (i.e., pH = 5.3, 1×10^{-5} M Cu^{2+}), previous investigation showed that the collectorless flotation recovery of sphalerite increased from 45% to around 80% (Fornasiero and Ralston, 2006). This increase in hydrophobicity after Cu^{2+} activation as revealed by experimental contact angles is consistent with the improved sphalerite floatability.

Compared to the fresh sphalerite-ZnS (110) surface, the villamaninite-CuS_2 (100) and covellite-CuS (001) surfaces have much larger simulated and experimental contact angles, which reveals their natural hydrophobic character. For the villamannite-CuS_2 (100) surface, due to the lack of specimen, the experimental contact angle has not yet been measured.

Table 8.7 Simulated and Experimental for Zinc and Copper Sulfide Surfaces

Mineral Surface	Simulated Contact Angles, degree	Experimental Contact Angles, degree
Fresh Sphalerite (110) Surface	48	42
Cu^{2+} Activated Sphalerite Surface	-	57
$CuZnS_2$ (110) Surface	54	-
Villamaninite (100) Surface	71	-
Covellite (001) Surface	85	65

For covellite-CuS (001) surface, the simulated and experimental contact angles both indicate its hydrophobic character, but the simulated contact angle is relatively larger. The imperfection of the covellite specimen may be the reason for the difference between experimental and MDS results. Though the covellite-CuS (001) surface was polished parallel to the cleavage plane, the cleavage plane itself is not smooth and flat enough, as in the photograph shown from microscopic examination presented in Figure 8.16.

As a result, there would be other unknown covellite surfaces exposed on the specimen surface during polishing, which might compromise the hydrophobic character of the covellite-CuS (001) surface. The oxidation/weathering of the covellite mineral sample might also be the reason for the difference between the experimental and simulated contact angles (Chander, 1991). Note that the covellite-CuS (001) surface is relatively more hydrophobic than the villamaninite-CuS_2 (100) surface, based on their simulated contact angles.

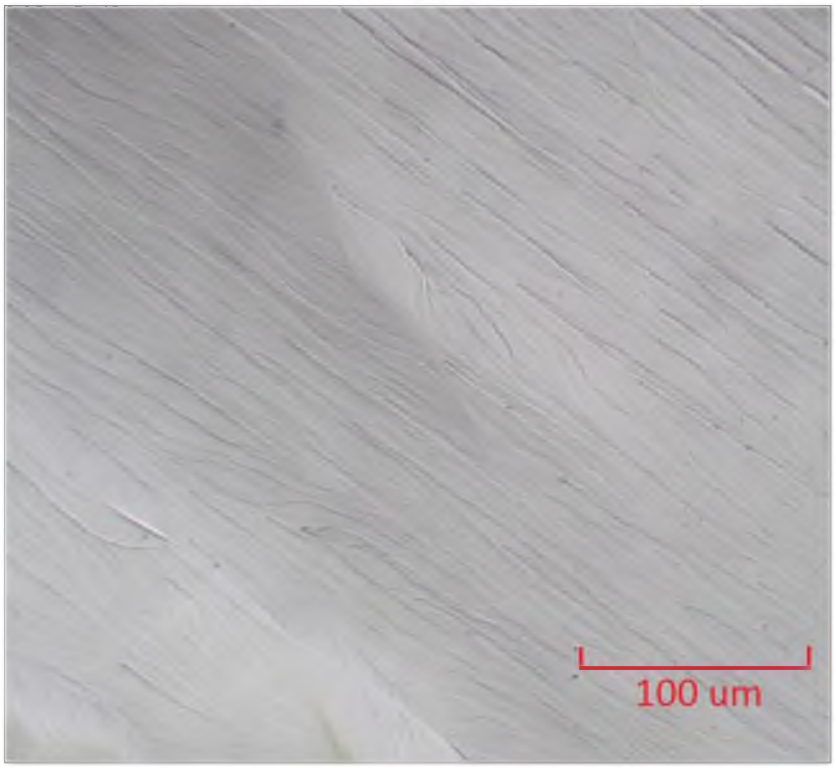

Figure 8.16. Optical microscopy photograph for the cleavage plane of the covellite CuS crystal with reflected light.

As listed in Table 8.7, the simulated contact angle of the copper-zinc sulfide-$CuZnS_2$ (110) surface is close to the experimental contact angle measured for the Cu^{2+} activated sphalerite surface, and its value is between the contact angles of the fresh sphalerite-ZnS (110) surface and the copper sulfide surfaces (i.e., villamaninite-CuS_2 (001) and covellite-CuS (001) surfaces). This possible copper-zinc sulfide product during the Cu^{2+} activation of the sphalerite surface is more hydrophobic than the fresh sphalerite surface. The simulated and experimental contact angle measurements suggest that the more hydrophobic state of the possible copper-zinc sulfide and/or copper sulfide product at the surface of the Cu^{2+} activated sphalerite accounts for the complete floatability of Cu^{2+} activated sphalerite as revealed by the previous collectorless flotation studies (Fornasiero and Ralston, 2006; Fuerstenau and Sabacky, 1981).

In MD simulation, interatomic interaction between two atoms within the cut off distance (11 Å for this study) will be considered. However, the first stoichiometric crystal layer, i.e., the outermost crystal layer around 1.5 Å from the crystal surface, has the most significant effect on the behavior of the interfacial water molecules at the crystal surface. By comparing the compositions of the first stoichiometric crystal layer of these sulfide surfaces, it was found that the surface with greater copper content has a relatively more hydrophobic surface character.

More details about the effect of the surface copper content on the interfacial water and the corresponding hydrophobic surface state will be discussed for the fresh sphalerite-ZnS (110), copper-zinc sulfide-$CuZnS_2$ (110), villamaninite-CuS_2 (100), and covellite-CuS (001) surfaces in the following section.

8.3.2 MDS Interfacial Water Structures

MDS snapshots in the x-z plane (left column) and in the y-z plane (right column) for interfacial water at the fresh sphalerite-ZnS (110), copper-zinc sulfide-$CuZnS_2$ (110), villamaninite-CuS_2 (100), and covellite-CuS (001) surfaces are presented in Figure 8.17. The gap presented between the water phase and the crystal surface, reflecting the "water-excluded volume" or "water exclusion zone," indicates the interaction between the water molecules and the surface. For the fresh sphalerite-ZnS (110), copper-zinc sulfide-$CuZnS_2$ (110), villamaninite-CuS_2 (100), and covellite-CuS (001) surfaces, according to the snapshots, the gaps show the following sequence: sphalerite-ZnS (110) surface < copper-zinc sulfide-$CuZnS_2$ (110) surface < villamaninite-CuS_2 (100) surface < covellite-CuS (001) surface.

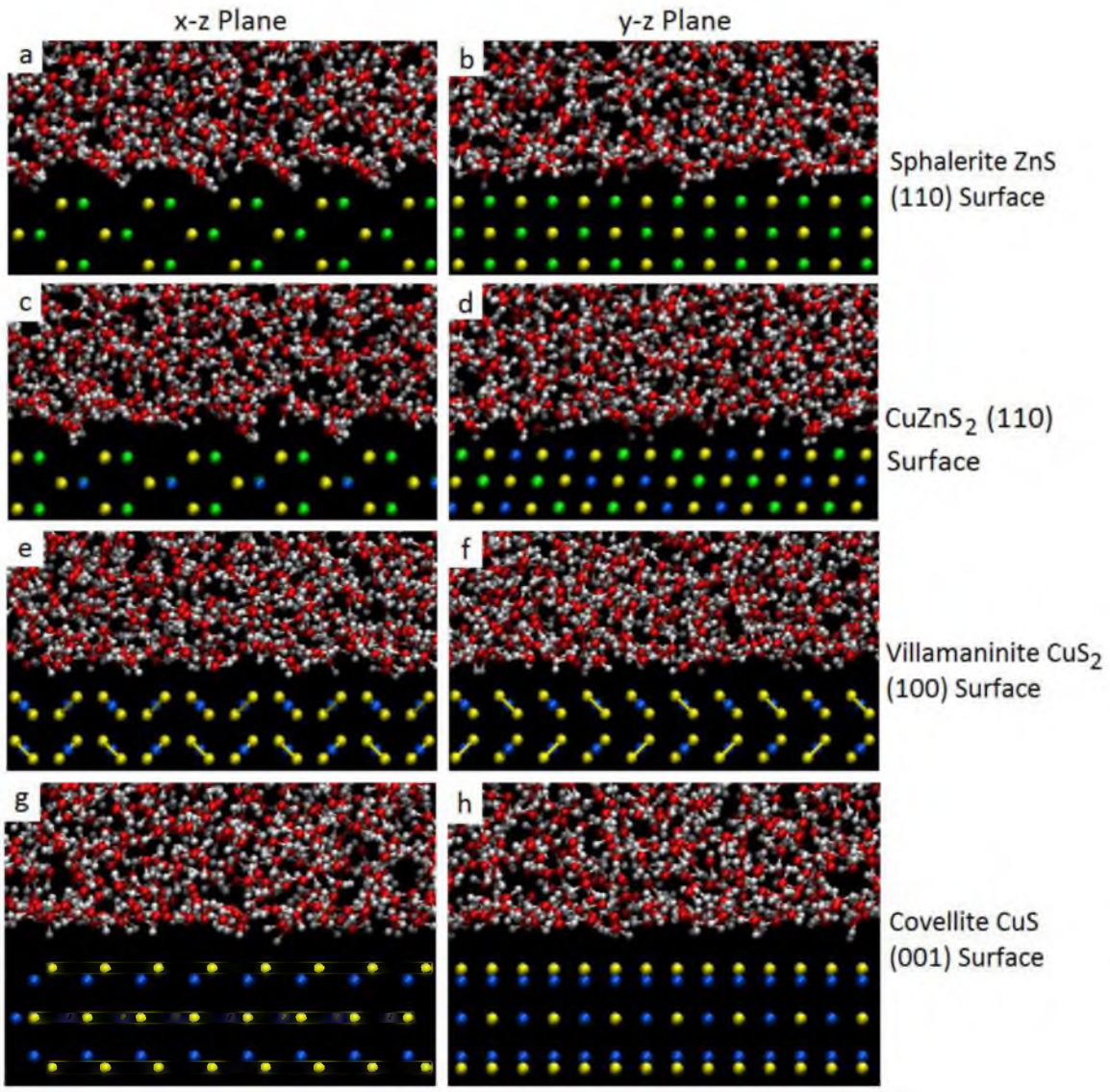

Figure 8.17. MDS snapshots of mineral/water interfaces: (a), (b), fresh sphalerite ZnS (110) surface; (c), (d), $CuZnS_2$ (110) surface; (e), (f), villamaninite CuS_2 (100) surface; (g), (h), covellite CuS (001) surface. The simulation time is at 2 ns. The atoms' color codes are as follow: yellow, S; green, Zn; blue, Cu; red, O; white, H.

The larger gap indicates relatively weak interaction between interfacial water and the surface, which is believed to account for the macroscopic hydrophobic character of the surface. Thus, the hydrophobicity for these crystal surfaces should follow the same sequence, which is consistent with the simulated contact angle results. The gaps between the interfacial water molecules and the crystal surfaces in the snapshots confirm the assumption that the greater the copper content for the Cu-Zn-S surfaces the more hydrophobic the surface state.

The number density profiles for the fresh sphalerite-ZnS (110), copper-zinc sulfide-$CuZnS_2$ (110), villamaninite-CuS_2 (100), and covellite-CuS (001) surfaces are shown in Figure 8.18. As mentioned in previous sections, the first peak of the relative water number density distribution for which the value is greater than 1 is considered as the "primary water density peak" for this surface, which means the water in this region is more condensed than in the bulk.

As expected, due to the hydrophobicity of the copper-zinc sulfide-$CuZnS_2$ (110), villamaninite-CuS_2 (100), and covellite-CuS (001) surfaces, water molecules are excluded from these surfaces. The primary water density peaks for these surfaces are located at least 3 Å away from the surface, and this distance is greater than the distance between hydrogen-bonded water/water interactions, which is approximately 2.8 Å as mentioned in previous sections. These results demonstrate the weak interaction between the water molecules and the sulfide mineral surfaces. Also, the comparably sharper primary water density peak for the covellite-CuS (001) surface indicates the weaker water-surface interaction and a more hydrophobic character when compared to the villamaninite-CuS_2 (100) surface.

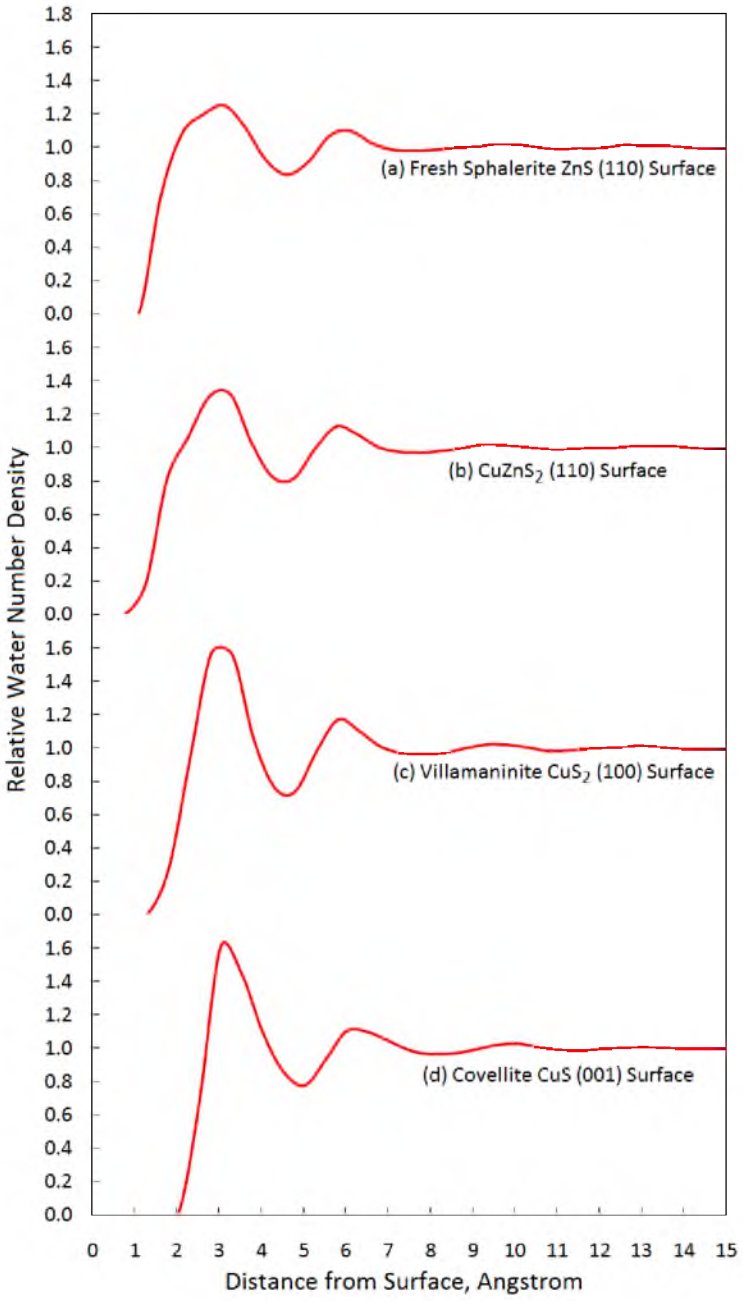

Figure 8.18. Relative water number density profiles at selected mineral surfaces: (a) fresh sphalerite ZnS (110) surface; (b) $CuZnS_2$ (110) surface; (c) villamaninite CuS_2 (100) surface; (d) covellite CuS (001) surface.

Note that for the copper-zinc sulfide-$CuZnS_2$ (110) surface, the relative water number density has a shoulder around 0.9 at 2 Å away from the surface, which indicates a greater interaction between interfacial water and the copper-zinc sulfide-$CuZnS_2$ (110) surface than at the villamaninite-CuS_2 (100) and covellite-CuS (001) surfaces. This analysis is consistent with the simulated contact angle results which show that the villamaninite-CuS_2 (100) and covellite-CuS (001) surfaces are more hydrophobic than the copper-zinc sulfide-$CuZnS_2$ (110) surface. For the fresh sphalerite-ZnS (110) surface, water molecules interact more strongly with the Zn and S atoms at the sphalerite-ZnS (110) surface. The distance between the surface and the primary water density peak for the fresh sphalerite-ZnS (110) surface is around 2.2 Å, which is much smaller than the distance found for other hydrophobic surfaces.

The distinct differences in the water-excluded volume for the fresh sphalerite-ZnS (110), copper-zinc sulfide-$CuZnS_2$ (110), villamaninite-CuS_2 (100), and covellite-CuS (001) surfaces, which are indicated by the primary water density peak, confirm the different interfacial water characteristics for the surfaces with different degrees of hydrophobicity. They also confirm the trend of the hydrophobicity of these surfaces revealed from the simulated contact angles and the MDS snapshots.

The water residence time distributions along the surface normal of the fresh sphalerite-ZnS (110), copper-zinc sulfide-$CuZnS_2$ (110), villamaninite-CuS_2 (100), and covellite-CuS (001) surfaces are shown in Figure 8.19. The magnitude and position of the first peak of the water residence time for the surfaces in this study and some other surfaces from several previous MDS studies are listed in Table 8.8 (Du and Miller, 2007a; Yin, 2012).

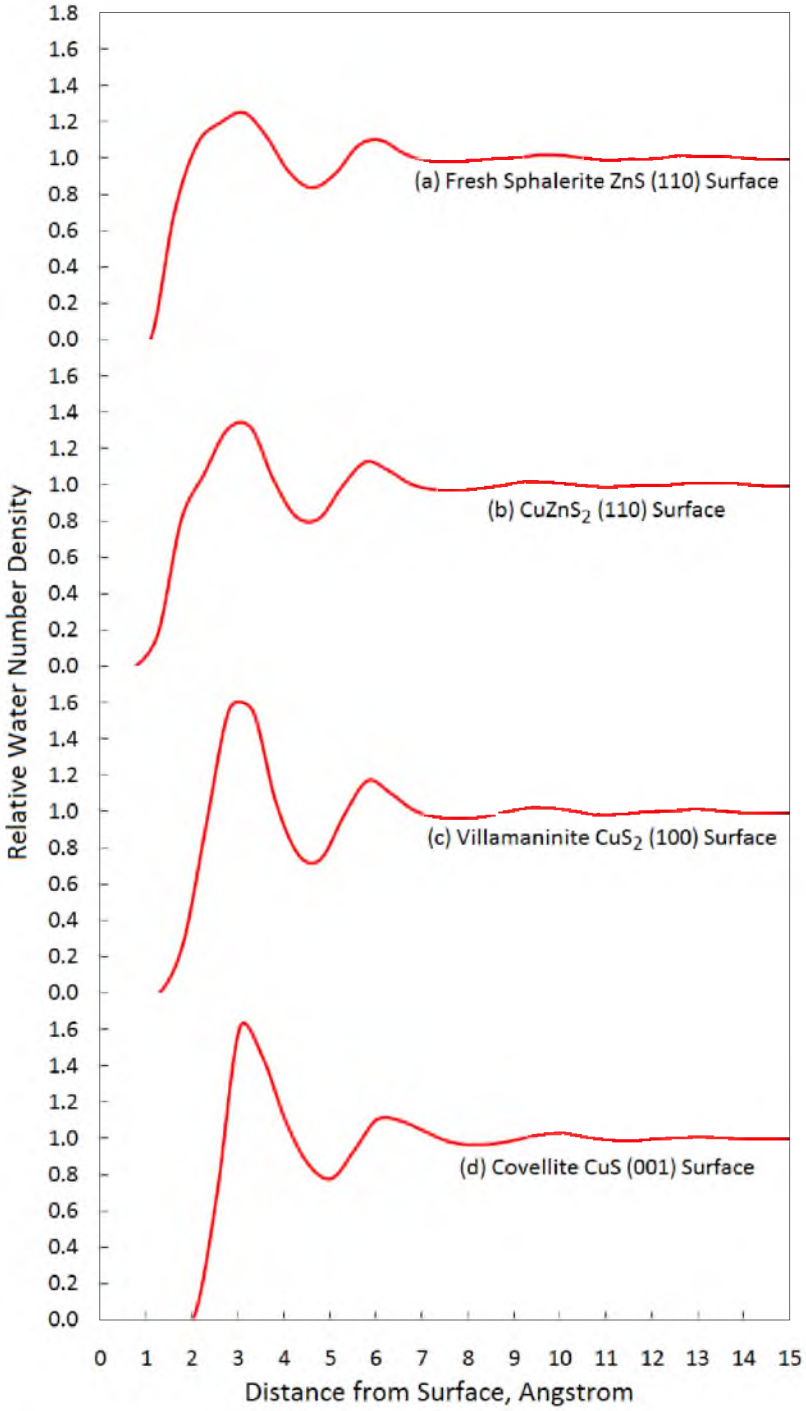

Figure 8.19. Water residence time profiles for selected mineral surfaces: (a) fresh sphalerite ZnS (110) surface; (b) $CuZnS_2$ (110) surface; (c) villamaninite CuS_2 (100) surface; (d) covellite CuS (001) surface.

Table 8.8 Comparison of Interfacial Water Residence Times of Selected Hydrophobic and Hydrophilic Mineral Surfaces

Surface State	Mineral Surface	First Peak for Water Residence Time	
		Distance from Surface (Å)	Magnitude (ps)
Hydrophilic	Muscovite (001) Surface	1.0	25.0
	Kaolinite Alumina Face	2.0	29.3
Hydrophobic	Sphalerite ZnS (110) Surface	2.2	7.8
	$CuZnS_2$ (110) Surface	3.2	6.4
	Villamaninite CuS_2 (100) Surface	3.4	6.9
	Covellite CuS (001) Surface	3.5	6.7
	Pyrite (100) Surface	3.5	7.5

The magnitude of water residence time at the fresh sphalerite-ZnS (110), copper-zinc sulfide-$CuZnS_2$ (110), villamaninite-CuS_2 (100), and covellite-CuS (001) surfaces is very close to other hydrophobic selected sulfide mineral surfaces, such as the pyrite (100) surface. More importantly, these values are much smaller than water residence times at the hydrophilic surfaces, such as muscovite, kaolinite alumina, or silica surfaces. These results indicate the relatively weak interaction between interfacial water and the sulfide mineral surfaces, which is consistent with the natural hydrophobic character of sulfide mineral surfaces under anaerobic conditions.

For the fresh sphalerite-ZnS (110), copper-zinc sulfide-$CuZnS_2$ (110), villamaninite-

CuS_2 (100), and covellite-CuS (001) surfaces, the trend found in the simulated contact angles and water number density profiles was found again in the water residence time analysis. According to Figure 8.19 and Table 8.8, the distances of the first peak for water residence time from the fresh sphalerite-ZnS (110), copper-zinc sulfide-$CuZnS_2$ (110), villamaninite-CuS_2 (100), and covellite-CuS (001) surfaces have the following sequence: sphalerite-ZnS (110) surface < copper-zinc sulfide-$CuZnS_2$ (110) surface < villamaninite-CuS_2 (100) surface < covellite-CuS (001) surface. The closer distance of the first water residence time peak from the surface indicates the stronger interaction between interfacial water molecules and the surface as well as a relatively more hydrophilic surface state. Thus, the water residence time analysis for the fresh sphalerite-ZnS (110), copper-zinc sulfide-$CuZnS_2$ (110), villamaninite-CuS_2 (100), and covellite-CuS (001) surfaces gives the same trend for the hydrophobicity of these surfaces described in earlier paragraphs.

The water dipole and hydrogen position relative density distributions for the fresh sphalerite-ZnS (110), copper-zinc sulfide-$CuZnS_2$ (110), villamaninite-CuS_2 (100), and covellite-CuS (001) surfaces are shown in Figure 8.20. For the fresh sphalerite-ZnS (110) surface, approximately 2 Å from the surface, a large peak with the angle α at 90° and angle β around 50° indicates that the majority of water molecules in the first water layer have their dipole perpendicular to the surface normal (i.e., water dipole parallel to the surface) and two hydrogen atoms oriented about 50° to the surface normal (i.e., one of the two Hydrogen atoms in the water molecule is inclined toward the surface), which reveals the relatively stronger interaction between the interfacial water molecules and surface. This peak does not show up in the case of the copper-zinc sulfide-$CuZnS_2$ (110), villamaninite-CuS_2 (100), and covellite-CuS (001) surfaces.

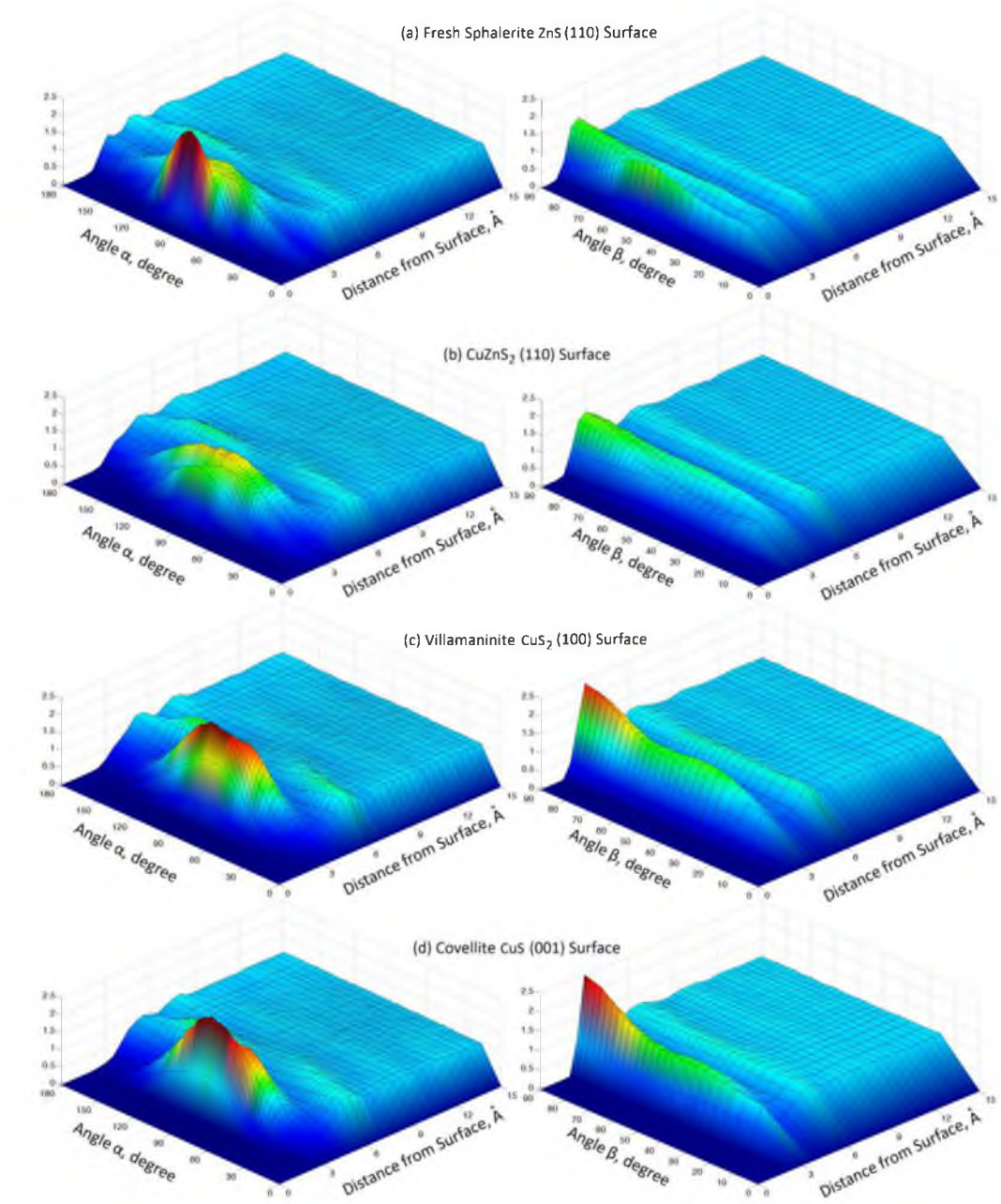

Figure 8.20. Water dipole moment (angle α) and hydrogen position (angle β) relative density distribution along the surface normal at selected mineral surfaces: (a) fresh sphalerite ZnS (110) surface; (b) $CuZnS_2$ (110) surface; (c) villamaninite CuS_2 (100) surface; (d) covellite CuS (001) surface.

For the copper-zinc sulfide-$CuZnS_2$ (100) surface, instead of a peak, a shoulder with the same α and β angles can be observed at the same position (approximately 2 Å from the surface), indicating a relatively weak interaction between the water molecules in the first layer and the copper-zinc sulfide-$CuZnS_2$ (110) surface when compared to the sphalerite-ZnS (110) surface. The orientation of the hydrogen atom of interfacial water toward the sphalerite-ZnS (110) and copper-zinc sulfide-$CuZnS_2$ (110) surfaces is because of the electrostatic interaction between the positively charged hydrogen atoms and the negatively charged S atoms at the surface. This organization can be observed from the MDS snapshots of interfacial water molecules at the sphalerite-ZnS (110) and copper-zinc sulfide-$CuZnS_2$ (110) surfaces in Figure 8.18 (a) and (c). The reason that this interaction is weaker at the copper-zinc sulfide-$CuZnS_2$ (110) surface is the comparably smaller atomic partial charge for the S atoms in the copper-zinc sulfide-$CuZnS_2$ structure than in the sphalerite-ZnS structure. Though the crystal structures for the copper-zinc sulfide-$CuZnS_2$ and sphalerite-ZnS crystals are similar, atomic partial charges for both the Zn and S atoms in the copper-zinc sulfide-$CuZnS_2$ crystal are smaller than they are in the sphalerite ZnS crystal. When copper substitutes at the zinc sulfide surface, the Zn and S atomic partial charges are reduced, which makes the surface less "polar". It is well established that a polar surface exhibits a hydrophilic surface state because of stronger interaction between water and the surface whereas the nonpolar surface has a hydrophobic character due to the relatively weak water/surface interactions (Miller, 2000). Thus, it is the copper substitution which makes the sphalerite-ZnS surface less polar and thus less interaction with water, becoming more hydrophobic, when activated.

For the villamaninite-CuS_2 (100) and covellite-CuS (001) surface, there is a large

peak for the α angle at 90° (i.e., water dipole parallel to the surface), a large peak for the β angle at 90°, and a shoulder of the β angle from 70° to 0° (i.e., two Hydrogen atoms rotating or vibrating along the dipole moment with initial and final positions parallel to the surface). The results confirm the weaker interaction between the interfacial water and the villamaninite-CuS_2 (100) and covellite-CuS (001) surfaces as compared to the sphalerite-ZnS (110) and copper-zinc sulfide-$CuZnS_2$ (110) surfaces. Note that the peak at the covellite-CuS (001) surface is higher and sharper than the peak at the villamaninite-CuS_2 (100) surface. Dipole moment of the water molecules in the first water layer are more oriented parallel to the covellite-CuS (001) surface than for the villamaninite-CuS_2 (100) surface, indicating the relatively weak interaction between interfacial water and the covellite-CuS (001) surface than the villamaninite-CuS_2 (001) surface. This is consistent with the trend of hydrophobicity of the fresh sphalerite-ZnS (110), copper-zinc sulfide-$CuZnS_2$ (110), villamaninite-CuS_2 (100), and covellite-CuS (001) surfaces from simulated contact angle, water number density, and water residence time analysis. The atomic partial charges and the surface polarity decrease along the sequence, in which the copper content increases: sphalerite-ZnS (110) surface; copper-zinc sulfide-$CuZnS_2$ (110) surface; villamaninite-CuS_2 (100) surface; covellite-CuS (001) surface. Thus, the electrostatic interactions between interfacial water and the surface decrease, but the surface hydrophobicity increases following the same sequence. In addition to the decrease of surface polarity caused by the copper substitution, according to the UFF parameters, Cu atoms have more VdW repulsive interaction with the interfacial water molecules than the Zn atoms (Rappé et al., 1992). This might also have an effect on the relatively greater hydrophobic character for the Cu^{2+} activated sphalerite surface.

Distribution of the average number of hydrogen bonds per water molecule along the surface normal for the fresh sphalerite-ZnS (110), copper-zinc sulfide-$CuZnS_2$ (110), villamaninite-CuS_2 (100), and covellite-CuS (001) surfaces is presented in Figure 8.21. For the fresh sphalerite-ZnS (110), copper-zinc sulfide-$CuZnS_2$ (110), villamaninite-CuS_2 (100), and covellite-CuS (001) surfaces, from the surface to the bulk water, the total number of hydrogen bonds per water molecule increases until it reaches a plateau value close to 3.35 about 4 Å from the surface, very close to the value of 3.5 reported in the literature (Nieto-Draghi et al., 2003). Although the number of hydrogen bonds per water molecule for the fresh sphalerite-ZnS (110), copper-zinc sulfide-CuZnS2 (110), villamaninite-CuS2 (100), and covellite-CuS (001) surfaces fluctuate somewhat before they reach the plateau, none of the surfaces exceed the plateau value for hydrogen bonding of 3.35 for bulk water.

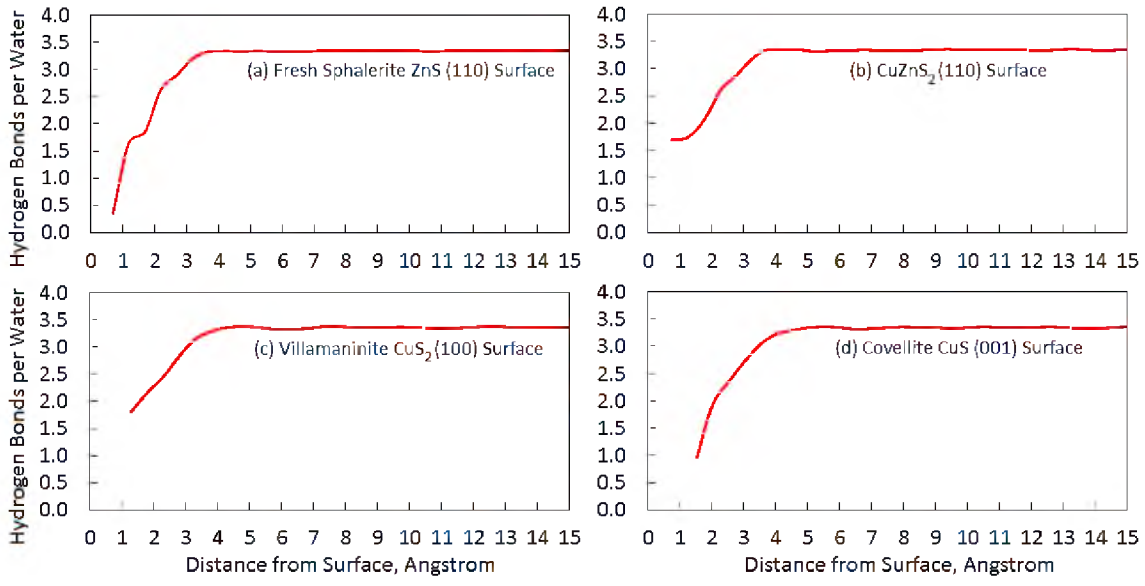

Figure 8.21. Distribution of hydrogen-bonding number per water molecule along the surface normal for selected mineral surfaces: (a) fresh sphalerite ZnS (110) surface; (b) $CuZnS_2$ (110) surface; (c) villamaninite CuS_2 (100) surface; (d) covellite CuS (001) surface.

Because of the exclusion of water molecules at the fresh sphalerite-ZnS (110), copper-zinc sulfide-$CuZnS_2$ (110), villamaninite-CuS_2 (100), and covellite-CuS (001) surfaces, there are very few hydrogen bonds in the interfacial region over a distance of 1 Å from the surface. The distinct differences between the distribution of the number of hydrogen bonds per water molecule for the hydrophilic quartz surface and the fresh sphalerite-ZnS (110), copper-zinc sulfide-$CuZnS_2$ (110), villamaninite-CuS_2 (100), and covellite-CuS (001) surfaces reveals the natural hydrophobic character for the fresh sphalerite-ZnS (110), copper-zinc sulfide-$CuZnS_2$ (110), villamaninite-CuS_2 (100), and covellite-CuS (001) surfaces.

8.3.3 Summary

Results of experimental contact angle measurements for the fresh and Cu^{2+} activated sphalerite surfaces as well as the covellite-CuS (001) surface indicate that the modest hydrophobicity of the sphalerite surface would be altered toward the strong hydrophobicity of the covellite-CuS (001) surface during the Cu^{2+} activation process.

Based on the metathetic exchange reaction for Cu^{2+} activation of sphalerite, a copper-zinc sulfide-$CuZnS_2$ crystal was established from the chalcopyrite crystal structure by DFT calculations. The force field including the UFF Lennard-Jones parameters and Mulliken charges was used in the MD simulations to predict the interfacial water characteristics at the fresh sphalerite-ZnS (110), copper-zinc sulfide-$CuZnS_2$ (110), villamaninite-CuS_2 (100), and covellite-CuS (001) surfaces. The simulated contact angle measurements are consistent with the experimental measurements and confirmed the increase in hydrophobicity of the sphalerite surface during the Cu^{2+} activation process. According to the simulated contact angles, the hydrophobicity increases according to the

following sequence: sphalerite-ZnS (110) surface; copper-zinc sulfide-$CuZnS_2$ (110) surface; villamaninite-CuS_2 (100) surface; covellite-CuS (001) surfaces, i.e., the copper content at the surface increases.

This trend was confirmed by the MDS results regarding the interfacial water structures and dynamic properties, including water density distribution, water residence time, water dipole orientation, and hydrogen bonding analysis. It has been revealed that the interactions between interfacial water and the surface decrease along the same sequence, mainly because of the decrease of surface polarity caused by the increased copper content of the surface and the relatively stronger VdW repulsive force of the copper atoms than Zn atoms. Thus, the copper content at the sphalerite surface as a result of Cu^{2+} activation is the origin of a greater hydrophobic character.

CHAPTER 9

CONCLUSIONS

9.1 Summary of Results

A summary of the sessile drop contact angles, MDS interfacial water features and SFVS results for the selected hydrophobic and hydrophilic mineral surfaces, reported in Chapter 4 and 5, are presented in Table 9.1. The selected hydrophobic mineral surfaces are the graphite (001) surface and OTS monolayer on quartz. The selected hydrophilic mineral surfaces include the quartz (001), sapphire (001), and gibbsite (001) surfaces. The MDS sessile drop contact angles for the selected mineral surfaces are consistent with the corresponding experimental values.

The MDS interfacial water features at the selected mineral surfaces include the water exclusion thickness, water dipole orientation, water residence time, and hydrogen bonds per water molecule at the interface.

The water exclusion zone thickness for a hydrophobic mineral surface is around 3 Å, such as the graphite (001) surface. The surface roughness at the OTS monolayer caused by the stretching of OTS molecules is responsible for its 2.5 Å water exclusion thickness. The water exclusion thickness for a hydrophilic mineral surface from the water number density profile is less than 2 Å, such as the oxide/hydroxide mineral surfaces listed in Table 9.1.

Table 9.1 Comparison between Contact Angle and Interfacial Water Features of the Selected Hydrophobic and Hydrophilic Mineral Surfaces.

Selected Mineral Surface	Contact Angle, degree		Exclusion Zone Thickness, Å	Water Residence Time, ps	Water Dipole Orien-tation	H-bond per Water at Interface	3700cm^{-1} Peak in SFVS Spectrum
	Exp.	MDS					
Graphite (001) Surface	92	86	3.2	7.2	Free OH	2.0	Yes
OTS Monolayer	105	108	2.5	4.7	Free OH	2.0	Yes
Quartz (001) Surface	5	9	0.5	44.6	Highly Ordered	4.7	No
Sapphire (001) Surface	14	11	1.0	41.8	Highly Ordered	3.4	Yes
Gibbsite (001) Surface	2	0	1.5	15.0	Highly Ordered	3.4	-

The water residence time is less than 10 ps for a hydrophobic mineral surface but greater than 20 ps for a hydrophilic mineral surface, according to Table 9.1 and previous MDS studies (Wang et al., 2013; Yin, 2012). From the water dipole orientation and hydrogen bonding analysis, at a hydrophobic mineral surface, the "free OH" vibration has been identified as a characteristic feature, and these interfacial water molecules have only 2 hydrogen bonds per water molecule. However, at a hydrophilic mineral surface, interfacial water molecules are highly ordered and have the same or more hydrogen bonds per water molecule compared to bulk water (3.4 hydrogen bonds per water for the SPC/E water model).

The 3700 cm^{-1} "free OH" peak has been found in the SFVS spectrum of interfacial water molecules at the hydrophobic graphite (001) surface and OTS monolayer but not at the hydrophilic quartz surface, which supports the results of the MDS water dipole orientation analysis and hydrogen bonding analysis. There is a 3700 cm^{-1} peak present in the SFVS spectrum of the sapphire/water interface, but it has been proved in section 5.3 that this peak is from OH groups at the hydrated sapphire surface but not interfacial water molecules. After rinsed with acetone, ethanol, and deionized water, the sapphire specimen was blown dry with nitrogen at room temperature and treated in Argon plasma for 15 minutes. During surface preparation, the OH groups could be generated by the hydroxylation of the sapphire surface and remain on the sapphire surface, which has been established in a previous SFVS study (Zhang et al., 2008).

According to the results for MD simulations of a water drop spreading at the hydrophobic molybdenite (001) surface and the hydrophilic quartz (001) surface in Chapter 6, a longer simulation time is required for spreading at the hydrophilic mineral

surface to reach equilibrium, because of more area to cover at the hydrophilic mineral surface. For the hydrophobic molybdenite (001) surface, the MDS advancing and receding contact angles are similar, but the experimental advancing contact angle is larger than the receding contact angles. On the other hand, the MDS advancing and receding contact angles of the hydrophilic quartz (001) surface are the same, while the MDS advancing contact angle is larger than the MDS receding contact angle. Regardless of the influence of surface roughness of the surfaces, the experimental contact angles of mm size water drops are consistent with the MDS contact angles of nm size water drops for the hydrophobic molybdenite (001) surface and the hydrophilic quartz (001) surface.

Bubble attachment MD simulations are reported in Chapter 7. A nitrogen bubble attached to the hydrophobic molybdenite (001) surface and a contact angle was established, but film rupture did not occur at the hydrophilic quartz (001) surface. The relatively weak interaction between the interfacial water molecules and the hydrophobic molybdenite (001) surface is the origin of the bubble attachment phenomena. The well-known film thinning, rupture, and displacement process associated with bubble attachment was observed in MD simulations. The MDS bubble attachment contact angles of the hydrophobic molybdenite (001) surface and the hydrophilic quartz (001) surface are consistent with the corresponding experimental captive bubble contact angles.

Wettability and interfacial water features of sulfide/telluride mineral surfaces, including the calaverite (001), chalcopyrite (110), galena (100), pyrite (100), molybdenite face, molybdenite armchair-edge, molybdenite zigzag-edge, and sphalerite (110) surfaces, have been studied by MDS, as reported in section 8.1. The MDS contact angles are consistent with experimental results. The water exclusion zone of over 3 Å is found at

the hydrophobic sulfide/telluride mineral surfaces, such as the molybdenite face, calaverite (001), chalcopyrite (110), galena (100), and pyrite (100) surfaces. The moderately hydrophobic sulfide mineral surfaces, such as the molybdenite armchair-edge, molybdenite zigzag-edge, and sphalerite (110) surfaces, have a water exclusion zone thickness about 2.5 Å. The MDS interfacial water features reveal the relatively weak interaction between interfacial water and the selected sulfide/telluride mineral surfaces, which accounts for the origin of the natural hydrophobic character of the sulfide/telluride minerals under anaerobic conditions.

The MDS contact angles for the oxidized pyrite (100) surface with and without ferric hydroxide support the experimental contact angle measurements in section 8.2. The oxidized pyrite (100) surface with ferric hydroxide is hydrophilic and can be wetted by water. According to the MDS interfacial water analysis, the hydrogen bonding interaction between the interfacial water and ferric hydroxide molecules are responsible for the hydrophilic character of the oxidized pyrite (100) surface with ferric hydroxide. The interfacial water molecules at the oxidized pyrite (001) surface with ferric hydroxide have a water residence time over 10 ps and are highly ordered instead of having "free OH" vibration. According to the MDS hydrogen bonding analysis, the interfacial water molecules at the oxidized pyrite (001) surface with ferric hydroxide form hydrogen bonds with the OH groups from ferric hydroxide.

The MDS and experimental contact angles of the fresh sphalerite (110) surface show a modest hydrophobic character. In section 8.3, the results of MDS contact angle measurements indicate that the surface becomes more hydrophobic as the copper content at the surface increases, which is the result of Cu^{2+} activation. The experimental results

and MDS interfacial water features confirm this hypothesis. The interfacial water molecules at the surface with more copper content are less ordered (more "free OH" vibration), and have relatively weak interaction with the surface, as revealed by the water dipole orientation analysis. The copper content at the sphalerite surface as a result of Cu^{2+} activation is the origin of a greater hydrophobic character.

9.2 Research Contributions

The MD simulations of the selected natural hydrophobic mineral surface (graphite), collector modified hydrophobic mineral surface (OTS monolayer), and natural hydrophilic mineral surfaces (quartz, sapphire, and gibbsite) are reported and systematically considered for the interfacial water features, including MDS contact angles, "water exclusion zone", water number density profile, water dipole orientation, water residence time, and hydrogen bonding analysis. In addition, the MDS results are verified by experimental techniques, such as contact angle measurement and SFVS.

The effects of spreading time, advancing/receding contact angles, and drop size on sessile drop contact angle measurements were studied systematically by both MDS and experiments. The MDS advancing and receding contact angles of the molybdenite (001) and quartz (001) surfaces have never been reported.

The MD simulations of bubble attachment at the molybdenite (001) and quartz (001) surfaces, which include about a quarter of a million atoms in the simulation system, are reported for the first time and compared to experimental results. The kinetics of the MDS bubble attachment process is discussed with respect to film thinning, rupture, and displacement.

Wettability and MDS interfacial water features of sulfide/telluride mineral surfaces are reported, which have not been reported. The MDS interfacial water features of selected sulfide/telluride mineral surfaces under anaerobic conditions, Cu^{2+} activated spaherite (110), and oxidized pyrite (100) surfaces are studied systematically to determine which interfacial water features best identify the wetting characteristics of selected mineral surfaces.

Finally, a set of Fortran programs was developed in this dissertation research to extract molecular information from molecular trajectories generated by MD simulations. The analysis codes generate molecular information, including 2-dimensional plot of water drop and nitrogen bubble, number density profiles, water number density profile, water dipole orientation, water residence time, and number of hydrogen bonds per water.

9.3 Future Research Topics

Bubble attachment MD simulations require higher computational capacities and are time consuming, so in this dissertation research only two simulation systems, nitrogen bubble attachment at molybdenite and quartz surfaces, were studied. Such simulations require about 4 weeks to complete. The MDS nitrogen bubble attachment contact angles at other mineral surfaces, for example pyrite, will be measured and compared with molybdenite and quartz. In addition, other gas phases of the bubble, such as CO_2 should be considered in the future. The bubble attachment MD simulations use a two point model to simulate nitrogen molecules. To better describe the kinetics of the nitrogen/water interface, a three point model can be used in the bubble attachment MD simulations (Somasundaram et al., 1999). The kinetics and bubble attachment time

analysis of MD bubble attachment simulations should be considered and compared with experimental results in future research.

The MDS interfacial water analysis in this dissertation research focuses on the structural and dynamic properties of interfacial water molecules. The energetic properties of interfacial water, such as surface tension, can be calculated from MD simulations (Dang and Chang, 1997). In the future research, the MDS surface tension of the selected mineral/water interfaces should be calculated and discussed with the respect to interfacial water features.

REFERENCES

Abraham, F.F., 1978. The interfacial density profile of a Lennard-Jones fluid in contact with a (100) Lennard-Jones wall and its relationship to idealized fluid/wall systems: A Monte Carlo simulation. The Journal of Chemical Physics 68, 3713-3716.

Abu-Dari, K., Raymond, K.N., Freyberg, D.P., 1979. The bihydroxide ($H_3O_2^-$) anion. A very short, symmetric hydrogen bond. Journal of the American Chemical Society 101, 3688-3689.

Afifi, A.M., Kelly, W.C., Essene, E.J., 1988. Phase relations among tellurides, sulfides, and oxides; Pt. II, Applications to telluride-bearing ore deposits. Economic Geology 83, 395-404.

Argyris, D., Tummala, N.R., Striolo, A., Cole, D.R., 2008. Molecular structure and dynamics in thin water films at the silica and graphite surfaces. The Journal of Physical Chemistry C 112, 13587-13599.

Beaussart, A., Parkinson, L., Mierczynska-Vasilev, A., Beattie, D.A., 2012. Adsorption of modified dextrins on molybdenite: AFM imaging, contact angle, and flotation studies. Journal of colloid and interface science 368, 608-615.

Berendsen, H., Grigera, J., Straatsma, T., 1987. The missing term in effective pair potentials. Journal of Physical Chemistry 91, 6269-6271.

Buckingham, R.A., 1938. The classical equation of state of gaseous helium, neon and argon, Proceedings of the Royal Society of London A: Mathematical, Physical and Engineering Sciences. The Royal Society, 264-283.

Buckley, A., Woods, R., 1987. The surface oxidation of pyrite. Applied Surface Science 27, 437-452.

Buckley, A., Woods, R., Wouterlood, H., 1989. An XPS investigation of the surface of natural sphalerites under flotation-related conditions. International Journal of Mineral Processing 26, 29-49.

Buckley, A.N., Woods, R., 1984a. An X-ray photoelectron spectroscopic study of the oxidation of chalcopyrite. Australian Journal of Chemistry 37, 2403-2413.

Buckley, A.N., Woods, R., 1984b. An X-ray photoelectron spectroscopic study of the oxidation of galena. Applications of surface science 17, 401-414.

Cao, Q., Wang, X., Miller, J.D., Cheng, F., Jiao, Y., 2011. Bubble attachment time and FTIR analysis of water structure in the flotation of sylvite, bischofite and carnallite. Minerals Engineering 24, 108-114.

Chander, S., 1991. Electrochemistry of sulfide flotation: growth characteristics of surface coatings and their properties, with special reference to chalcopyrite and pyrite. International journal of mineral processing 33, 121-134.

Chander, S., Fuerstenau, D., 1972. On the natural floatability of molybdenite. Trans. AIME 252, 62-69.

Cheng, F., Cao, Q., Guan, Y., Cheng, H., Wang, X., Miller, J.D., 2013. FTIR analysis of water structure and its influence on the flotation of arcanite (K_2SO_4) and epsomite ($MgSO_4 \cdot 7H_2O$). International Journal of Mineral Processing 122, 36-42.

Chowdhuri, S., Chandra, A., 2001. Molecular dynamics simulations of aqueous NaCl and KCl solutions: Effects of ion concentration on the single-particle, pair, and collective dynamical properties of ions and water molecules. The Journal of Chemical Physics 115, 3732-3741.

Clarke, P., Fornasiero, D., Ralston, J., Smart, R.S.C., 1995. A study of the removal of oxidation products from sulfide mineral surfaces. Minerals Engineering 8, 1347-1357.

Cygan, R.T., Liang, J.-J., Kalinichev, A.G., 2004. Molecular models of hydroxide, oxyhydroxide, and clay phases and the development of a general force field. The Journal of Physical Chemistry B 108, 1255-1266.

Dana, J.D., 1869. A system of mineralogy.

Dang, L.X., Chang, T.-M., 1997. Molecular dynamics study of water clusters, liquid, and liquid–vapor interface of water with many-body potentials. The Journal of chemical physics 106, 8149-8159.

Dang, L.X., Pettitt, B.M., 1990. A theoretical study of like ion pairs in solution. Journal of Physical Chemistry 94, 4303-4308.

Dang, L.X., Smith, D.E., 1995. Comment on ''Mean force potential for the calcium–chloride ion pair in water''[J. Chem. Phys. 99, 4229 (1993)]. The Journal of chemical physics 102, 3483-3484.

De Leeuw, N., Purton, J., Parker, S., Watson, G., Kresse, G., 2000. Density functional theory calculations of adsorption of water at calcium oxide and calcium fluoride surfaces. Surface science 452, 9-19.

Delley, B., 2000. DMol3 DFT studies: from molecules and molecular environments to surfaces and solids. Computational materials science 17, 122-126.

Downs, R.T., Hall-Wallace, M., 2003. The American Mineralogist crystal structure

database. American Mineralogist 88, 247-250.

Drelich, J., Miller, J.D., 1994. The effect of solid surface heterogeneity and roughness on the contact angle/drop (bubble) size relationship. Journal of colloid and interface science 164, 252-259.

Drelich, J., Miller, J.D., 2012. Induction time measurements for air bubbles on chalcopyrite, bornite, and gold in seawater. Water in Mineral Processing, 73-85.

Drelich, J., Miller, J.D., Good, R.J., 1996. The effect of drop (bubble) size on advancing and receding contact angles for heterogeneous and rough solid surfaces as observed with sessile-drop and captive-bubble techniques. Journal of colloid and interface science 179, 37-50.

Drzymala, J., 1994. Hydrophobicityand collectorless flotation of inorganic materials. Advances in colloid and interface science 50, 143-185.

Du, H., Miller, J., 2007a. A molecular dynamics simulation study of water structure and adsorption states at talc surfaces. International Journal of Mineral Processing 84, 172-184.

Du, H., Miller, J.D., 2007b. Interfacial water structure and surface charge of selected alkali chloride salt crystals in saturated solutions: A molecular dynamics modeling study. The Journal of Physical Chemistry C 111, 10013-10022.

Du Plessis, R., 2004. The thiocarbonate flotation chemistry of auriferous pyrite.

Dussan, E., 1979. On the spreading of liquids on solid surfaces: static and dynamic contact lines. Annual Review of Fluid Mechanics 11, 371-400.

Eftekhari-Bafrooei, A., Borguet, E., 2009. Effect of surface charge on the vibrational dynamics of interfacial water. Journal of the American Chemical Society 131, 12034-12035.

Ellis, T.M.R., PHilips, I.R., Lahey, T.M., 1994. Fortran 90 programming. Addison-Wesley Wokingham, England.

Eriksson, J.C., Yoon, R., 2007. The nature of hydrophobic attraction forces. Froth Flotation: A Centenary of Innovation, Society of Mining Engineers Golden, Colorado, 133-178.

Finkelstein, N., Allison, S., Lovell, V., Stewart, B., Somasundaran, P., Grieves, R., 1975. Advances in Interfacial Phenomena of Particulate. Solution/Gas Systems, AIME, 165-175.

Fornasiero, D., Ralston, J., 2006. Effect of surface oxide/hydroxide products on the collectorless flotation of copper-activated sphalerite. International Journal of Mineral Processing 78, 231-237.

Fowler, B., 1974. Infrared studies of apatites. I. Vibrational assignments for calcium, strontium, and barium hydroxyapatites utilizing isotopic substitution. Inorganic Chemistry 13, 194-207.

Franks, G.V., Gan, Y., 2007. Charging behavior at the alumina–water interface and implications for ceramic processing. Journal of the American Ceramic Society 90, 3373-3388.

Freysz, E., Du, Q., Shen, Y., 1994. Sum frequency vibrationnal spectroscopy of water molecules at interfaces, Annales de physique, 95.

Frisch, M., Trucks, G., Schlegel, H.B., Scuseria, G., Robb, M., Cheeseman, J., Scalmani, G., Barone, V., Mennucci, B., Petersson, G., 2009. Gaussian 09, Revision A. 02, Gaussian. Inc., Wallingford, CT 200.

Fuerstenau, D., Raghavan, S., 1978. The surface and crystal chemistry of silicate minerals and their flotation behavior. Freiberger Forschungsh. A 593, 75-109.

Fuerstenau, M., Kuhn, M., Elgillani, D., 1968. The role of dixanthogen in xanthate flotation of pyrite. Trans. AIME 241, 148-156.

Fuerstenau, M., Sabacky, B., 1981. On the natural floatability of sulfides. International Journal of Mineral Processing 8, 79-84.

Fuerstenau, M.C., Miller, J.D., Kuhn, M.C., 1985. Chemistry of flotation. Society for Mining Metallurgy.

Gaudin, A., Miaw, H., Spedden, H., 1957. Native floatability and crystal structure, Proc. 2nd Int. Congr. Surf. Activity III, Electrical Phenomena and Solid/Liquid Interface. Butterworths London, 202-219.

Goumans, T., Wander, A., Brown, W.A., Catlow, C.R.A., 2007. Structure and stability of the (001) α-quartz surface. Physical Chemistry Chemical Physics 9, 2146-2152.

Grano, S., Ralston, J., Smart, R.S.C., 1990. Influence of electrochemical environment on the flotation behaviour of Mt. Isa copper and lead-zinc ore. International Journal of Mineral Processing 30, 69-97.

Guy, P., Trahar, W., 1985. The effects of oxidation and mineral interaction on sulphide flotation, Flotation of sulphide minerals. Elsevier Amsterdam, 91-110.

Hsu, P.Y., Dhinojwala, A., 2012. Contact of oil with solid surfaces in aqueous media probed using sum frequency generation spectroscopy. Langmuir 28, 2567-2573.

Irvine, W.M., Pollack, J.B., 1968. Infrared optical properties of water and ice spheres. Icarus 8, 324-360.

Jańczuk, B., Wójcik, W., Zdziennicka, A., González-Caballero, F., 1992. Determination

of the galena surface free energy components from contact angle measurements. Materials chemistry and physics 31, 235-241.

Jones, J.E., 1924. On the determination of molecular fields. I. From the variation of the viscosity of a gas with temperature, Proceedings of the Royal Society of London A: Mathematical, Physical and Engineering Sciences. The Royal Society, 441-462.

Kim, J., Kim, G., Cremer, P.S., 2001. Investigations of water structure at the solid/liquid interface in the presence of supported lipid bilayers by vibrational sum frequency spectroscopy. Langmuir 17, 7255-7260.

Koneshan, S., Rasaiah, J.C., Lynden-Bell, R., Lee, S., 1998. Solvent structure, dynamics, and ion mobility in aqueous solutions at 25 C. The Journal of Physical Chemistry B 102, 4193-4204.

Kristall, Z., Grano, S.R., Reynolds, K., Smart, R.S.C., Ralston, J., 1994. An investigation of sphalerite flotation in the Murchison Zinc concentrator, Proc. Fifth Mill Operators' Conference (Aust. Inst. Min. Metall. Publ. 1994), 171-180.

Kusalik, P.G., Svishchev, I.M., 1994. The spatial structure in liquid water. Science 265, 1219-1221.

Lambert, A.G., Davies, P.B., Neivandt, D.J., 2005. Implementing the theory of sum frequency generation vibrational spectroscopy: A tutorial review. Applied Spectroscopy Reviews 40, 103-145.

Lee, S.H., Rossky, P.J., 1994. A comparison of the structure and dynamics of liquid water at hydrophobic and hydrophilic surfaces—a molecular dynamics simulation study. The Journal of chemical physics 100, 3334-3345.

Lepetic, V., 1974. Flotation of chalcopyrite without collector after dry, autogenous grinding. CIM Bulletin 67, 71-77.

Luzar, A., Chandler, D., 1996. Effect of environment on hydrogen bond dynamics in liquid water. Physical review letters 76, 928.

Lynden-Bell, R., Rasaiah, J., 1997. From hydrophobic to hydrophilic behaviour: A simulation study of solvation entropy and free energy of simple solutes. The Journal of chemical physics 107, 1981-1991.

Mahoney, M.W., Jorgensen, W.L., 2000. A five-site model for liquid water and the reproduction of the density anomaly by rigid, nonpolarizable potential functions. The Journal of Chemical Physics 112, 8910-8922.

Marsden, J., House, I., 2006. The chemistry of gold extraction. SME.

McCarthy, M.I., Schenter, G.K., Scamehorn, C.A., Nicholas, J.B., 1996. Structure and dynamics of the water/MgO interface. The Journal of Physical Chemistry 100, 16989-

16995.

Miller, J., 2000. Hydrophobic Surface State Flotation. Encyclopedia of Separation Science, Academic Press.

Mundy, C., Mohamed, F., Schiffman, F., Tabacchi, G., Forbert, H., Kuo, W., Hutter, J., Krack, M., Iannuzzi, M., McGrath, M., 2000. CP2K software package. There is no corresponding record for this reference.

Nguyen, A., Nalaskowski, J., Miller, J., 2003. A study of bubble–particle interaction using atomic force microscopy. Minerals engineering 16, 1173-1181.

Nickolov, Z.S., Wang, X., Miller, J., 2004. Liquid/air interfacial structure of alcohol–octyl hydroxamic acid mixtures: a study by sum-frequency spectroscopy. Spectrochimica Acta Part A: Molecular and Biomolecular Spectroscopy 60, 2711-2717.

Niecikowska, A., Krasowska, M., Ralston, J., Malysa, K., 2012. Role of surface charge and hydrophobicity in the three-phase contact formation and wetting film stability under dynamic conditions. The Journal of Physical Chemistry C 116, 3071-3078.

Nieto-Draghi, C., Ávalos, J.B., Rousseau, B., 2003. Transport properties of dimethyl sulfoxide aqueous solutions. The Journal of chemical physics 119, 4782-4789.

Obraztsov, A., Obraztsova, E., Tyurnina, A., Zolotukhin, A., 2007. Chemical vapor deposition of thin graphite films of nanometer thickness. Carbon 45, 2017-2021.

Ostroverkhov, V., Waychunas, G.A., Shen, Y., 2004. Vibrational spectra of water at water/α-quartz (0001) interface. Chemical Physics Letters 386, 144-148.

Ostroverkhov, V., Waychunas, G.A., Shen, Y., 2005. New information on water interfacial structure revealed by phase-sensitive surface spectroscopy. Physical review letters 94, 046102.

Palacky, G., 1988. Resistivity characteristics of geologic targets. Electromagnetic methods in applied geophysics 1, 53-129.

Palmer, D., 2009. CrystalMaker Software. CrystalMaker Software Ltd, Oxford, England.

Pearlman, D.A., Case, D.A., Caldwell, J.W., Ross, W.S., Cheatham, T.E., DeBolt, S., Ferguson, D., Seibel, G., Kollman, P., 1995. AMBER, a package of computer programs for applying molecular mechanics, normal mode analysis, molecular dynamics and free energy calculations to simulate the structural and energetic properties of molecules. Computer Physics Communications 91, 1-41.

Peng, Z., Merz Jr, K.M., 1992. The gas-phase and solution-phase free energy surfaces for carbon dioxide reaction with hydroxide ($CO_2 + OH^-$. fwdarw. HCO_3^-). Journal of the American Chemical Society 114, 2733-2734.

Perdew, J.P., Burke, K., Ernzerhof, M., 1996. Generalized gradient approximation made simple. Physical review letters 77, 3865.

Perdew, J.P., Ziesche, P., Eschrig, H., 1991. Electronic structure of solids' 91. Akademie Verlag, Berlin.

Politano, A., Chiarello, G., 2013. The nature of free OH stretching in water adsorbed on carbon nanosystems. The Journal of chemical physics 139, 064704.

Pugh, R., Rutland, M., Manev, E., Claesson, P., 1996. Dodecylamine collector—pH effect on mica flotation and correlation with thin aqueous foam film and surface force measurements. International journal of mineral processing 46, 245-262.

Raichur, A., Wang, X., Parekh, B., 2000. Quantifying pyrite surface oxidation kinetics by contact angle measurements. Colloids and Surfaces A: Physicochemical and Engineering Aspects 167, 245-251.

Rappé, A.K., Casewit, C.J., Colwell, K., Goddard Iii, W., Skiff, W., 1992. UFF, a full periodic table force field for molecular mechanics and molecular dynamics simulations. Journal of the American Chemical Society 114, 10024-10035.

Rasaiah, J.C., Zhu, J., 1990. Cavity functions and association in models for weak electrolytes and sticky hard spheres. The Journal of Chemical Physics 92, 7554-7564.

Ravitz, S., 1940. AIME Tech. Pub. 1147

Richmond, G., 2002. Molecular bonding and interactions at aqueous surfaces as probed by vibrational sum frequency spectroscopy. Chemical Reviews 102, 2693-2724.

Rowlinson, J.S., Swinton, F., 2013. Liquids and Liquid Mixtures: Butterworths Monographs in Chemistry. Butterworth-Heinemann.

Rustad, J.R., Felmy, A.R., Bylaska, E.J., 2003. Molecular simulation of the magnetite-water interface. Geochimica et cosmochimica acta 67, 1001-1016.

Schrödle, S., Richmond, G.L., 2008. In situ non-linear spectroscopic approaches to understanding adsorption at mineral–water interfaces. Journal of Physics D: Applied Physics 41, 033001.

Shen, Y., 1994. Surfaces probed by nonlinear optics. Surface Science 299, 551-562.

Shen, Y., Nihonyanagi, S., Uosaki, K., 2001. Sum frequency generation (SFG) study of the pH-dependent water structure on a fused quartz surface modified by an octadecyltrichlorosilane (OTS) monolayer. Physical Chemistry Chemical Physics 3, 3463-3469.

Shen, Y.R., Ostroverkhov, V., 2006. Sum-frequency vibrational spectroscopy on water interfaces: Polar orientation of water molecules at interfaces. Chemical Reviews 106,

1140-1154.

Shi, B., Dhir, V.K., 2009. Molecular dynamics simulation of the contact angle of liquids on solid surfaces. The Journal of chemical physics 130, 034705.

Sithole, H., Ngoepe, P., Wright, K., 2003. Atomistic simulation of the structure and elastic properties of pyrite (FeS_2) as a function of pressure. Physics and chemistry of minerals 30, 615-619.

Smart, R.S., Amarantidis, J., Skinner, W.M., Prestidge, C.A., La Vanier, L., Grano, S.R., 2003. Surface analytical studies of oxidation and collector adsorption in sulfide mineral flotation. Springer.

Smith, D.E., Dang, L.X., 1994. Computer simulations of NaCl association in polarizable water. The Journal of Chemical Physics 100, 3757-3766.

Somasundaram, T., Lynden-Bell, R., Patterson, C., 1999. A simulation study of the kinetics of passage of CO2 and N2 through the liquid/vapor interface of water. The Journal of chemical physics 111, 2190-2199.

Somasundaran, P., 2006. Encyclopedia of surface and colloid science. CRC press.

Sovago, M., Campen, R.K., Wurpel, G.W., Müller, M., Bakker, H.J., Bonn, M., 2008. Vibrational response of hydrogen-bonded interfacial water is dominated by intramolecular coupling. Physical review letters 100, 173901.

Stapelbroek, B., Jansen, H., Kooij, E., Snoeijer, J., Eddi, A., 2014. Universal spreading of water drops on complex surfaces. Soft matter 10, 2641-2648.

Steudel, R., Eckert, B., 2003. Solid sulfur allotropes sulfur allotropes, Elemental sulfur and sulfur-rich compounds I. Springer, 1-80.

Strunz, H., Nickel, E.H., 2001. Strunz mineralogical tables: chemical-structural mineral classification system. Schweizerbart.

Subrahmanyam, T., Monte, M., Middea, A., Valdiviezo, E., Lins, F., 1999. Contact angles of quartz by capillary penetration of liquids and captive bubble techniques. Minerals engineering 12, 1347-1357.

Takahashi, T., Miyahara, T., Mochizuki, H., 1979. Fundamental study of bubble formation in dissolved air pressure flotation. Journal of Chemical Engineering of Japan 12, 275-280.

Todorova, T., Alexiev, V., Prins, R., Weber, T., 2004. Ab initio study of 2H-MoS_2 using Hay and Wadt effective core pseudo-potentials for modelling the (1010) surface structure. Physical Chemistry Chemical Physics 6, 3023-3030.

Van Loon, L.L., Allen, H.C., 2004. Methanol reaction with sulfuric acid: a vibrational

spectroscopic study. The Journal of Physical Chemistry B 108, 17666-17674.

VandeVondele, J., Hutter, J., 2007. Gaussian basis sets for accurate calculations on molecular systems in gas and condensed phases. The Journal of chemical physics 127, 114105.

VandeVondele, J., Krack, M., Mohamed, F., Parrinello, M., Chassaing, T., Hutter, J., 2005. Quickstep: Fast and accurate density functional calculations using a mixed Gaussian and plane waves approach. Computer Physics Communications 167, 103-128.

Wang, J., Kalinichev, A.G., Kirkpatrick, R.J., 2004a. Molecular modeling of water structure in nano-pores between brucite (001) surfaces. Geochimica et Cosmochimica Acta 68, 3351-3365.

Wang, J., Kalinichev, A.G., Kirkpatrick, R.J., 2006. Effects of substrate structure and composition on the structure, dynamics, and energetics of water at mineral surfaces: A molecular dynamics modeling study. Geochimica et cosmochimica acta 70, 562-582.

Wang, J., Wolf, R.M., Caldwell, J.W., Kollman, P.A., Case, D.A., 2004b. Development and testing of a general amber force field. Journal of computational chemistry 25, 1157-1174.

Wang, X., Liu, J., Du, H., Miller, J., 2009. States of adsorbed dodecyl amine and water at a silica surface as revealed by vibrational spectroscopy. Langmuir 26, 3407-3414.

Wang, X., Pan, B., Cheng, H., Miller, J., 2013. Separation of carnallite from halite by reverse flotation with dodecyl morpholine for the production of potash. Presentation, 2013 SME Annual Meeting, Denver, Colorado, 24-27.

Wang, X., Yin, X., Nalaskowski, J., Du, H., Miller, J., 2012. Molecular features of water films created with bubbles at hydrophilic and hydrophobic surfaces, Proceedings XXVI IMPC 2012, New Delhi, India, 5819-5828.

Wang, X., Yin, X., Nalaskowski, J., Du, H., Miller, J.D., 2014. Molecular features of water films created with bubbles at silica surfaces.

Wang, H.-F., Gan, W., Lu, R., Rao, Y., Wu, B.-H., 2005. Quantitative spectral and orientational analysis in surface sum frequency generation vibrational spectroscopy (SFG-VS). International Reviews in Physical Chemistry 24, 191-256.

Werder, T., Walther, J.H., Jaffe, R., Halicioglu, T., Koumoutsakos, P., 2003. On the water-carbon interaction for use in molecular dynamics simulations of graphite and carbon nanotubes. The Journal of Physical Chemistry B 107, 1345-1352.

Weston, D., 1978. Concentration of hydrated aluminum oxide minerals by flotation. Google Patents.

Wiberg, N., 2001. Holleman-Wiberg's inorganic chemistry. Academic Press, New York.

Wilson, I.D., Adlard, E.R., Cooke, M., Poole, C.F., 2000. Encyclopedia of separation science. Acad. Press.

Wright, K., Gale, J.D., 2004. Interatomic potentials for the simulation of the zinc-blende and wurtzite forms of ZnS and CdS: Bulk structure, properties, and phase stability. Physical Review B 70, 035211.

Yalamanchili, M., Kellar, J., Miller, J., 1991. In-situ FT-IR internal reflection spectroscopy of collector adsorption phenomena in soluble-salt flotation systems, Proceedings of the XVII International Mineral Processing Congress, 131-142.

Yeganeh, M., Dougal, S., Pink, H., 1999. Vibrational spectroscopy of water at liquid/solid interfaces: Crossing the isoelectric point of a solid surface. Physical Review Letters 83, 1179.

Yin, X., 2012. Anisotropic Surface Features of Selected Phyllosilicates. The University of Utah.

Yu, C.J., Richter, A., Datta, A., Durbin, M., Dutta, P., 1999. Observation of molecular layering in thin liquid films using X-ray reflectivity. Physical Review Letters 82, 2326.

Zachwieja, J.B., McCarron, J.J., Walker, G.W., Buckley, A.N., 1989. Correlation between the surface composition and collectorless flotation of chalcopyrite. Journal of colloid and interface science 132, 462-468.

Zhang, L., Tian, C., Waychunas, G.A., Shen, Y.R., 2008. Structures and charging of α-alumina (0001)/water interfaces studied by sum-frequency vibrational spectroscopy. Journal of the American Chemical Society 130, 7686-7694.

Zhang, X., Du, H., Wang, X., Miller, J., 2013. Surface chemistry considerations in the flotation of rare-earth and other semisoluble salt minerals.

Zhang, X., Wang, X., Miller, J.D., 2014. Wetting of selected fluorite surfaces by water. Surface Innovations 3, 39-48.

Zhuang, X., Miranda, P., Kim, D., Shen, Y., 1999. Mapping molecular orientation and conformation at interfaces by surface nonlinear optics. Physical Review B 59, 12632.